

**The Dissertation Committee for Stavros Gaitanaros Certifies that this is the
approved version of the following dissertation:**

On the Quasi-static and Dynamic Crushing of Random Foams

Committee:

Stelios Kyriakides, Supervisor

Andrew M. Kraynik

Krishnaswamy Ravi-Chandar

Kenneth M. Liechti

Chad M. Landis

On the Quasi-static and Dynamic Crushing of Random Foams

by

Stavros Gaitanaros, B.E.; M.E.

Dissertation

Presented to the Faculty of the Graduate School of

The University of Texas at Austin

in Partial Fulfillment

of the Requirements

for the Degree of

Doctor of Philosophy

The University of Texas at Austin

May, 2014

Acknowledgements

I would like to express my sincere gratitude to my advisor, Professor Stelios Kyriakides, whose mentoring was paramount not only for the completion of this dissertation but more importantly in my growth as a scientist and an engineer. He was always there to offer advice, a second chance when I needed it and his discreet help in many ways during these past years. I hope that his style of work and his ethics will follow and guide me throughout my professional career.

I would like to thank Dr. Andrew Kraynik for a fruitful collaboration and for sharing his deep insight on foams. I learned a lot in the beginning of my graduate studies from numerous interactions with Prof. Wen-Yea Jang. I would also like to express my gratitude to all members of my PhD committee and especially Prof. Ravi-Chandar for our discussions on the dynamic crushing of foams. I owe a lot to Prof. Mark Mear who is an exceptional teacher and serving as his TA was a pleasure. Scott Messec was always available to provide technical support and his help has been invaluable.

Many thanks go to all the guys in the group for all the much needed breaks from routine; special thanks go to (in order of appearance) Prof. Yannis Korkolis, Dr. Liang-Hai Lee, Dr. Julian Hallai, Nate Bechle and Lin Yuan. I owe deep gratitude to all of my friends in Austin and particularly Nikolas Bouklas and his wife Christina that helped me maintain a (form of) life outside of WRW.

I would not be able to do this without the continuous love and support from my family; my sisters Elena and Marina who still treat me as the youngest one and whom I miss a lot, and of course my mother for always being there no matter what.

Finally I dedicate this to Maria. Pursuing a PhD was just one of the many adventures that we have embarked upon together.

On the Quasi-static and Dynamic Crushing of Random Foams

Stavros Gaitanaros, Ph.D.

The University of Texas at Austin, 2014

Supervisor: Stelios Kyriakides

Lightweight cellular materials such as foams exhibit excellent energy absorption characteristics and are widely used for impact mitigation in a variety of applications. In this study a modeling framework is developed in order to investigate the crushing behavior of Al-alloy open-cell foams under quasi-static and dynamic loadings. Quasi-static crushing produces a response that exhibits a relatively stiff linearly elastic regime that terminates into a load maximum; it is followed by an extended load plateau during which localized cell crushing initiates and gradually spreads throughout the specimen. When most of the cells are crushed the densified material stiffens again. Quasi-static compression is simulated using micromechanically accurate foam models. Skeletal random models are generated from soap froth using the Surface Evolver software. The linear edges of the skeletal microstructure are then dressed with appropriate distributions of solid to match those of ligaments in the actual foams and their relative density. The ligaments are modeled as shear-deformable beams with variable cross sections discretized with beam elements in LS-DYNA, while the Al-alloy is modeled as a finitely deforming elastic-plastic material. Utilization of the beam-to-beam contact algorithm of the code is an essential component of the simulation of crushing. Such models are shown to reproduce all aspects of quasi-static crushing faithfully.

Dynamic crushing experiments on the same foam have shown that specimens impacted at velocities of 60 m/s and above develop nearly planar shocks that propagate at well-defined velocities crushing the specimen. The same modeling framework is used to simulate these impact experiments. It is demonstrated that random foam models reproduce essentially all aspects of the dynamic crushing behavior observed experimentally. This includes the formation and propagation of shocks, the stresses at both ends, the Hugoniot strain, and the linear relationship of shock front vs. impact velocities. The same models are also used to examine the transition from quasi-static to shock front type crushing. In addition, a detailed parametric analysis is performed to examine the effect of relative density on the crushing response, from the quasi-static initiation and plateau stresses to the formation of shocks and the associated Hugoniot.

Table of Contents

Chapter 1: Introduction	1
1.1 Foam Manufacturing and Microstructure	2
1.2 Quasi-Static Compressive Response and Crushing of Foams	3
1.3 Dynamic Crushing of Foams	4
Chapter 2: Random Foam Modeling.....	12
2.1 Microstructure of aluminum foams	13
2.1.1 X-Ray Micro-Computed Tomography	13
2.1.2 Aluminum Foam Morphology	14
2.2 Geometry of random foam models	15
2.2.1 Random Foam by Surface Evolver	15
2.2.2 Anisotropy and Cropping.....	16
2.3 Finite Element Modeling	17
2.3.1 Discretization and Material Distribution	17
2.3.2 Contact Implementation.....	20
2.3.3 Density Correction	21
2.3.4 Material Behavior	21
Chapter 3: Quasi-static Crushing.....	32
3.1 Experimental Crushing Responses	33
3.1.1 Rise Direction Experiments	33
3.1.2 Transverse Direction Experiments	35
3.2 Numerical Results with Random Foam Models	35
3.2.1 Model Parameters and Boundary Conditions	35
3.2.2 Crushing in the Rise Direction	36
3.2.3 Effect of Domain Size and Structure Variations	40
3.2.4 Crushing in the Transverse Direction.....	41
3.3 Random Foam Modeling vs. Kelvin Cell Models	43
3.3.1 Kelvin Cell and Random Foam Modeling Similarities and Differences	43

3.3.2 Kelvin Cell and Random Foam Modeling Performance.....	44
Chapter 4: Review of Dynamic Crushing Experiments and Hugoniot.....	64
4.1 Direct Impact and Shock Formation.....	64
4.1.1 Experimental Set-Up for Direct and Stationary Impact Experiments.....	64
4.1.2 Results from a Direct Impact Experiment that Develops Shocks	65
4.2 Construction of the Hugoniot.....	68
4.2.1 Shock Equations.....	68
4.2.2 Hugoniot.....	70
4.2.3 Effect of specimen density and anisotropy.....	74
4.3 Impact at Subcritical Velocities.....	75
Chapter 5: Dynamic Crushing Simulations.....	94
5.1 Dynamic Model.....	95
5.1.1 Domain Size, Density and Anisotropy.....	95
5.1.2 Quasi-Static Response.....	95
5.2 Dynamic Crushing and Shocks.....	97
5.2.1 Initial and Boundary Conditions.....	97
5.2.2 Simulation of Direct Impact that Develops Shocks.....	97
5.2.3 Effect of the Anvil-Bar Interface.....	101
5.2.4 Constant Velocity Impact.....	102
5.2.5 Effect of Cell Size.....	103
5.2.6 Direct Impact at Different Velocities.....	104
5.3 Hugoniot: Comparisons of Experiments and Analysis.....	105
5.4 Impact at Subcritical Velocities.....	107
Chapter 6: Foam Density and Energy Absorption.....	137
6.1 Quasi-static Crushing For Varying Density.....	138
6.2 Direct Impact Simulation for Different Densities.....	140
6.3 Effect of Relative Density on the Hugoniot.....	142
6.4 Effect of Density on the Transition to Shock Formation.....	143

Chapter 7: Summary and Conclusions.....	156
7.1 Quasi-static Crushing.....	156
7.2 Dynamic Crushing	158
7.3 Effect of Relative Density on Crushing and Energy Absorption.....	160
7.4 Future Work	161
Appendix A.....	163
References.....	165
Vita	171

Chapter 1: Introduction

Materials with cellular microstructure are one of Nature's methods of producing lightweight but strong structures while simultaneously conserving material. Examples include most woods (Fig. 1.1a¹), trabecular bone (Fig. 1.1b²), fruits and vegetables (Fig. 1.1c³), cork, stalks and roots of plants (Fig. 1.1d⁴), coral and shells, etc., all of which combine high stiffness with relatively low density. Man-made cellular materials can be made from most metals, polymers, ceramics and come as space filling foams (Fig. 1.1e⁵) or two-dimensional honeycombs (Fig. 1.1f⁵). Both natural and synthetic cellular solids possess unique mechanical, thermal, acoustical, and other properties that make them attractive in a broad range of applications (e.g., see Gibson and Ashby, 1997; Gibson *et al.*, 2010). These include uses in acoustic and thermal insulation (Fig. 1.2a⁶), as coatings for orthopedic implants and tissue engineering scaffolds, as core in sandwich panels (Fig. 1.2b⁷), and in a plethora of impact mitigation applications (Figs. 1.2c and 1.2d⁸) ranging from packaging to automotive and aerospace blast protection. This thesis focuses on the mechanical properties of a class of open-cell foams with special emphasis on the crushing response and energy absorption under quasi-static and dynamic loadings.

¹ reproduced from <http://civcal.media.hku.hk/materials/wood/structure>

² reproduced from <https://www.llnl.gov/str/Sep06/Kinney.html>

³ reproduced from <http://rsif.royalsocietypublishing.org/content/early/2012/08/07/rsif.2012.0341.full>

⁴ reproduced from <http://iopscience.iop.org/0295-5075/91/1/18001/fulltext/>

⁵ reproduced from Jang (2008)

⁶ reproduced from http://www.basf.de/basfcorp/copsfiles/pressefotodb/9342_12_190_large.jpg

⁷ reproduced from <http://www.tms.org/pubs/journals/JOM/0012/Banhart-0012.html>

⁸ reproduced from <http://www.newsday.com/sports/baseball/mets/baseball-taking-concussions-seriously-1.2809412>

1.1 Foam Manufacturing and Microstructure

Synthetic foams have a polyhedral cellular microstructure generated either through a foaming process, powder compaction, by vapor deposition on a polymeric template, by casting, and more recently by 3D printing (e.g., Ashby et al., 2000). Their cells can be *open* (Figs. 1.3a and 1.4a) or *closed* (Fig. 1.1e): in the first case the material is concentrated in the nearly straight edges of the polyhedra, and in the nodes at which they intersect; in the latter case the cell faces are covered with thin membranes or plates. A key variable of all cellular materials is their relative density ($\rho^*/\rho \equiv$ density of foam/density of base material), which ranges from 1% at the lower end and 15% at the other extreme (e.g., Hilyard and Cunningham, 1994; Ashby *et al.*, 2000).

A large class of foams is produced by a foaming process involving a polymeric resin, diisocyanate, water and other ingredients (see Artavia and Macosko, 1994; Priester and Turner, 1994; Foamex, 2003). They are introduced in a controlled manner in a mixer resulting in an exothermic reaction that generates CO₂ bubbles. The bubbles expand causing a significant increase in the volume that leads to generating a soap-froth like microstructure through the intersection of bubbles. During the rise of the foam the compound starts to solidify and, for open-cell microstructures, the gas bubbles burst leaving behind polyhedra such as those shown in Fig. 1.3a. For such foams the randomly packed polyhedral cells have 11 to 17 faces (Matzke, 1946). The nearly straight edges, or *ligaments*, have characteristic three-cusp hypocycloid cross sections known as *Plateau borders* (see Fig. 1.3b). The foaming process usually results in some elongation of the cells in the rise direction. This elongation is an anisotropy that affects the mechanical and other properties of the polymerized and solidified foam.

The ERG Duocel® foam used in this study is manufactured by using polymeric foam templates to generate a mold in which an Al alloy is cast (Ashby et al., 2000; Jang

et al., 2008). The main characteristics of the cellular microstructure (see Fig. 1.4a) are similar to those of the polymeric foams. However the cross sections of the ligaments have lost their concave hypocycloid shapes and are now convex as shown in Fig. 1.4b. As a consequence, the relative density of the aluminum foam is significantly higher than that of the polymeric template. In both the original polymeric and aluminum foams the cross sectional area of the ligaments is smallest at mid-span and increases as the nodes are approached (see Figs. 1.3b and 1.4b).

1.2 Quasi-Static Compressive Response and Crushing of Foams

The interconnected network microstructure coupled with the mechanical properties of the base material is essential ingredients to any effort to model the mechanical properties of foams. These include all aspects of their compressive response (see Figs. 1.5a and 1.5b), i.e. the linear elastic regime, the stress plateau and its extent through the second stiffening branch. The approach taken in past studies (Gong and Kyriakides, 2005; Jang and Kyriakides, 2009b) has been to build up micromechanical models that capture the key geometric features mentioned above, i.e., the appropriate anisotropy and material distribution, endow them with suitable constitutive models for the base material, and use them to reproduce all aspects of quasi-static mechanical responses. Motivated by the nearly monodisperse nature of the microstructure of the polymeric and metallic foams analyzed in Gong *et al.* (2005), Jang *et al.* (2008), and Jang and Kyriakides (2009a), the cellular microstructure was modeled using the 14-sided, periodic Kelvin cell. It was shown that such models capture with accuracy the initial anisotropic elastic moduli (Gong *et al.*, 2005; Jang *et al.*, 2008), the “yield stress” that also represents the onset of instability (Laroussi *et al.* 2002; Gong and Kyriakides, 2005; Gong *et al.*, 2005; Jang *et al.*, 2010), the localization of deformation and its spreading

tracing a nearly flat stress plateau, and the eventual densification (Gong and Kyriakides, 2005; Jang and Kyriakides, 2009b). The only weakness of complete crushing responses produced by Kelvin cell models is that the crushing patterns differ from those of actual random foams caused by the regularity of their microstructure. Furthermore, Kelvin cell models are only applicable to monodisperse foams (for crushing of foams with other regular microstructures see Luxner *et al.*, 2007).

The present study extends these previous works by introducing numerical models with more representative random microstructures. The models are capable of simulating the complete crushing behavior of open-cell foams that also produce the correct crushing patterns. This modeling framework is described in Chapter 2. The random foam models start as soap froth microstructures generated using the *Surface Evolver* software (Brakke, 1992; Kraynik, 2003; Kraynik, 2006). Simulation of a complete crushing process from localization to densification requires large size models, which in turn dictates that ligaments are modeled as shear deformable beams with variable cross sections. Beam-to-beam contact on the outer surface of ligaments is an essential component of the models. In Chapter 3 the effectiveness of random foam models in capturing all aspects of the quasi-static crushing response of open-cell foams is tested. This includes the response in the rise and transverse direction and the associated crushing patterns that are directly compared to the ones observed experimentally.

1.3 Dynamic Crushing of Foams

The low initial stress peaks and extended load plateaus of foams constitute excellent energy absorption characteristics and make them attractive in a variety of impact mitigation and blast protection applications. For this reason, their behavior under dynamic loading has been of practical interest and several studies have been performed

on the dynamic crushing of polymeric (Morris, 1991; Skews *et al.*, 1991; Zaretsky and Ben-Dor, 1995; Zaretsky *et al.*, 2012) and metal foams (Tan *et al.*, 2005a; Radford *et al.*, 2005; Lee *et al.*, 2006; Nemat-Nasser *et al.*, 2007; Elnasri *et al.*, 2007; Maines *et al.*, 2010; Tan *et al.*, 2012). All of these works report the formation of shocks when the foam is impacted above a critical velocity. This is attributed to what has been established before in the shock physics community; material systems with adiabatic compression modulus that increases with further compression can be expected to develop stable shocks (e.g., see Bethe, 1942). Herrmann (1969) illustrated this for a class of porous metals, an application that is related to modern foams but with a much larger relative density. Reid and Peng (1997) reported shock-like behavior in another class of cellular materials, wood, which results in significant enhancement in the stress behind the shocks. In an attempt to analyze this behavior, they assumed a constitutive model based on a *rigid-perfectly-plastic-locking* (or rigid)—*r-p-p-l*—approximation of the quasi-static compressive response of the material. This type of constitutive model has been used in several other efforts involving shock forming cellular materials. Pattofatto *et al.* (2007) replaced the r-p-p-l with a more representative power-law fit of the convex rising branch of the quasi-static response.

With this as background, Barnes (2012) and Barnes *et al.* (2014) conducted a series of experiments designed to provide a more complete characterization of dynamic crushing and shock formation. Their results, reported in Chapter 4, come from a series of impact tests on Al-6101-T6 open-cell foam in which high-speed photography was used to establish the shock velocity and the strain behind the shock directly from experiments. Such measurements at different impact speeds enabled the establishment of the Hugoniot, which in turn allows calculation of all problem variables without resorting to a constitutive model.

In chapter 5, suitably sized and calibrated random foam models, generated in a similar fashion to the ones used in quasi-static crushing (Chapter 2 and Gaitanaros *et al.*, 2012), are utilized to simulate several of the dynamic crushing and shock propagation experiments reported in Chapter 4. The numerical results are directly compared in all aspects with the dynamic crushing behavior observed in the experiments. This includes the formation and propagation of shocks, the stresses across the shock, the Hugoniot strain, and the linear relationship of shock front vs. impact velocities. The same modeling framework is subsequently used to examine the transition from quasi-static to shock type crushing.

In Chapter 6, a detailed parametric analysis is performed that examines the effect of relative density on the crushing response. Using the same microstructure to construct foam models with different densities we are able to derive how relative density affects the quasi-static initiation and plateau stresses, the densification strain, the formation of shocks, all representations of the Hugoniot and the total energy absorbed. Finally, conclusions and future work are presented in Chapter 7.

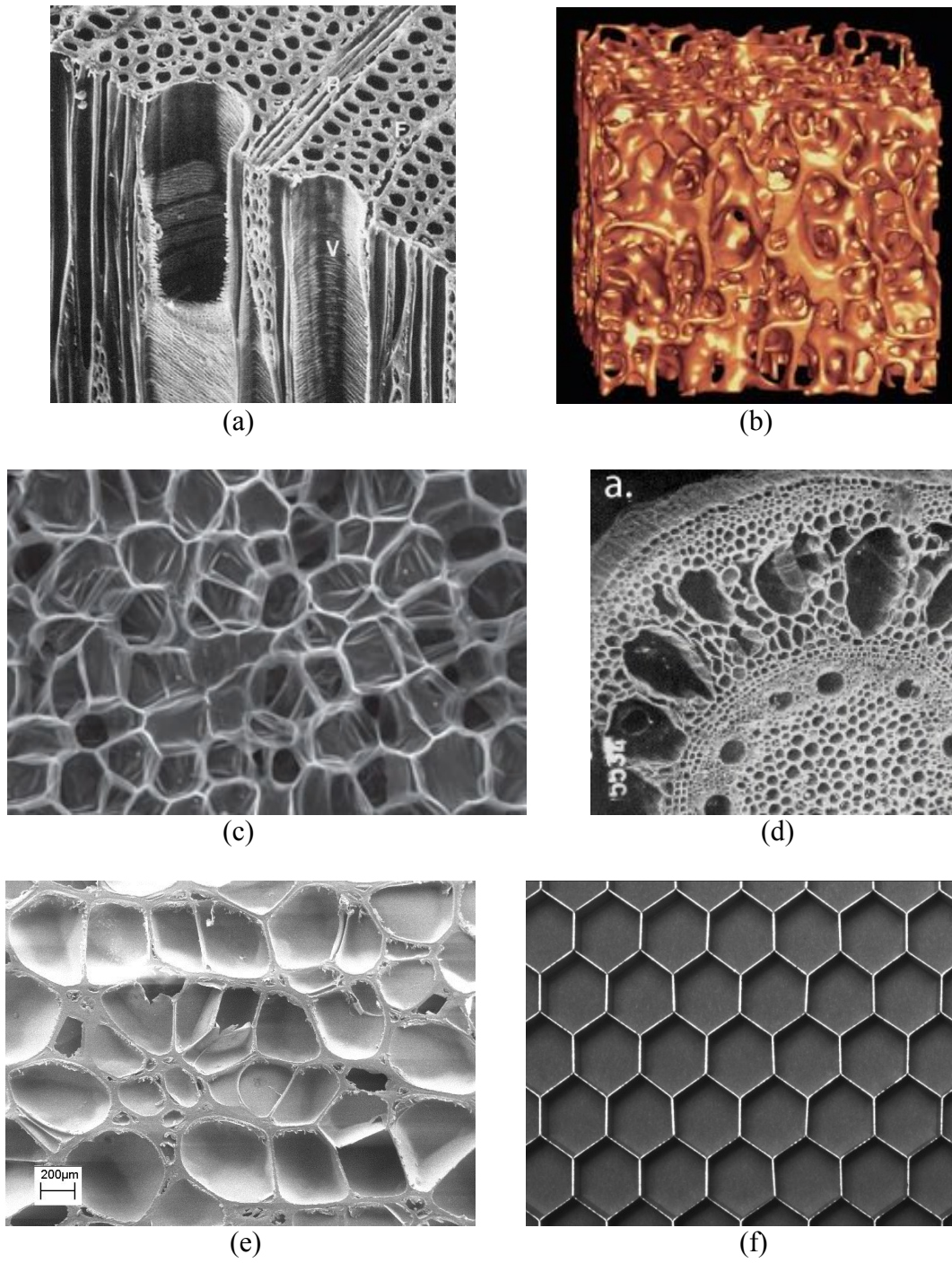
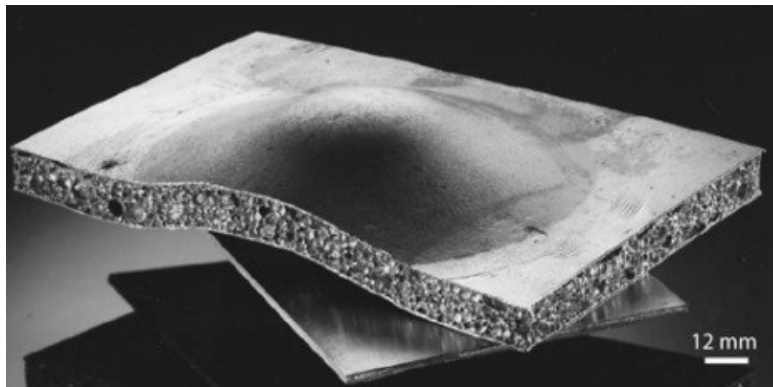


Fig. 1.1 Cellular materials: (a) Hardwood; (b) trabecular bone; (c) carrot; (d) root of *Zea mays*; (e) closed cell foam; (f) hexagonal honeycomb.



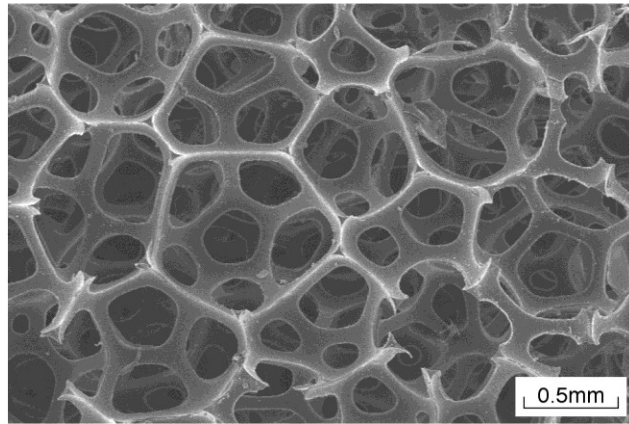
(a)



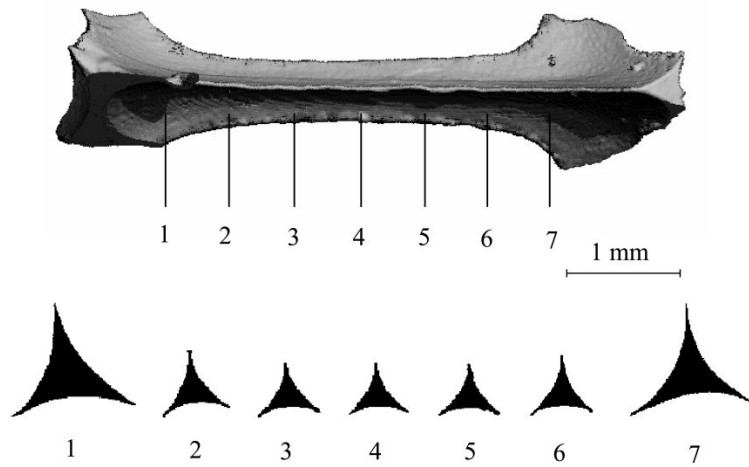
(b)



Fig. 1.2 Foam applications: (a) Thermal insulation in trains; (b) sandwich panel; (c) car bumper; (d) helmet cushioning.

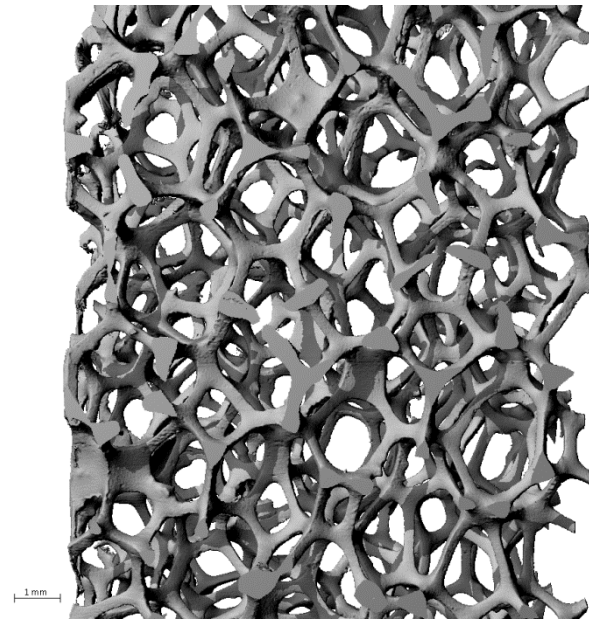


(a)

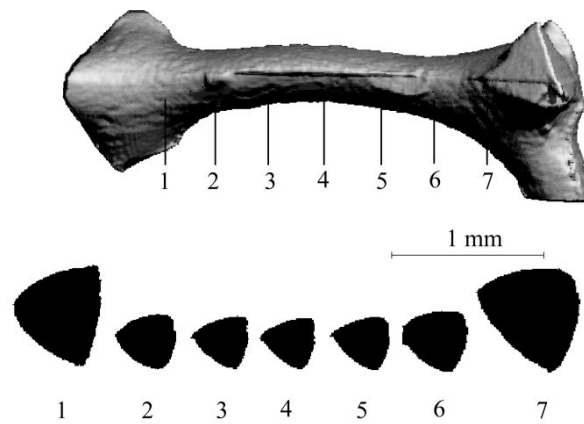


(b)

Fig. 1.3 Open-cell polymeric foam: (a) Microstructure and (b) ligament and cross sections (Jang *et al.*, 2008).

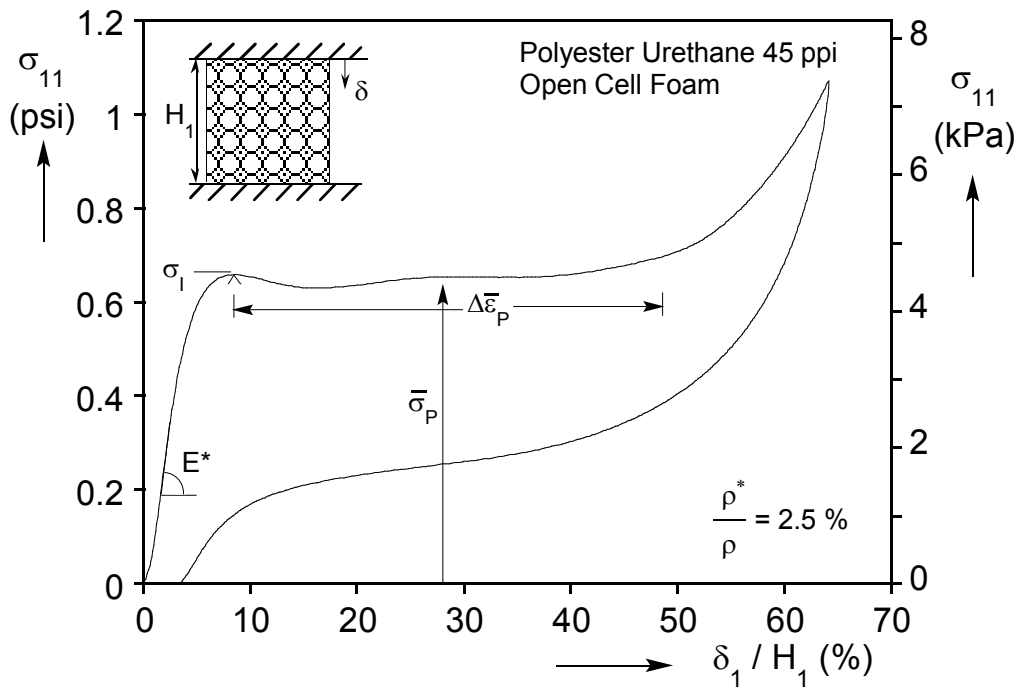


(a)

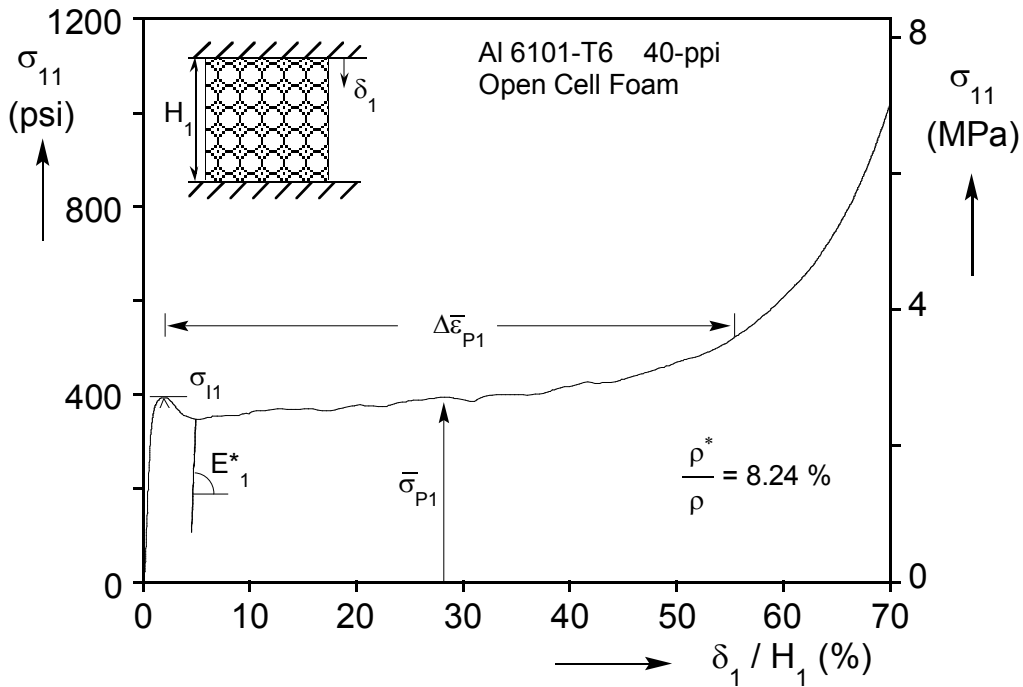


(b)

Fig. 1.4 Open-cell Aluminum foam: (a) Microstructure and (b) ligament and cross sections (Jang *et al.*, 2008).



(a)



(b)

Fig. 1.5 Typical compressive response of (a) a polymeric (Gong *et al.*, 2005) and (b) an aluminum alloy foam (Jang and Kyriakides, 2009a).

Chapter 2: Random Foam Modeling

Open-cell solid foams consist of randomly packed polyhedral cells that result from the foaming process. In the case of nearly monodisperse foams, the polyhedra have anywhere from 11 to 17 faces (Matzke, 1946) and the material is concentrated in nearly straight edges and in the nodes where four ligaments meet. This microstructure is responsible for the unique mechanical, thermal, acoustical and other properties of such foams (e.g., see Hilyard and Cunningham, 1994; Gibson and Ashby, 1997; Weaire and Hutzler, 1999; Ashby *et al.*, 2000). A main objective of the research community has been to connect the foam microstructure to these properties.

A significant degree of success in reproducing all mechanical properties of a class of monodisperse polymeric and metal foams was achieved by using models that idealized the microstructure as consisting of 14-sided regular cells of Kelvin (Thompson, 1887; see also Warren and Kraynik, 1997; Zhu *et al.*, 1997; Laroussi *et al.*, 2002; Gong *et al.*, 2005a; Gong and Kyriakides, 2005; Gong *et al.*, 2005b; Jang *et al.*, 2008; Jang and Kyriakides, 2009b). Essential components of these models were the introduction of the correct anisotropy, ligament geometry and actual mechanical properties of the base material into the periodic microstructures. Despite this success, Kelvin cell models have some limitations and disadvantages. First, they are limited to monodisperse foams and second the resultant localization and crushing modes of deformation, governed by the regularity of the microstructure, differ from those observed in actual foams (see Chapter 3).

In this work, the randomness of the cellular microstructure is modeled with reasonable accuracy using realistic random soap froth generated using the Surface Evolver software (Brakke, 1992). The generated models are subsequently used to study the quasi-static and dynamic crushing responses of a class of open-cell aluminum alloy

foams. Soap froth random models with N^3 cells are generated using the Surface Evolver. The ligaments are made straight but with non-uniform cross sectional area distributions that mimic those of the physical foams. The models are assigned, as was done in previous studies, the density and anisotropy measured. The ligaments are modeled as shear deformable beams with the elasto-plastic material behavior of the Al-alloy. The microstructure is discretized with finite elements using LS-DYNA, which allows for beam-to-beam contact on the outer surface of the ligaments essential for random and polydisperse microstructures. We start by a short review of the aspects of the microstructure of aluminum foams that are going to be incorporated in our modeling framework, which is described in detail next.

2.1 Microstructure of aluminum foams

2.1.1 X-Ray Micro-Computed Tomography

The foam examined in this work is the Aluminum 6101-T6 ERG Duocel ® open-cell foam. A detailed study on the microstructure of this particular foam was performed in Jang *et al.* (2008) using computed tomography (see also Jang and Kyriakides, 2009a). Computed X-ray tomography is a non-destructive visualization technique that provides a fully 3D rendering with all internal details of a body (ASTM E1441-00, 1992; Ketcham and Carlson, 2001). The technique works by mapping the spatial distribution of the linear attenuation coefficients of the body, which is a function of the density and atomic number of the material being scanned and the X-ray energy. A slice image is taken by first sending a thin fan of X-rays from a point source located on one side of the specimen. As the X-rays pass through the body, they are attenuated differently by regions of different density and the net attenuation along each ray path is recorded by a detector. A new signal is subsequently sent from a slightly different angle. This procedure is repeated N times (N depends on desired resolution) until the specimen turns a complete revolution.

Software based on a backward projection algorithm is then used to process the N angular images and to reconstruct the 3-D attenuation map of the slice. The process is repeated for a new neighboring slice until the whole body is scanned. The slices are then assembled to form a 3-D image of the whole body. A typical image of the microstructure of such an Al foam used in this study generated using X-ray tomography is shown in Fig. 2.1.

2.1.2 Aluminum Foam Morphology

The random microstructure shown in Fig. 2.1 consists of polyhedral cells of nearly uniform size (i.e., the foam is essentially monodisperse) with a varying number of faces. This particular type of metal foam is manufactured by using polymeric foams as templates to generate molds in which Al alloy is cast. Consequently, they have the same distribution of random polyhedra and polygonal sides as polymeric and more generally liquid foams. For the same reason, the cells are somewhat elongated in the direction in which the originally liquid foam rose as carbon dioxide gas bubbles developed (approximately the vertical direction of the image in Fig. 2.1—designated as rise direction). For this particular foam the elongated dimension is on average about 1.18 times the cell dimensions in the transverse plane and this ratio is defined as the anisotropy (λ). The polyhedral geometry and anisotropy are illustrated in an individual cell extracted from the scanned image in Fig. 2.2a. Thus, for example, this cell has 13 faces that include 3 quadrilaterals, 6 pentagons, 4 hexagons and a total of 33 ligaments.

A closer look at a ligament (see Fig. 2.2b) shows that it is nearly linear with convex cross sections that are somewhere between triangular and circular shapes. The cross sectional area varies along the length. This area distribution plays an important role in the modeling and was studied in detail in Jang *et al.* (2008). Figure 2.3 shows a plot of

the normalized area ($A(\xi)/A_o$) vs. normalized length ($\xi = x/\ell$) that was generated from many measurements on ligaments from foams of three different cell sizes. In addition to the area variation along the length, the mid-cross sectional area, A_o , varies with the ligament length. Figure 2.4 from the same reference shows clearly that longer ligaments are thinner while shorter ones are thicker. The distribution of lengths for the ligaments is given in the form of a frequency bar graph in Fig. 2.5. The distribution is similar to the one for a polymeric foam (see Fig. 5 in Jang *et al.*, 2008) with a stronger concentration around the mean value.

These measurements will form the basis of the numerically generated model foams that follows. Ligaments will be divided into two groups according to their length and the corresponding cross sectional areas will vary along the length. Realistic material distribution and the effect of anisotropy are essential components for the accurate reproduction of all mechanical properties of foams.

2.2 Geometry of random foam models

2.2.1 Random Foam by Surface Evolver

The foams analyzed in this study are random soap froth microstructures generated using Brakke's *Surface Evolver* (1992) (Kraynik *et al.*, 2003). The numerical procedure starts with a primitive Voronoi froth with foam-like characteristics generated from randomly packed monodisperse hard spheres using molecular dynamics. Each Voronoi cell consists of all points that lie closest to a random seed, i.e., the center of each sphere. The Voronoi structure is then used as an initial condition in the Surface Evolver to generate a "dry" foam in which the liquid volume fraction is zero and the films can be modeled as two-dimensional surfaces. The software minimizes energy and balances mechanical forces by satisfying Plateau's laws: I. *the faces of cells are surfaces of*

constant mean curvature; II. *three faces meet at equal dihedral angles of 120°* ; and III. *four edges meet at the tetrahedral angle $\cos^{-1}(-1/3) \approx 109.47^\circ$* . For monodisperse foam the additional constraint that all cells have nearly the same volume is also applied. The relaxation process requires a large number of topological transitions that involve cell-neighbor switching. Since the solution is a local energy minimum, the surface area can be further reduced by subjecting the foam to large-deformation tension-compression cycles that provoke additional neighbor switching (*annealing*). The resulting structures are in very good agreement with Matzke's experimental study (1946) of monodisperse soap froth regarding types of polyhedra, distribution of polygonal sides, and ligament length distribution (see Kraynik, 2003, Kraynik *et al.*, 2003, 2004, 2005, 2006). The ligament lengths distribution for a model of 1728 cells is depicted in the frequency bar graph of Fig. 2.6. Clearly, the distribution follows closely the one shown for the aluminum foams in Fig. 2.5.

2.2.2 Anisotropy and Cropping

The models used in this study start as skeletal versions of such random microstructures formed by joining the cell vertices with straight lines, and result in cubical spatially periodic random soap froths of several sizes (N^3). A cluster of cells extracted from one of the soap froths generated, shown in Fig. 2.7a, illustrates the randomness of the microstructure as well as its essentially monodisperse nature. Anisotropy is introduced to the models by elongating ligaments with a projection in the x_1 -direction an amount that amplifies this projection by a factor λ while the projections in the x_2 - and x_3 - directions retain their original lengths. Figure 2.7b shows the same cluster of cells after this stretching process.

The periodicity of the models is then removed. To facilitate crushing simulations of the numerical foam model, ligaments in the top and bottom surfaces are cropped so that their ends become co-planar. Figure 2.8a shows a 3-D rendering of a soap froth having 10^3 cells before applying the anisotropy or cropping of ligaments in the top and bottom surfaces. Figure 2.8b shows a planar view of the same model after application of the affine deformation in the x_1 -direction and after cropping. Here, plates are placed at the top and bottom surfaces for visualization purposes.

2.3 Finite Element Modeling

2.3.1 Discretization and Material Distribution

The straight ligaments are sequentially “dressed” with shear-deformable beams with circular cross sections with variable area along their length that follows the expression developed in Jang *et al.* (2008) and is also included in Fig. 2.3:

$$A(\xi) = A_o f(\xi) = A_o (36\xi^4 + \xi^2 + 1), \quad \xi = x/\ell, \quad (2.1)$$

where A_o depends on the ligament length ℓ as follows

$$A_o = \bar{A}_o g(\eta) = \bar{A}_o (0.6633 + 0.2648\eta^{-2.5963}), \quad \eta = \ell/\bar{\ell}. \quad (2.2)$$

Here, \bar{A}_o and $\bar{\ell}$ are the average values of the measured mid-section cross sectional area and length respectively.

Modeling ligaments as beams leads to an overlap of material at the nodes. This extra material affects the calculation of the density of the model foam and must be corrected for. Following Jang *et al.* (2008), the overlap material is removed by cutting the ends of the beams. The corrected relative density is then expressed as

$$\frac{\rho^*}{\rho} = k \left(\frac{R_o}{\ell} \right)^n, \quad (2.3)$$

where R_o is the mid-span radius of the ligament and the parameters k and n depend on the anisotropy. The value of R_o is evaluated from Eq. (3) using $\rho^* / \rho = 0.08$ and the average length $\bar{\ell}$ of all ligaments in the stretched froth. Subsequently, the ligaments are placed into two groups: group 1 includes all ligaments that are shorter than $\bar{\ell}$, and group 2 includes the ligaments that are longer than $\bar{\ell}$. The average length of each group is designated as $\bar{\ell}_1$ and $\bar{\ell}_2$. The two average lengths are then used in Eq. (2) to establish corresponding values for $A_o |_{\bar{\ell}_a}$, $a = 1, 2$.

The ligaments are discretized with the LS-DYNA (2006) code using the Hughes-Liu beam element (1981) that is derived from the isoparametric 8-node solid element. The element allows for finite deformations of the beam axis, finite rotations of its normals as well as transverse shear deformations. The reference surface can be located either at the mid-surface of the beam or at an offset location, facilitating this way the contact on the actual surface of the beam, a key characteristic for the present problem. The element generates a constant moment along the length, which in the present problem implies that each ligament must be modeled with a sufficient number of elements.

Considering the order of the element, the non-uniformity of the cross sectional area, and issues related to ligament contact, special care needs to be taken regarding the number of elements in each ligament. Convergence studies resulted in discretizing ligaments belonging in the first group ($\ell < \bar{\ell}$) using 7 elements while those in the second group ($\ell \geq \bar{\ell}$) with 9 elements. All elements have a uniform circular cross sectional area based on the following expression:

$$A(\xi) = A_o |_{\bar{\ell}_a} f(\xi) |_{\bar{\ell}_a}, a = 1, 2 \quad (2.4)$$

where $A_o |_{\bar{\ell}_a}$ are the two cross sectional areas established as described in the previous section. The values of $f(\xi) |_{\bar{\ell}_a}$ for the two groups of ligaments are given in Table 2.1. Figure 2.9 shows 3D renderings of representative ligaments from each of the two groups (the images in Figs. 2.9a and 2.9b are respectively based on the average length of each group $\bar{\ell}_1$ and $\bar{\ell}_2$).

Table 2.1 Cross sectional area of beam elements for the two ligament groups

ξ	$f(\xi) _{\bar{\ell}_1}$	$f(\xi) _{\bar{\ell}_2}$
$ \xi \leq 0.18$	1.0	1.0
$0.18 \leq \xi \leq 0.34$	1.2425	-
$0.18 \leq \xi \leq 0.26$	-	1.0
$0.26 \leq \xi \leq 0.34$	-	1.3925
$0.34 \leq \xi \leq 0.42$	1.9122	1.9122
$0.42 \leq \xi \leq 0.5$	2.8484	2.8484

Inherent inside the random soap froth are a few ligaments (less than 1% of the total number of ligaments) with extremely small length i.e., $\ell \approx R_o$. In an explicit finite element analysis, where a stable time increment is related to the smallest element length, keeping the previous mesh scheme for these ligaments would result in an excessive increase in the computational cost. Therefore a special discretization using 1-3 elements was used in order to remedy this issue.

A summary of the procedure to generate the random foam model, from the soap froth to the discretized model with properly assigned cross sectional areas, is shown with the use of a flowchart in Appendix A (Fig. A1).

2.3.2 Contact Implementation

Contact between ligaments of crushing cells is the mechanism through which local collapse is arrested enabling the spreading of crushing to neighboring and other cells. Consequently, the modeling of contact plays a crucial role in the ability of the model to reproduce the stress plateau and the second hardening regime associated with densification observed in experiments. An important improvement in the present effort is the more representative modeling of contact that is facilitated by the general automatic contact algorithm of LS-DYNA. The algorithm generates a circular cylindrical contact surface for every element, which here corresponds to the circular cross sections of the elements.

A standard penalty formulation is used with an interface stiffness chosen to be of the same order of magnitude as the stiffness of the contacting elements. At every step of the analysis penetrations are investigated along the length of each element by finding the intersection point between nearby beam elements and checking to see if their outer surfaces overlap. If they do, the contact force is computed and is applied to the nodal points of the interacting elements.

As noted above, the use of beam elements leads to excess material at the nodes. This excess material was corrected for the calculation of the density of the model but the overlaps remain in the numerical model. The overlapping material causes local non-physical contacts that lead to numerical instabilities. This issue was resolved by excluding the two elements adjacent to the nodes from developing contact. Note here, that the group of very short ligaments is also excluded from the contact definition because of initial interpenetrations.

Friction between contacting ligaments was also found to play an essential stabilizing role to the numerical solution. Coulomb friction with a coefficient of 0.4 was thus included in the contact definition. Friction prevents “dynamic” sliding between ligaments especially when the compressive force increases during the densification regime. We note here that a way to reduce the significant computational cost of the

contact algorithm (especially in quasi-static loading performed with explicit analysis) is to delay its activation until an average deformation of 2-3% is reached.

2.3.3 Density Correction

The mass density ρ of the Al alloy was assigned the value of 2690 kg/m³ (0.09718 lb/in³). The overlap at the nodes results in an overestimation of the inertial forces. Since the four ligaments contribute material to each node, this issue was remedied by scaling the density of the two elements in each of the four intersecting ligaments by 0.25. The effectiveness of this approximation was evaluated by numerically weighing each numerical model and ensuring that its weight corresponds to a foam density within the range $0.0785\rho - 0.0825\rho$.

2.3.4 Material Behavior

The foam Al alloy is treated as an elastic-plastic solid assigned the stress-strain properties measured in an independent tensile test by Jang and Kyriakides (2009b) reproduced in Fig. 2.10. The measurements were well fitted with a Ramberg-Osgood fit

$$\varepsilon = \frac{\sigma}{E} \left[1 + \frac{3}{7} \left(\frac{\sigma}{\sigma_y} \right)^{n-1} \right] \quad (2.5)$$

with parameters: $E = 10^4$ ksi (69 GPa), $\sigma_y = 28$ ksi (193 MPa), $n = 48$. The material model 24 - Piecewise Linear Isotropic Plasticity within LS-DYNA is used.

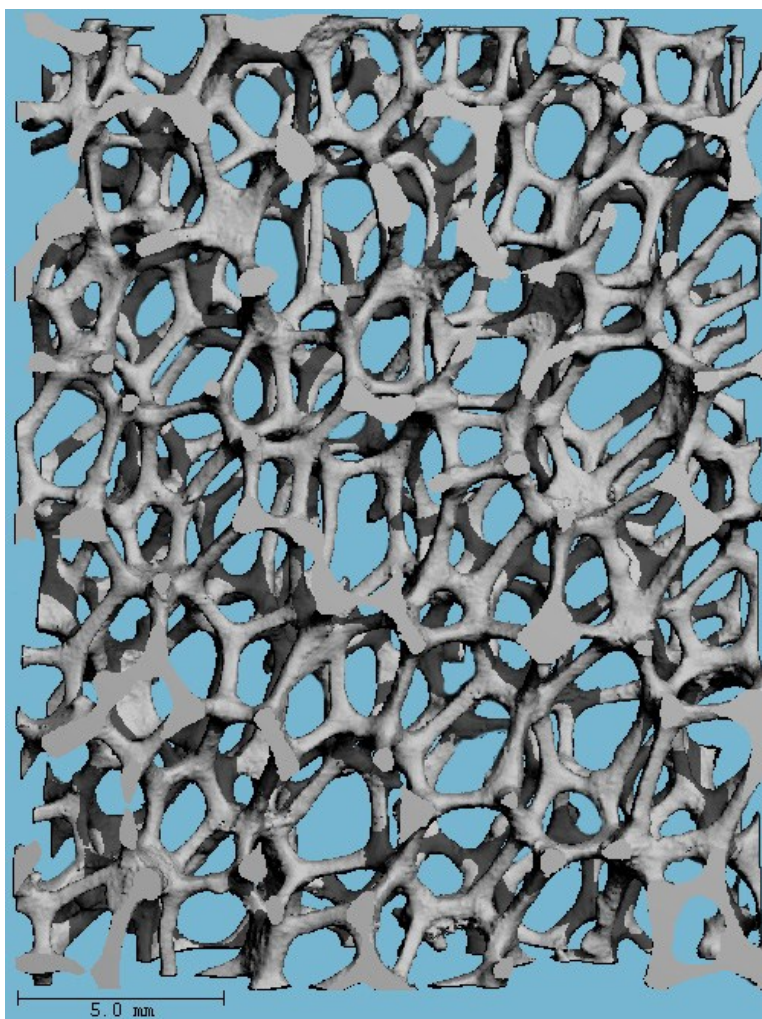
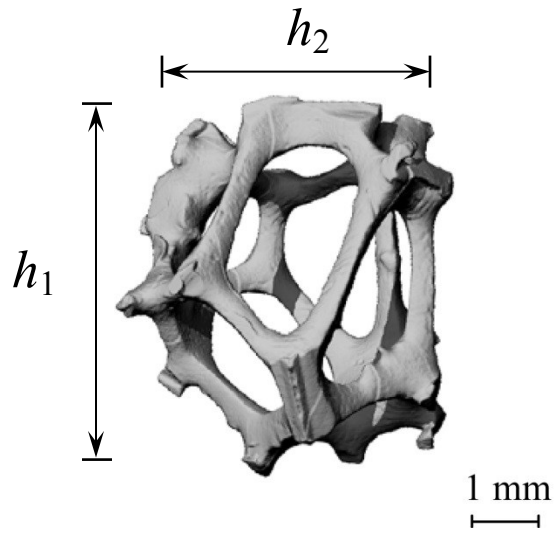
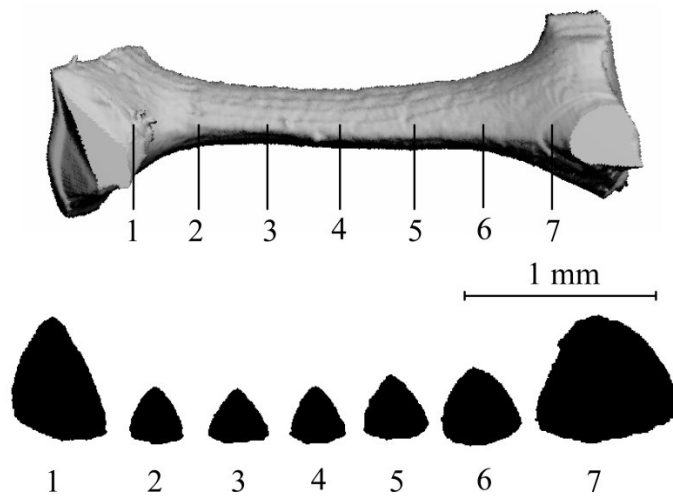


Fig. 2.1 Computed tomography image of a slice of a 10 ppi Al foam ($\rho^* / \rho \approx 8.2\%$)



(a)



(b)

Fig. 2.2 (a) Cell extracted from a 10-ppi Al foam illustrating irregular polyhedral geometry and elongation in the rise direction and (b) ligament extracted from the same foam and cross sectional views (from Jang *et al.*, 2008).

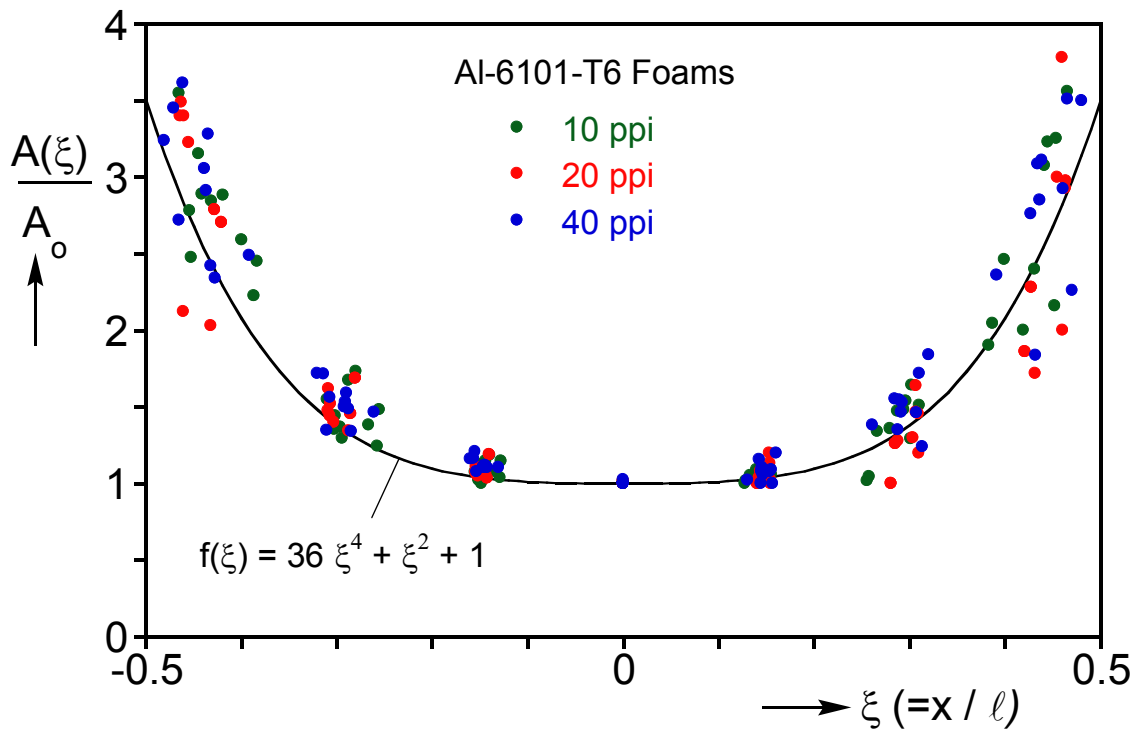


Fig. 2.3 Measured variation of ligament cross sectional area along the length fitted with function $f(\xi)$ (from Jang *et al.*, 2008).

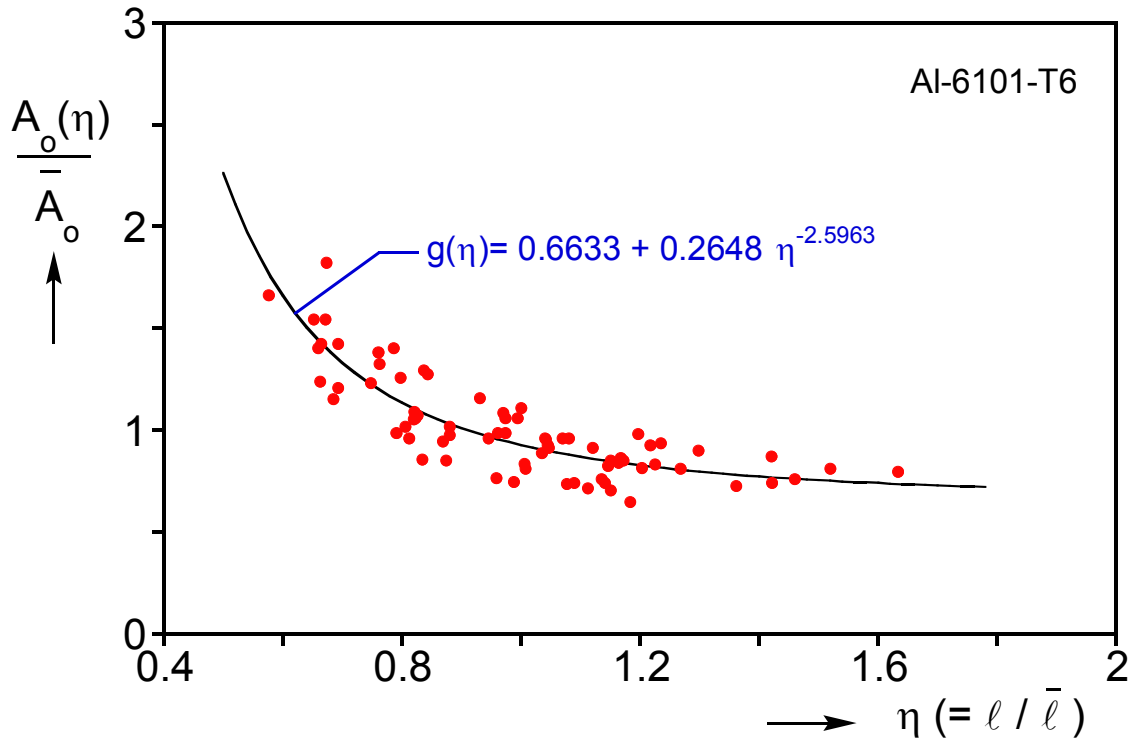


Fig. 2.4 Measured mid-span cross sectional area as a function of normalized length fitted with function $g(\eta)$ (from Jang *et al.*, 2008).

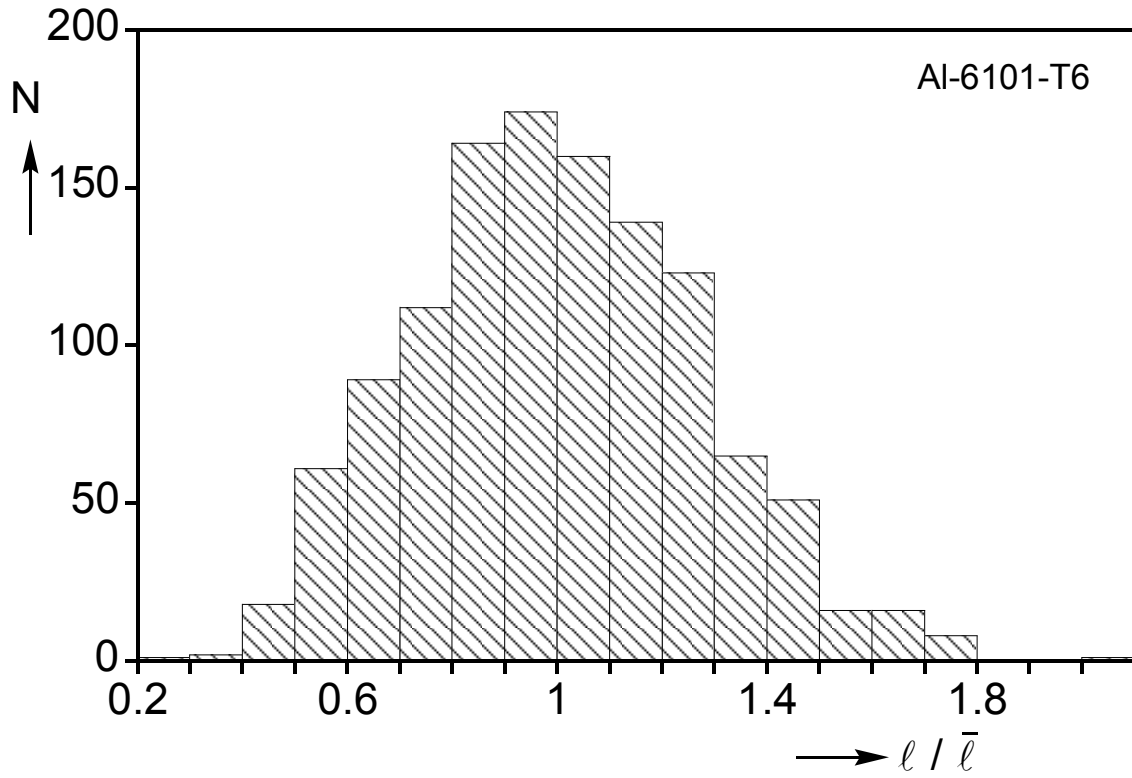


Fig. 2.5 Plot of frequency vs. normalized length for the Al foam (from Jang *et al.*, 2008).

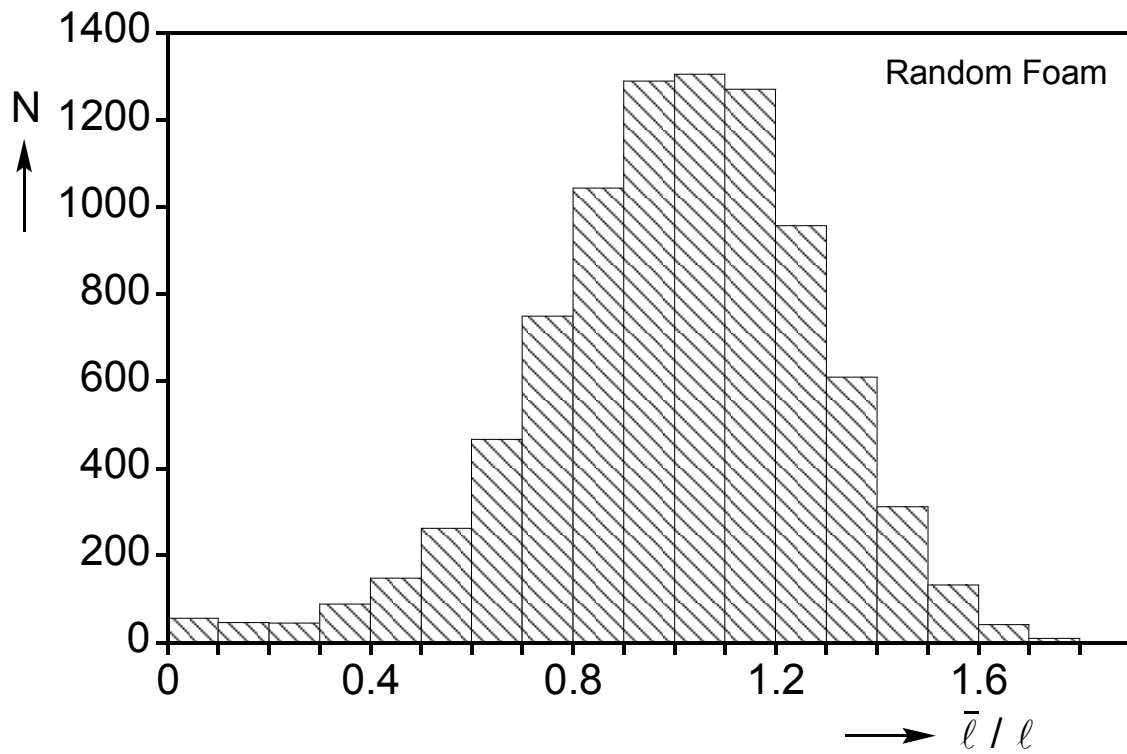
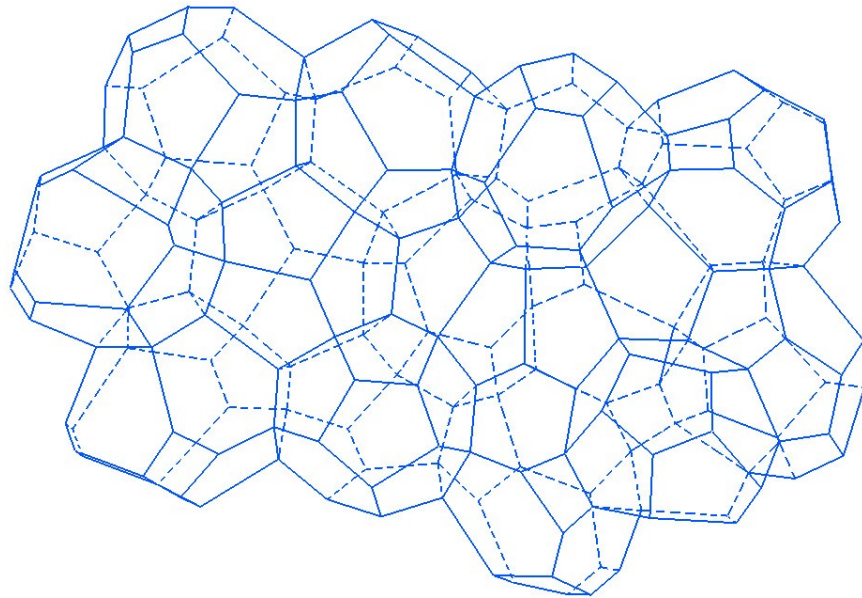
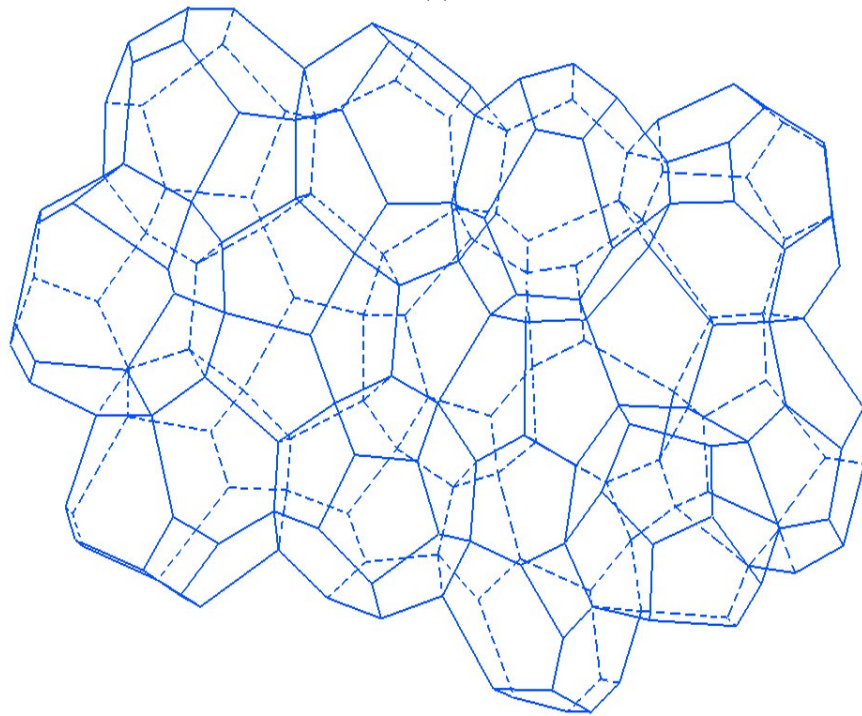


Fig. 2.6 Plot of frequency vs. normalized length for a 12^3 cells random foam model.



(a)



(b)

Fig. 2.7 (a) Skeletal drawing of cells extracted from a random foam model. (b) Same cells after anisotropy $\lambda = 1.2$ is applied.

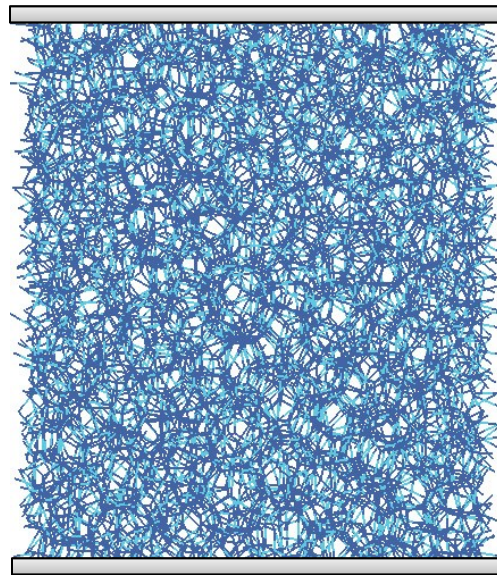
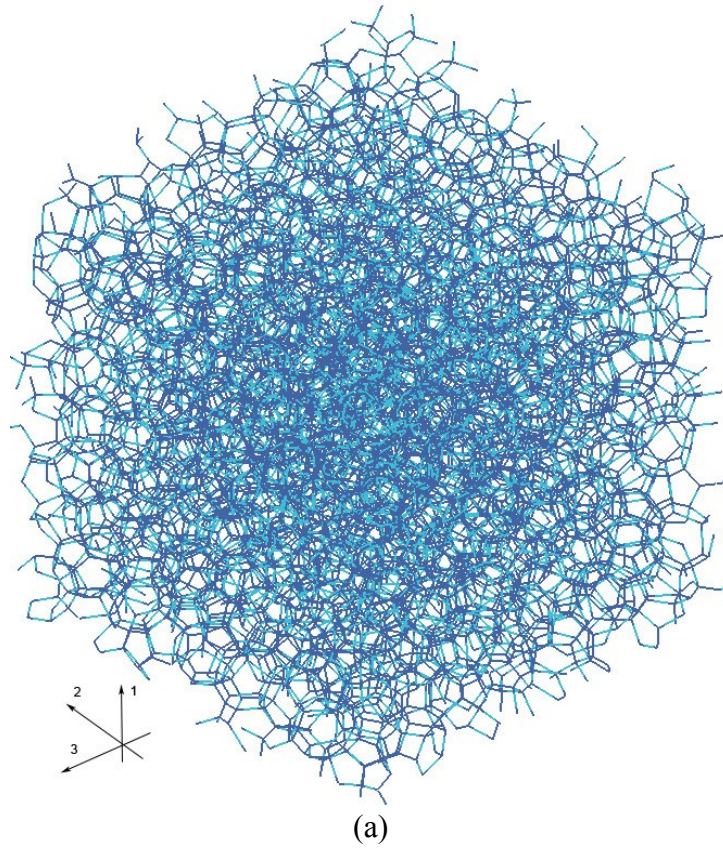
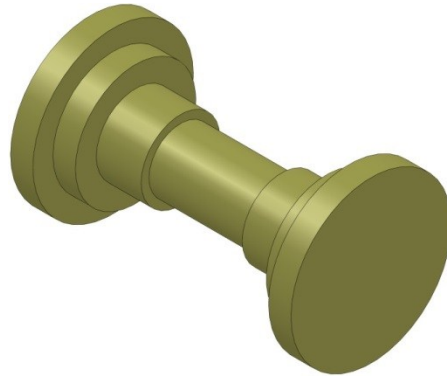
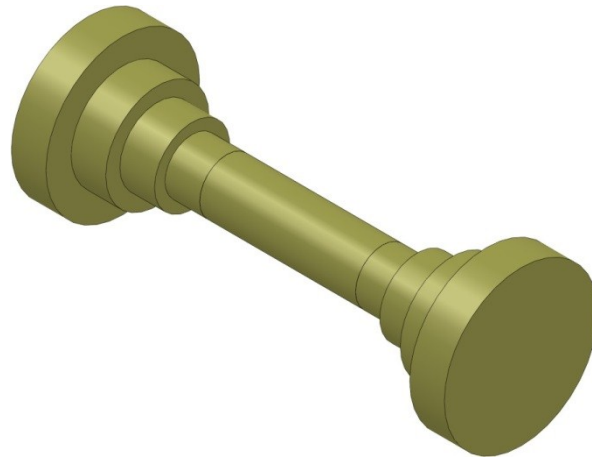


Fig. 2.8 (a) 3-D rendering of a random soap froth with 10^3 cells. (b) Front view of the same model after anisotropy is applied ($\lambda = 1.2$); ligaments are cropped and rigid plates are placed on top and bottom surfaces.



(a)



(b)

Fig. 2.9 FE discretization and cross sectional area variation of a ligament with (a) $l < \bar{l}$ and (b) $l \geq \bar{l}$.

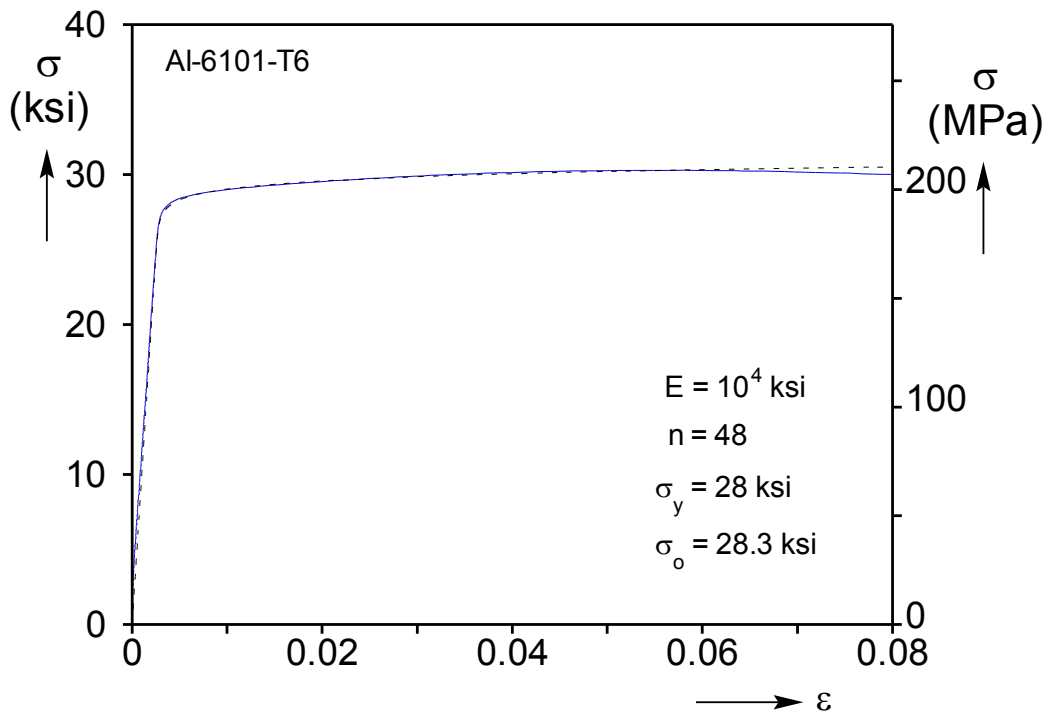


Fig. 2.10 Stress-strain response of Al-6101-T6 foam base material

Chapter 3: Quasi-static Crushing

A number of experimental studies on both open-cell (e.g., Gibson *et al.*, 1989; Triantafillou *et al.*, 1989; Bart-Smith *et al.*, 1998; Nieh *et al.*, 2000; Gioux *et al.*, 2000; Zhou *et al.*, 2002, 2004; Zhou and Soboyejo, 2004; Montanini, 2005, etc.) and closed-cell foams (e.g., Thornton and Magee, 1975; Simone and Gibson, 1998, Gioux *et al.*, 2000; Montanini, 2005; etc.) can be found in the literature. Jang and Kyriakides (2009a) performed a series of uniaxial compression tests on the Al foams analyzed in Chapter 2. These include crushing tests and combined crushing-scanning tests, performed in both the rise and the transverse directions. The compressive response exhibits the usual characteristics of cellular materials: an initial stiff elastic response that terminates into a limit load, followed by localized crushing that tends to spread at relatively constant load. When most of the cells are crushed the response becomes stable again with a second stiffening branch (*densification*).

The effectiveness of the modeling framework described in the previous chapter in reproducing such compressive responses is first evaluated in this chapter. Quasi-static crushing simulations in the rise and transverse directions are performed and the results are compared directly with the corresponding experimental ones from Jang and Kyriakides (2009a). The comparison is made in terms of both stresses and the evolution of associated crushing patterns from the limit load to densification. Other issues examined include the domain size, differences in the calculated response by altering the random microstructure, and a comparison with previously calculated Kelvin cell responses.

3.1 Experimental Crushing Responses

3.1.1 Rise Direction Experiments

We start with a short review of the results reported in Jang and Kyriakides (2009a), which will serve as a point of reference for our modeling framework. The main characteristics of the foam response in the rise direction and the associated events were demonstrated through a compression test on a 10-ppi specimen (Exp. R10-2, 50 mm side cubical specimen). This particular specimen was crushed between rigid platens incrementally. Between increments the specimen was unloaded, removed from the testing machine, placed in the micro-CT and scanned. This procedure enabled a detailed depiction of the evolution of plastic deformation in the whole specimen. Figure 3.1 shows the recorded stress-normalized displacement response. Figure 3.2 shows images of the initial and five deformed configurations of a full cross section of the specimen (the images are 0.35 in (9mm) from one of the faces). The configurations correspond to locations on the response marked with circled numbers. Isometric views of the specimen for the same configurations are shown in Figure 3.3.

The response exhibits an initial linear regime that terminates in a local load maximum at a stress of $\sigma_{I1} = 456$ psi (3.14 MPa). During the linear part of the response the specimen deformation is macroscopically homogeneous. The limit load is a sign that localization of deformation has commenced somewhere within the specimen. The elastic modulus of the foam was measured from the first unloading and found to be $E_1^* = 8.57 \times 10^{-3} E$ (E is the elastic modulus of bulk Al-6101-T6). The response drops down to a local minimum close to the 2nd unloading position and then traces a ragged plateau. At approximately 50-55% average strain, the response follows a second stiffening branch that corresponds to the densification of the foam.

A more global view of what had taken place can be seen in the full specimen images in Figs. 3.2 and 3.3. In image ①, an inclined band of crushed material at one third of the height of the specimen (above the lower faceplate) crosses the specimen from left to right. This is met around mid-width by a second band that emanated from the lower right-hand corner of the specimen. A 3D view of the specimen in image ① of Fig. 3.3 shows that this crushing zone is not planar, as the crushed band is also inclined in a plane perpendicular to the original one. By configuration ②, the crushing has consumed the lower one-third of the specimen with a few cells bonded to the faceplate remaining intact. By configuration ③, the crushing has consumed the lower 60% of the specimen and the crushing front is now more planar and nearly parallel to the faceplates. The crushing front continues to move upward (see images ④) but with a gradual increase in the load. The last image (⑤) was taken at $\delta/H = 55\%$ and, as can be seen, most of the cells have crushed with a few bonded to the two faceplates remaining intact. Subsequently, further crushing requires an increasingly higher load as the material is now in the densified regime.

This sequence of events is reminiscent of that reported in Papka and Kyriakides in the case of in-plane crushing of polymeric (1998a) and metallic honeycombs (1998b). By contrast, in similar compression tests on polyester urethane foams that are essentially elastic, Gong and Kyriakides (2005) noted that crushing was initiated by a long-wave buckling mode that affected the whole specimen and subsequently lead to the formation of many localized bands of crushed cells. Clearly, no long-wave buckling was observed in the Al foams tests described here and the crushing spread mainly by the propagation of collapsing cells.

3.1.2 Transverse Direction Experiments

A similar series of tests was performed for specimens prepared in the same manner but loaded in the transverse direction. A set of measured stress-displacement responses is shown in Figure 3.4. The responses are similar to ones recorded in the rise direction but with a few characteristic differences. First, because of the anisotropy, the limit load is lower while the initiation peak is less distinct and in some cases even indistinguishable. The stress plateau is smoother and more flat, while the load increase leading to densification initiates at a smaller average strain. The initiation and propagation of collapse happens in the same way as in the rise direction and is not going to be repeated here.

3.2 Numerical Results with Random Foam Models

3.2.1 Model Parameters and Boundary Conditions

The performance of the modeling framework outlined in Chapter 2 is now evaluated using results from a quasi-static numerical simulation of crushing of a 10^3 cell model. The model has a relative density of 8.0% and an anisotropy of $\lambda = 1.2$, both representing average values of the specimens tested in Jang and Kyriakides (2009a). An $x_1 - x_2$ view of a slice of this model is included in Fig. 3.5. The image shows the ligaments dressed up as solid beams with variable cross sections. Plates have been added to the top and bottom surfaces to help visualization of the model. The actual boundary conditions are that all nodes that intersect these two planes in the undeformed configuration are fixed to the planes. The bottom plate is also fixed in space while the top is displaced incrementally downward gradually compressing and crushing the model. The four lateral surfaces are left free from constraints.

LS-DYNA is an explicit code and thus care must be taken when deforming solids quasi-statically to ensure that inertia effects do not influence the response. This was achieved by selecting the rate of the applied displacement increment so that the kinetic energy remained very small compared to the internal energy. Displacement of the top plane with respect to time was given by the function

$$u(\tau) = u_o + (u_1 - u_o)\tau^3(10 - 15\tau + 6\tau^2) \quad (3.1)$$

where $\tau = (t - t_i) / (t_{i+1} - t_i)$. For the results that follow, the internal energy is several orders of magnitude larger than the kinetic energy at every step of the simulation. A model of this size ends up with approximately 87,250 elements and more than 500,000 degrees of freedom. This, plus the incremental solution procedure that must be followed translate into a requirement for significant computational resources for a complete crushing response.

3.2.2 *Crushing in the Rise Direction*

Figures 3.6 to 3.9 show results for crushing the model in the rise direction (x_1). The calculated engineering stress-shortening ($\sigma_{11} - \delta_1 / H_1$) response is shown in Fig. 3.6 where H_1 is the initial height of the model. Figure 3.7 shows a set of representative deformed configurations of a slice of the model corresponding to the numbered bullets marked on the response. The slice was extracted from nearly the center of the domain and for clarity is only $0.15 H_2$ thick—one-cell and one half (similar to the X-ray tomography images of Fig. 3.2). The initial configuration (©) clearly shows the cropping of the top and bottom surfaces but not on the sides.

The response exhibits the same general characteristics as those seen in physical crushing experiments (e.g., compare with Fig. 3.1). It starts with an initial elastic part with a modulus of $E_1^*/E=1.1\%$, a value that is somewhat higher than corresponding measured values in Table 2 of Jang *et al.* (2010). The present model was developed for best performance in the prediction of the overall crushing response where contact is a main challenge. Consequently the discretization and type of element adopted were guided by this objective. Previous models developed in an implicit code yield somewhat more accurate values of the elastic modulus.

As the stress increases, some plastic deformation sets in leading to a gradual degradation of the modulus and eventually to the attainment of a load maximum. The maximum stress attained, defined as the initiation stress of the foam, is $\sigma_{I1} = 446$ psi (3.08 MPa), a value that compares well with corresponding experimental results and predictions from the random model of Jang *et al.* (2010) developed in ABAQUS standard.

Up to this point, cell deformation was distributed essentially uniformly through the domain. Following the load maximum, deformation starts to localize at the “weakest” sites. To illustrate this point we include in Fig. 3.8 four zoomed-in deformed configuration of the zone marked with a red box in the undeformed full image of the slice in Fig. 3.7. The locations of these images are marked on the initial response that is plotted expanded in the inset. Image **1** corresponds to the load maximum and the other three to progressively larger values of δ_1 during the load drop that follows the maximum. In image **2**, ligaments in the circled area are seen to have bent visibly, collapsing at least one cell. In image **3** a bit later, the local deformation has spread to neighboring cells and in image **4** the ligaments of several of the affected cells have come into contact.

At a larger value of δ_1 , the localized collapse has evolved into a band that spans essentially the width of the domain as shown in image ① in Fig. 3.7. This band has a slightly negative slope on the left but becomes nearly horizontal on the right. In an effort to investigate how the band evolves across the domain, Fig. 3.9 compares images from nearly the front (I-1), the middle (I-2) and the back (I-3) of the domain at a point somewhat after configuration ① at $\delta_1/H_1 = 10.8\%$ (approximate locations shown in accompanying figure). The central band of collapsed cells in I-2 has broadened and became more horizontal. In image I-3 near the back of the domain, the band is at a higher location, it's nearly horizontal on the left but has an upward orientation on the right. In image I-1 closer to the front of the domain, the band is somewhat lower than in the center, is nearly horizontal on the left and has an upward inclination on the right. In other words the crushing band has a 3-D relief that follows local weaknesses in the microstructure. This conclusion is in agreement with the experimental observation of Jang and Kyriakides (2009a) albeit made in a larger specimen (see also Fig. 3.3).

Returning to the global response in Figs. 3.6 and 3.7, in configuration ② at $\delta_1/H_1 = 19.7\%$ the crushing has spread mainly downwards and covers approximately 25% of the height while the stress has remained essentially unchanged. In configuration ③ at $\delta_1/H_1 = 27.1\%$, the crushing zone has moved further down and also started consuming cells from the upper third of the domain. This deformation took place while the stress remained again nearly unchanged. As the crushing band spreads, it occasionally encounters stiffer and stronger cells that require higher stress to collapse. Such encounters are responsible for the stress undulations on the response. The smaller the domain or specimen the more pronounced the undulations tend to be. In crushing experiments involving relatively large number of cells, the amplitude of such undulations decreases and the response appears smoother. By contrast, for coarser cellular materials

of finite size the undulations are more pronounced. If the microstructure is also regular, like the circular honeycomb of Papka and Kyriakides (1998), then the undulations also have well defined periods and amplitudes.

In configuration ④ at $\delta_1 / H_1 = 35.6\%$, the band has moved in both directions and consumes more than two thirds of the domain. Its fronts now engage cells that are adjacent to the cells and ligaments that are fixed to the “end plates” making them stiffer and stronger, thus crushing them requires additional effort, which is reflected in the upswing of the response. Initially, the increase in stress is small but continues to pick up as the last rows of cells next to the boundaries are crushed as seen in configuration ⑤ at $\delta_1 / H_1 = 46\%$. The material has now densified and continued compression requires increasingly higher stress. During the subsequent part of the response, remaining hard zones are collapsed and partially collapsed zones become more compacted.

Overall, the cell crushing resembles very closely what was observed using X-ray tomography in the experiments of Jang and Kyriakides (2009a). This, of course, is the main improvement over Kelvin cell models afforded by analyzing a more realistic random microstructure. As reported in Jang and Kyriakides (2009a), the measured overall crushing responses from the three foams analyzed exhibited some variations. The three foams with 10, 20 and 40 ppi cell sizes were supplied in blocks of $4 \times 12 \times 14.5$ in ($102 \times 305 \times 368$ mm). The respective average relative densities of the blocks were 8.23%, 7.50% and 7.54% and the average anisotropies 1.27, 1.24 and 1.18 (Table 1 of Jang and Kyriakides, 2009a). Four inch tall specimens with a two-inch square base were extracted from the blocks by wire EDM and then cut in half producing the 2-inch cubical specimens. Measurements performed on the individual specimens showed that both the density and anisotropy varied within each block and even within each specimen. Furthermore, variations of both variables were observed to occur through the height of

the blocks. An additional complication, reported in Jang *et al.* (2008), is that dispersed throughout the foams were cells with small closed faces. These occurred at sites where in the polymeric foam templates small quadrilateral faces existed (see Fig. 8 of the same reference). The collective effect of these factors is the observed variation in the mechanical properties. This variation was also responsible for our decision to adopt in the models a relative density of 8.0% and an anisotropy of 1.2, values that approximately represent the averages of all foams considered. Thus, the numerical model rather than being representative of a particular specimen it represents the whole set. With this in mind, the calculated crushing response is compared in Fig. 3.10 with two measured responses that approximately bound the experimental results. The calculated response has all the features of the experimental ones while being closer to the response from specimen R10-3. In addition, the model produced a slightly less stiff response than the experiments at average strains higher than 60%. Considering the differences between the foams tested and the idealizations introduced in the random foam model, the comparison is deemed as being very complementary.

3.2.3 Effect of Domain Size and Structure Variations

The random nature of the microstructure of the soap froth models, generated using the Surface Evolver software, implies that no two models are the same. Of course this is also the case in the real foams tested. Consequently, some difference in the calculated response can be expected between models of the same size, dressed in the same manner, and assigned the same density and anisotropy. Figure 3.11 compares the calculated response from two 10^3 cell models: model I is the one presented this far and model II is a second one. The general trend of the two responses is very similar with the elastic modulus, the initiation stress, the plateau stress and its extent having similar

values. The observed difference is due to microstructural differences that lead to different evolution of crushing. The extent of the difference in such responses is expected to decrease as the size of the domain increases. It is also worth mentioning that the difference between the two calculated responses is smaller than differences observed in experiments on foams from the same block, because here the anisotropy and density are fixed.

In Jang *et al.* (2010) it was pointed out that the initiation stress calculated with their random foam models was influenced by the size of the domain considered. Sensitivity of the crushing response calculated with the present model to the domain size was examined using models with 6^3 , 8^3 , 10^3 and 12^3 cells each generated independently. The models were dressed with beam elements in the same manner and were assigned the same density and anisotropy. The four calculated responses are compared in Fig. 3.12. Clearly, the response is sensitive to the domain size as a distinct upward shift is observed in going from the 6^3 to the 8^3 domain. A smaller increase occurs when the domain is increased to 10^3 cells and near convergence is observed between the 10^3 and 12^3 cell domains. This size effect has been observed before and is attributed to the effect of the free lateral sides of the model. In view of the convergence observed in Fig. 3.12 the 10^3 cell size model was adopted in the simulations performed.

3.2.4 Crushing in the Transverse Direction

The same 10^3 cell foam model was used to simulate the compression in the transverse direction experiments. The model was assigned the same density and anisotropy. In this case, two lateral sides were appropriately cropped so that their ends could become co-planar while the other four sides remained as generated (see

configuration ⑩ in Fig. 3.14). The cropped sides were then fixed to parallel planes to accommodate the incremental compression of the model.

A calculated stress-displacement ($\sigma_{22} - \delta_2 / H_2$) response from a lateral compression simulation is shown in Fig. 3.13 and a set of corresponding deformed configurations in Fig. 3.14. It exhibits an initial load maximum, an extended stress plateau and a rising stress beyond average displacement of about 30%. In this direction the somewhat flattened cells are easier to collapse. A related observation is that the response is smoother with fewer and smaller amplitude undulations, again a feature shared with the experimental results. Included in Fig. 3.13 are two representative experimental responses. They are seen to agree quite well with the calculated response except that once more the numerical one is somewhat softer in the densification regime $\delta_2 / H_2 > 60\%$.

The crushing configurations exhibit once again localized crushing bands with a relief across the width and depth of the domain (see upper middle part in image ① of Fig. 3.14). Between configurations ② to ④ the crushing band broadens covering most of the central half of the domain. Intact cells in the upper and lower edges of the domain require additional stress in order to collapse due to the support provided by the rigid planes. Consequently, for $\delta_2 / H_2 > 30\%$ the stress starts to gradually increase and by configuration ⑤ most of the cells have collapsed. Crushing of remaining “hard” spots requires a further increase in stress as the material enters now the densified regime.

To facilitate comparison between crushing in the rise and transverse directions the two responses are plotted together in Fig. 3.15. It is clearly seen that in the transverse direction the limit stress is significantly smaller and the same holds for the stress drop following the limit load. The plateau is smoother with less undulations and about 80 psi (or 20%) lower than the corresponding one in the rise direction. Furthermore, the gradual

load increase leading to densification initiates at a smaller average strain. This observation is reinforced by looking at the deformed configurations ④ of Fig. 3.7 and ⑤ of Fig. 3.14 which both correspond to a normalized displacement of approximately 35%. In the first case (rise direction), the cells near the fixed edges are intact and about to collapse while in the latter case (transverse direction) all cells have collapsed and the foam starts to densify.

3.3 Random Foam Modeling vs. Kelvin Cell Models

The idealization of the foam microstructure with the periodic 14-sided Kelvin cell (Thompson, 1887) shown in Fig. 3.16 has proved very effective in the construction of numerical models that produce accurate estimates of the mechanical properties of open cell foams (e.g., see Warren and Kraynik, 1997; Zhu *et al.*, 1997; Laroussi *et al.*, 2002; Gong *et al.*, 2005a; Gong and Kyriakides, 2005; Gong *et al.*, 2005b; Jang and Kyriakides, 2009b). In this section, we compare the strengths and weaknesses of Kelvin cell models with respect to the random modeling framework. In particular, the comparison is made on the implementation of these two approaches as described in Jang and Kyriakides (2009b) and Gaitanaros *et al.* (2012).

3.3.1 Kelvin Cell and Random Foam Modeling Similarities and Differences

The Kelvin cell is regular, space-filling and periodic, which facilitates efficient construction of numerical models. By contrast, random foam models have to be generated through the Surface Evolver as outlined in §2.2.1. Ligaments in Kelvin cell models are discretized with 8 quadratic shear-deformable beam elements in every ligament. Contact between ligaments is introduced by the use of spring elements in ABAQUS. Discretization in random foam models is performed by using 7 or 9 (depending on the ligament length) *degenerate* (C^0) beam elements as described in §2.3.1. The general

beam-to-beam contact algorithm implemented in LS-DYNA is applied to all discretized ligaments.

Essential components of both modeling frameworks are the introduction of the appropriate anisotropy, the actual mechanical properties of the base material into the microstructures, and finally the “dressing” of ligaments with solids.

3.3.2 Kelvin Cell and Random Foam Modeling Performance

The regular geometry of the Kelvin cell makes it easy to use in terms of mesh and boundary conditions (e.g., a uniform mesh is sufficient). Its initial elastic response can be captured by focusing on a characteristic cell (see Fig. 3.16). Furthermore, for the elasto-plastic foams examined here, the initial yielding and the load maximum were shown to also be captured by consideration of a characteristic cell. This is the case because the onset of instability is governed by the single cell response. This is to be contrasted with corresponding instabilities in elastic (polymeric) foams of similar geometry where long wave buckling modes are preferred. Since for this family of monodisperse foams, characteristic cell calculations were shown to reproduce the elastic and initial inelastic behavior accurately, they provide a strong platform for parametric studies.

The crushing behavior beyond the limit load requires consideration of a multi-cell 3D domain. These 3D models have been shown to reproduce accurately the complete compressive response (see Fig. 3.17) of Al alloy open cell foams. Since contact is modeled through spring elements that get activated when a certain gap is closed, the densification strain is affected by the choice of the activation gap and thus is calibrated for best performance.

Despite these advantages, Kelvin cell models have certain limitations and disadvantages: they are only applicable to monodisperse foams and, even then, they result

in crushing patterns that differ from those of actual foams. This happens because crushing patterns are influenced by the regularity of the microstructure (see Fig. 3.18a).

The microstructure of random foam models on the other hand makes them challenging to implement and special care is needed for an effective discretization that provides accuracy and stability for the complete response. Because of the randomness of the microstructure, no unit cell exists. Moreover, as the convergence study reported in Chapter 2 has shown, a domain of at least a 1000 cells is needed for the minimization of boundary effects. In addition, the initial part of the random model response, i.e., the elastic modulus and the initiation stress, is somewhat stiffer than that predicted by Kelvin cell models which tends to be closer to measured values. At the same time, the random models provide accurate predictions of the complete crushing responses along with realistic crushing patterns (see Fig. 3.18b). Clearly, the random modeling framework is more general and can be applied to other foam microstructures such as ones with varying degrees of polydispersity. Furthermore they can be easily extended to multiaxial loading settings or ones involving inertial effects.

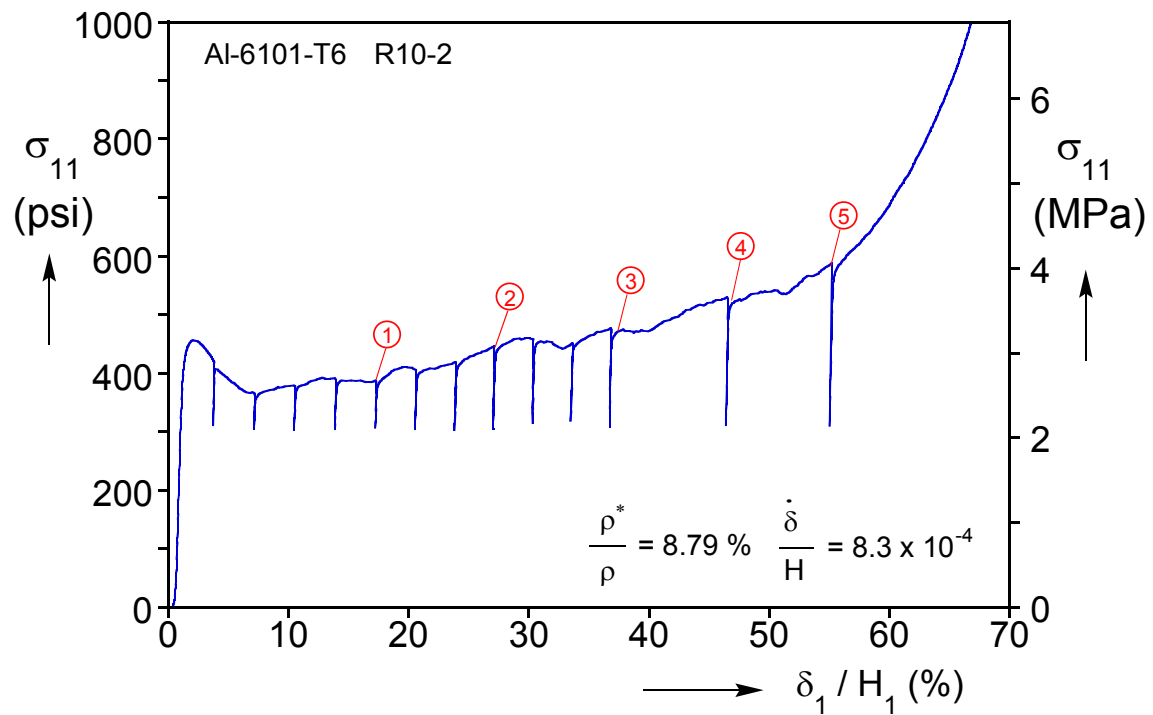
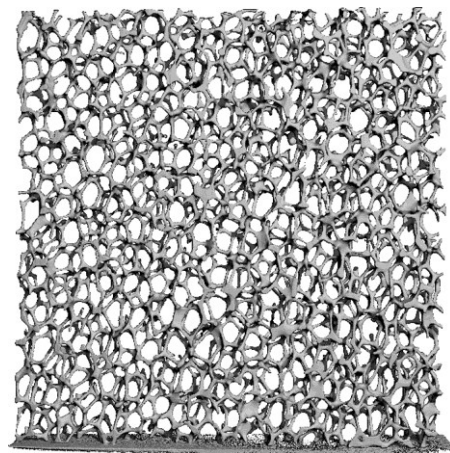
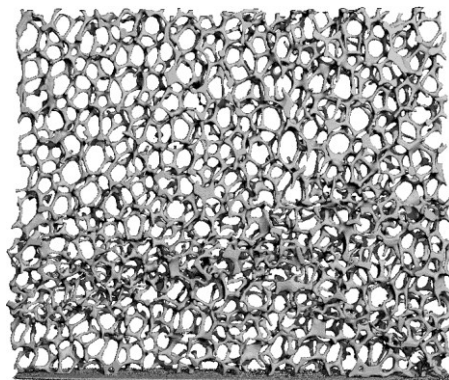


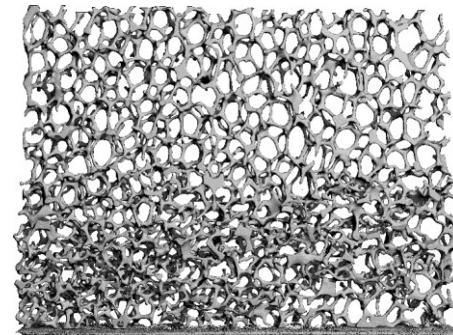
Fig. 3.1 Typical compressive response of an Al alloy open-cell foam (crushing in rise direction; from Jang and Kyriakides, 2009a).



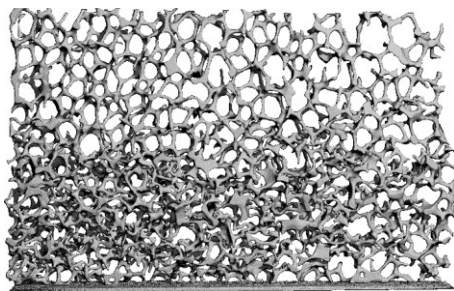
①



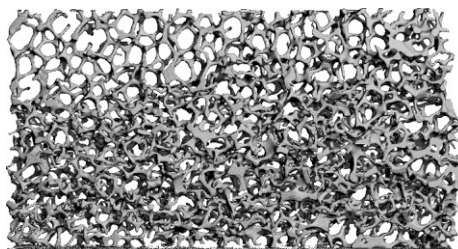
②



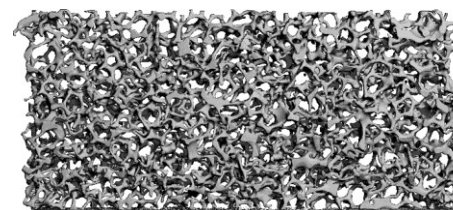
③



④



⑤



⑥

Fig. 3.2 Sequence of deformed configurations corresponding to points ① to ⑥ on the response of Fig. 3.1 (from Jang and Kyriakides, 2009a).

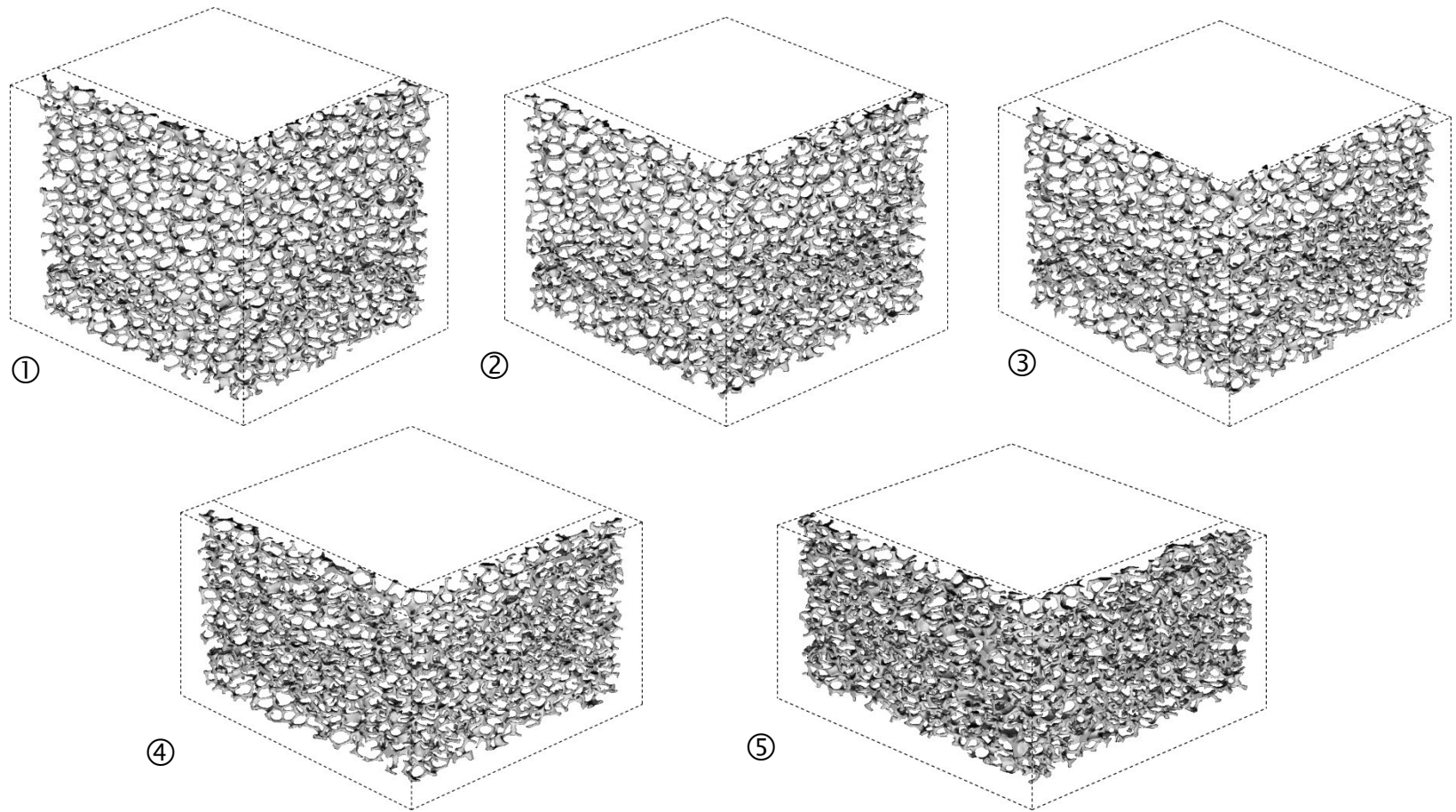


Fig. 3.3 Sequence of 3-D images of two perpendicular planes corresponding to points ① to ⑤ on response in Fig. 3.1 (from Jang and Kyriakides, 2009a).

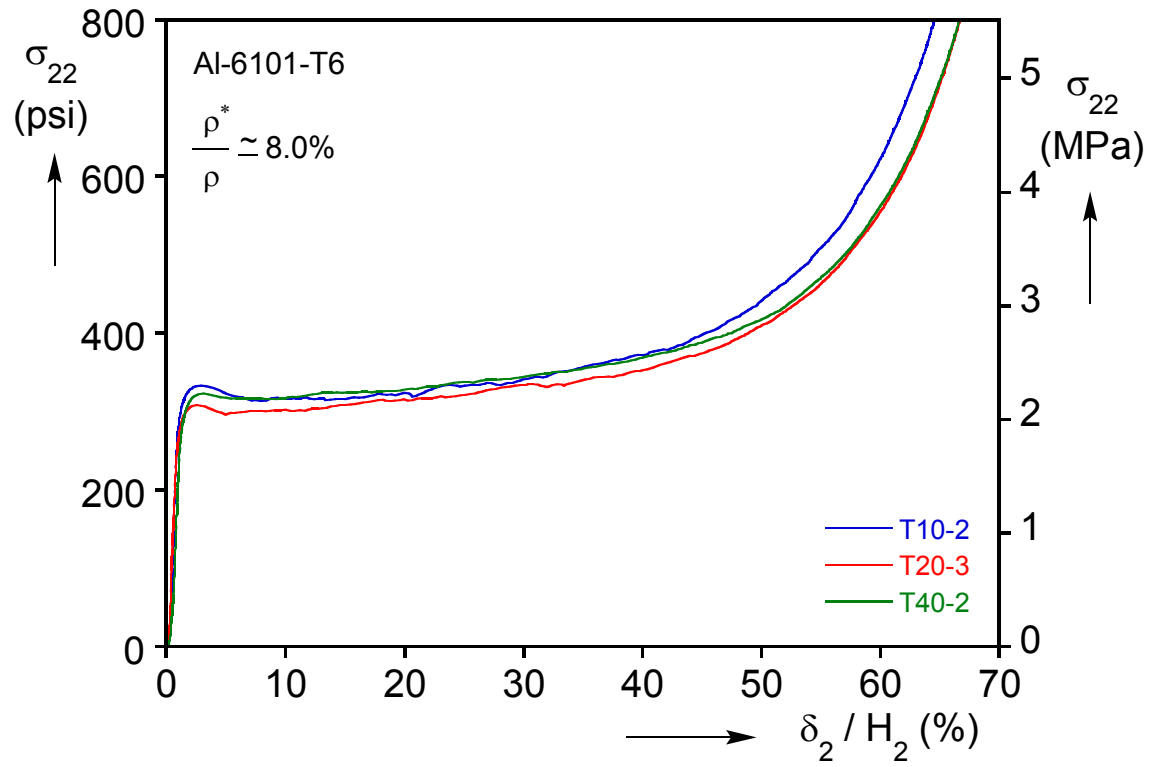


Fig. 3.4 Compressive responses in the transverse direction for different cell size foams (from Jang and Kyriakides, 2009a).

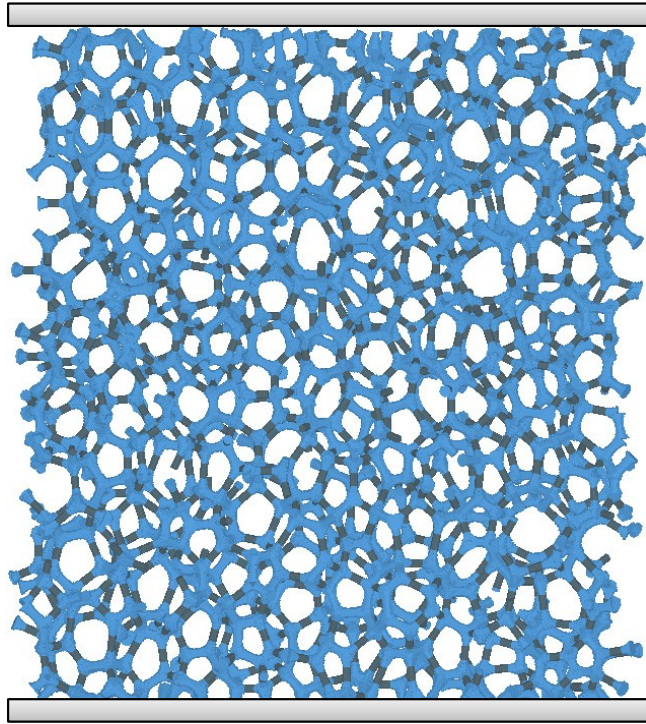


Fig. 3.5 Front view a 10^3 cell model with anisotropy $\lambda = 1.2$.

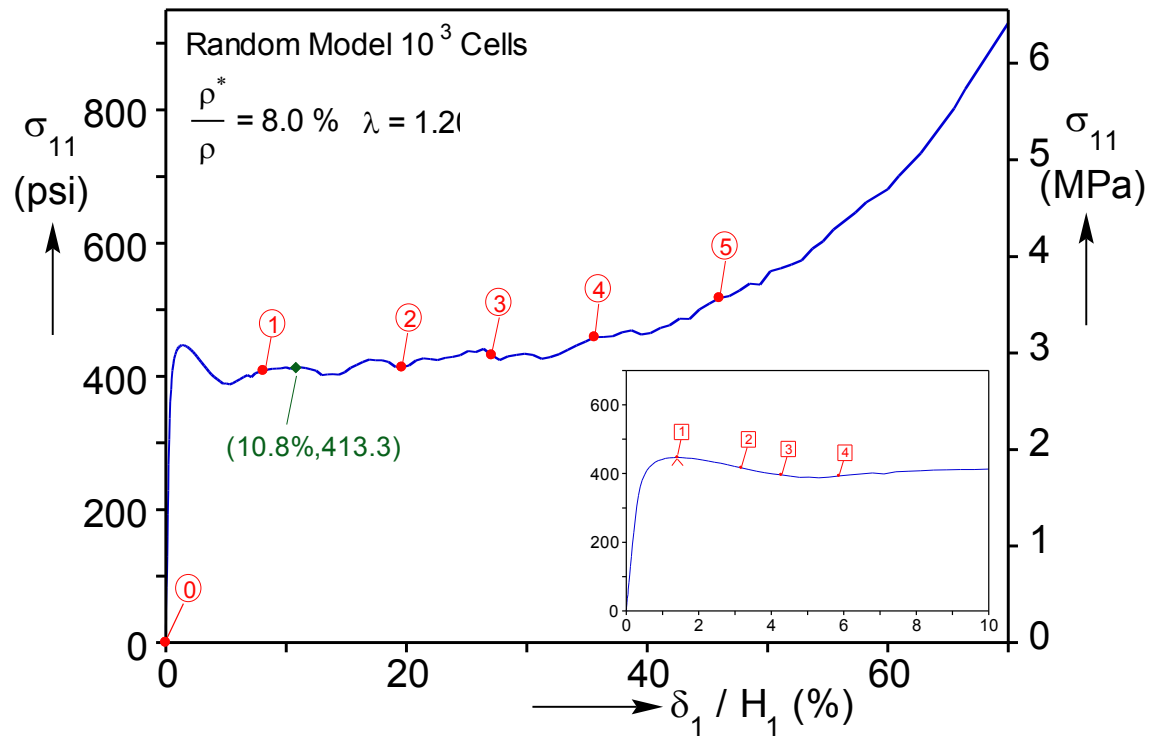


Fig. 3.6 Calculated compressive response in the rise direction of a model with 10^3 cells.

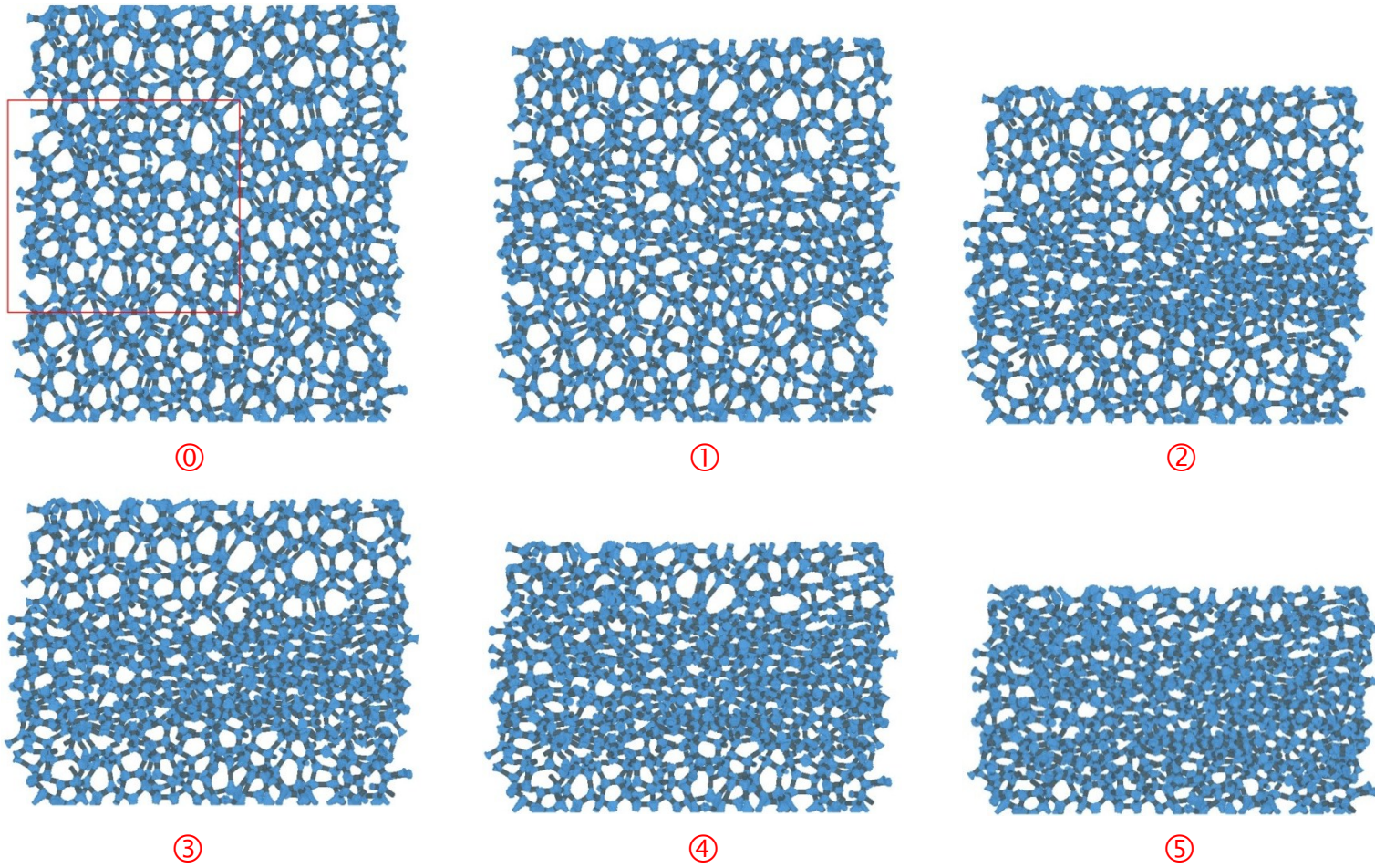


Fig. 3.7 Sequence of deformed configurations corresponding to points ① - ⑤ marked on the response shown in Fig. 3.6.

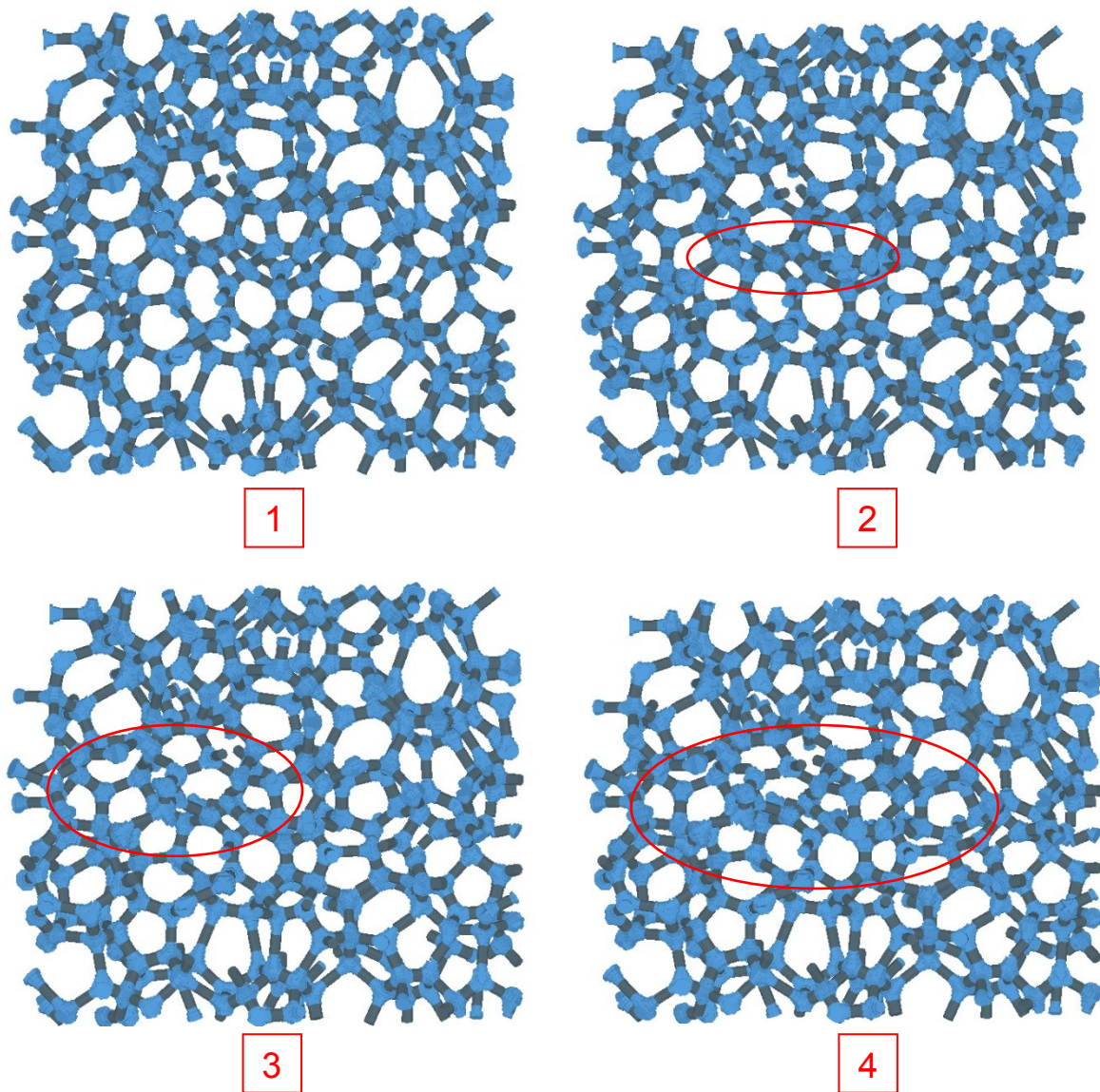


Fig. 3.8 Sequence of deformed configurations showing evolution of localized cell collapse corresponding to numbered bullets in the expanded response in the inset of Fig. 3.6 (expanded views of zone in red box in Fig. 3.7).

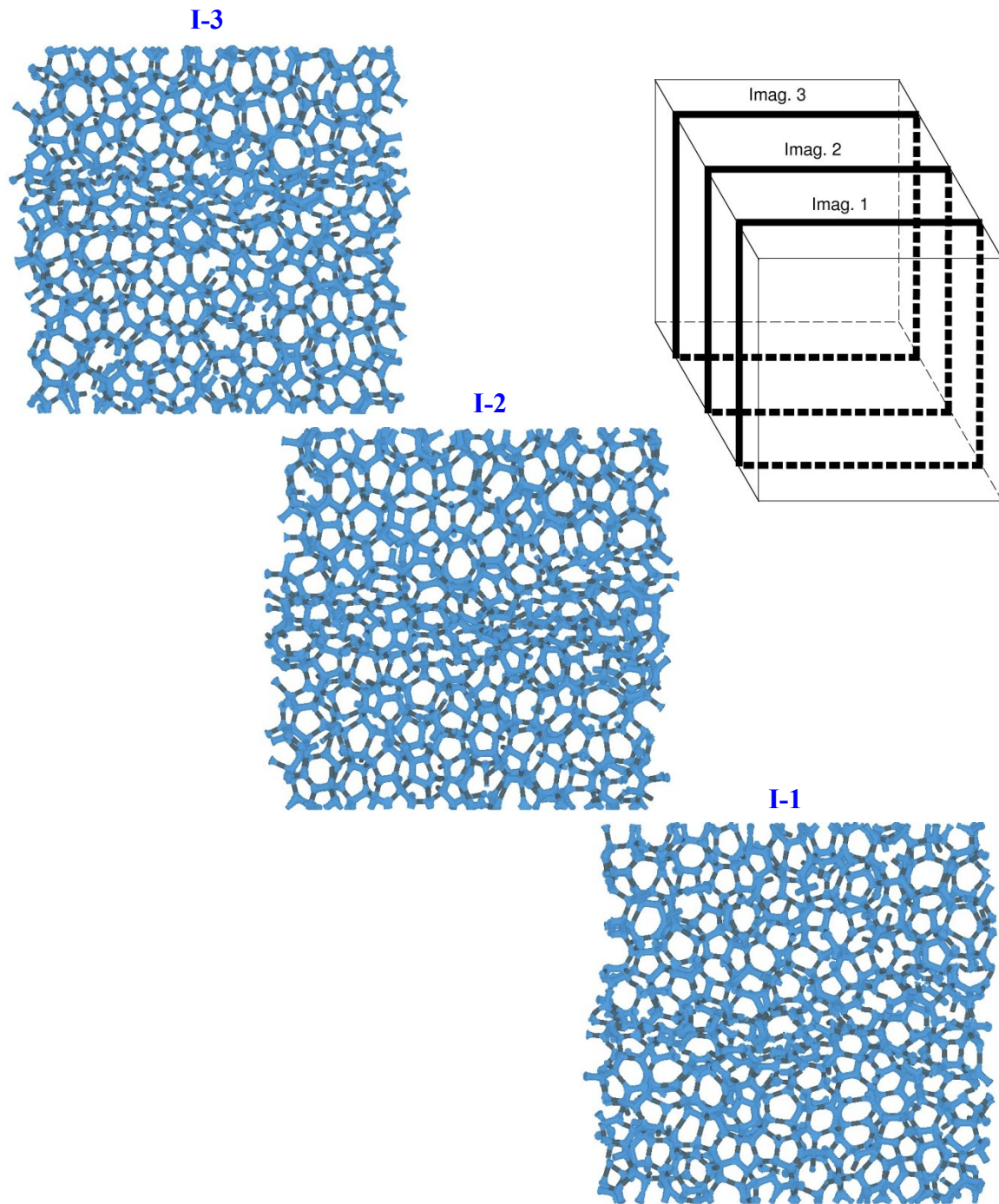


Fig. 3.9 Deformed configurations of model sections taken from the front, middle and back of the domain at $\delta_1/H_1 = 10.8\%$.

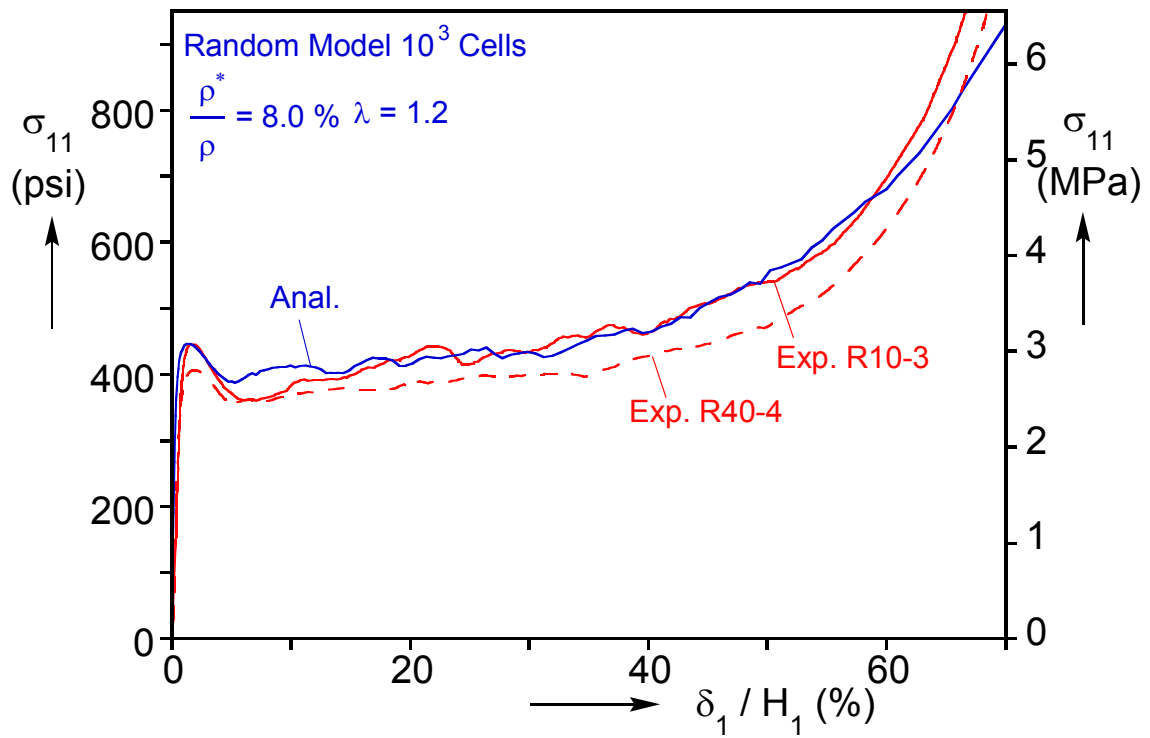


Fig. 3.10 Comparison of calculated and two experimental responses in rise direction.

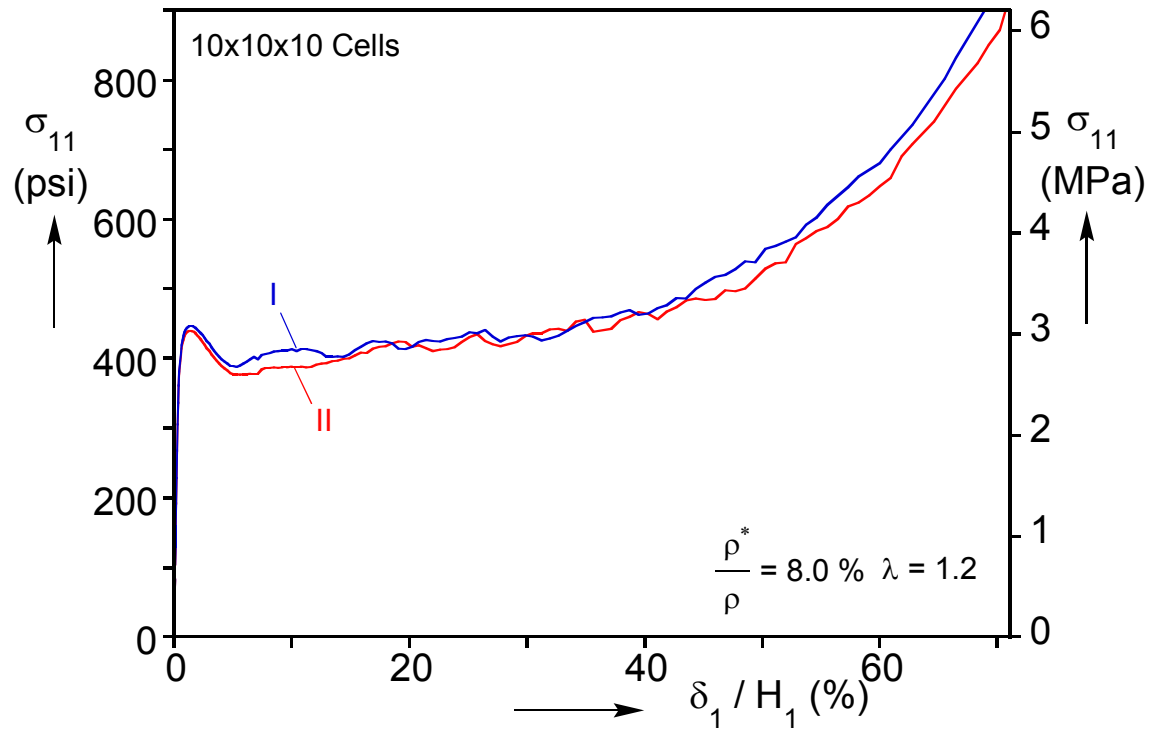


Fig. 3.11 Comparison of rise direction crushing responses from two random models of the same size.

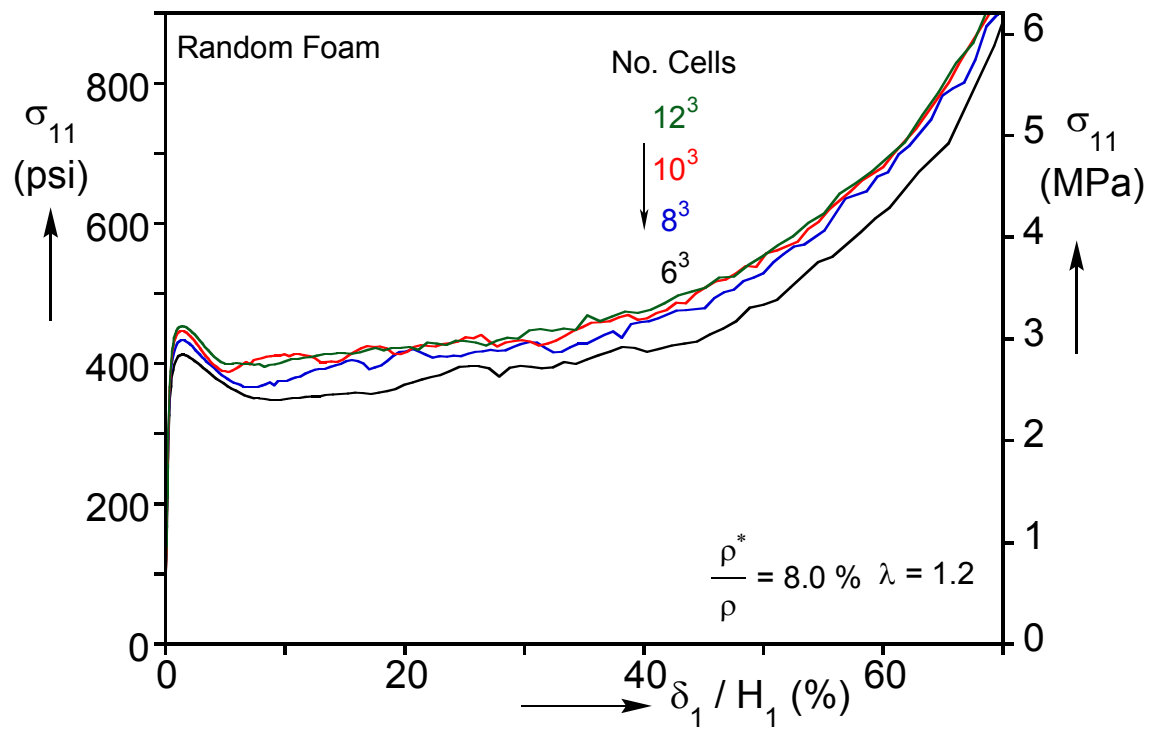


Fig. 3.12 Comparison of calculated responses from random foam models of different domain sizes.

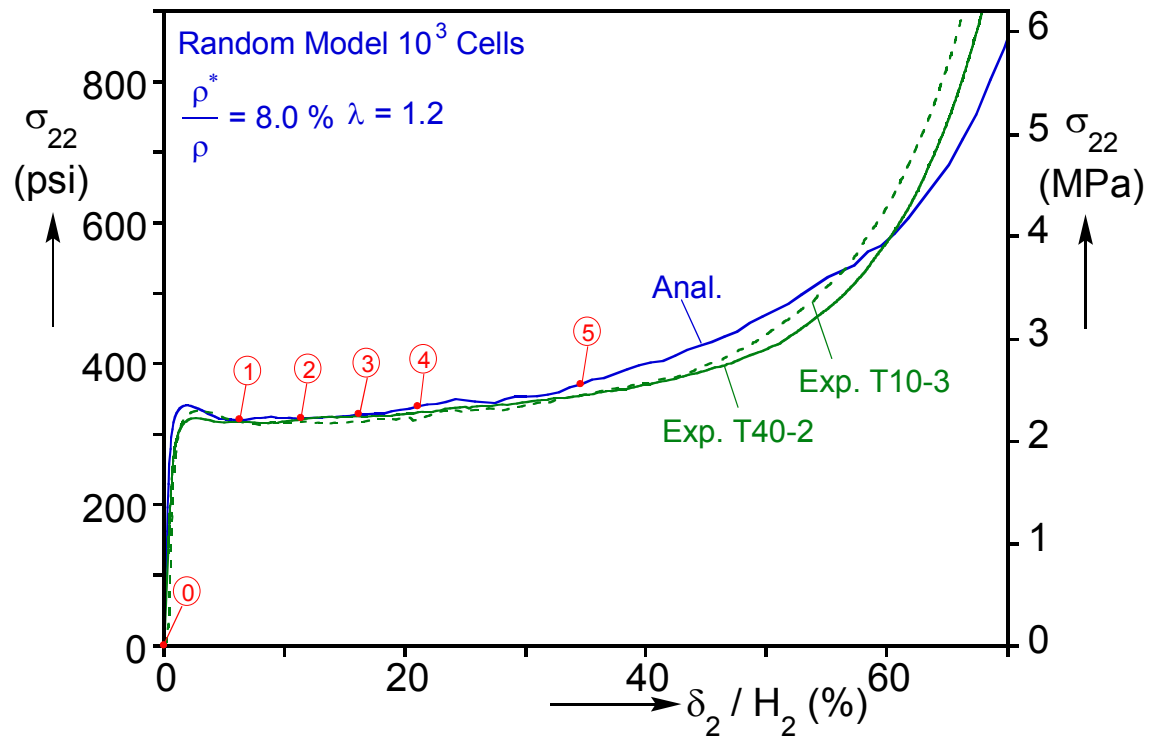


Fig. 3.13 Calculated compressive response in the transverse direction of a model with 10^3 cells and corresponding experimental responses.

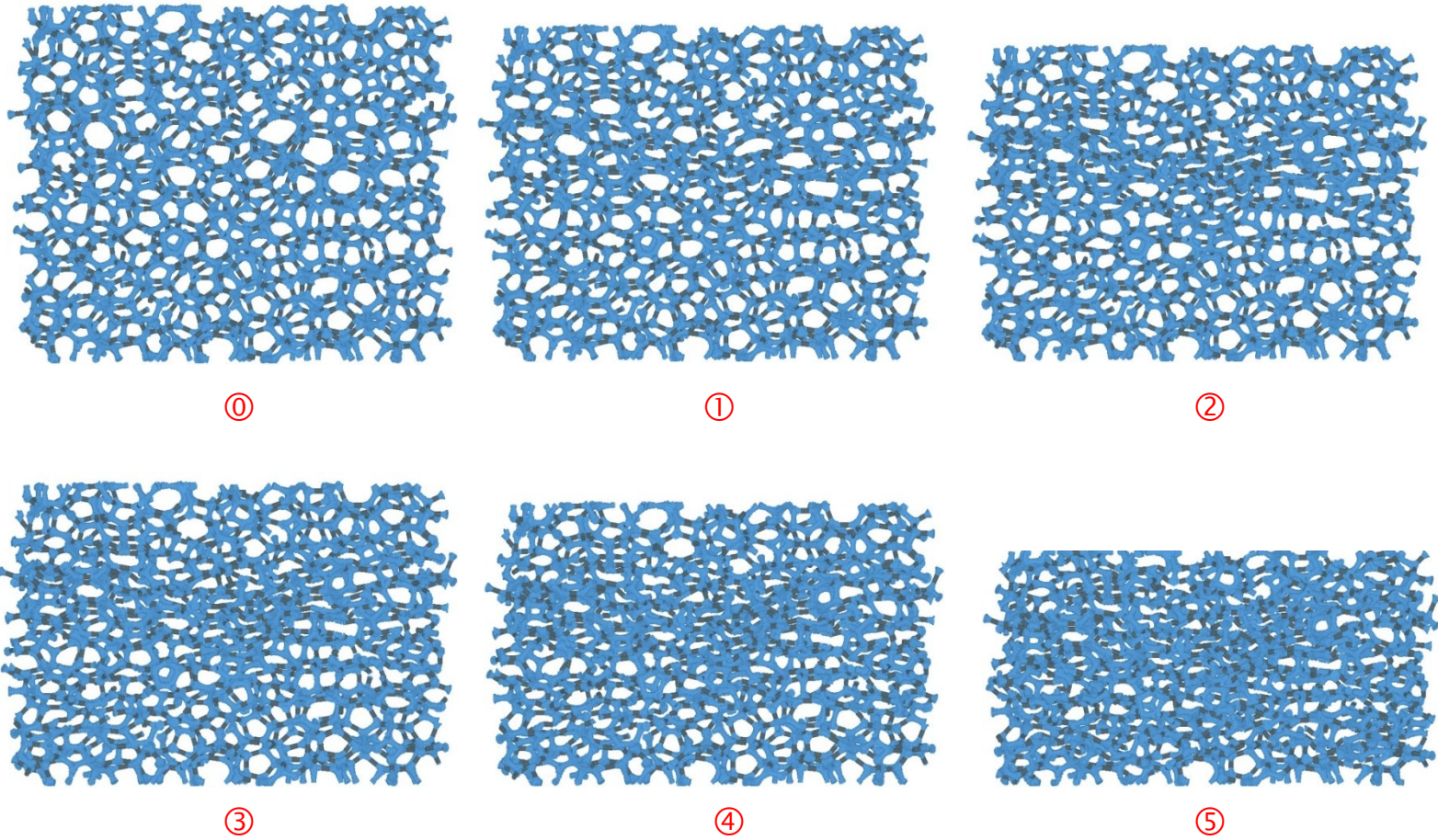


Fig. 3.14 Sequence of deformed configurations corresponding to points ① - ⑤ marked on the calculated response shown in Fig. 3.13.

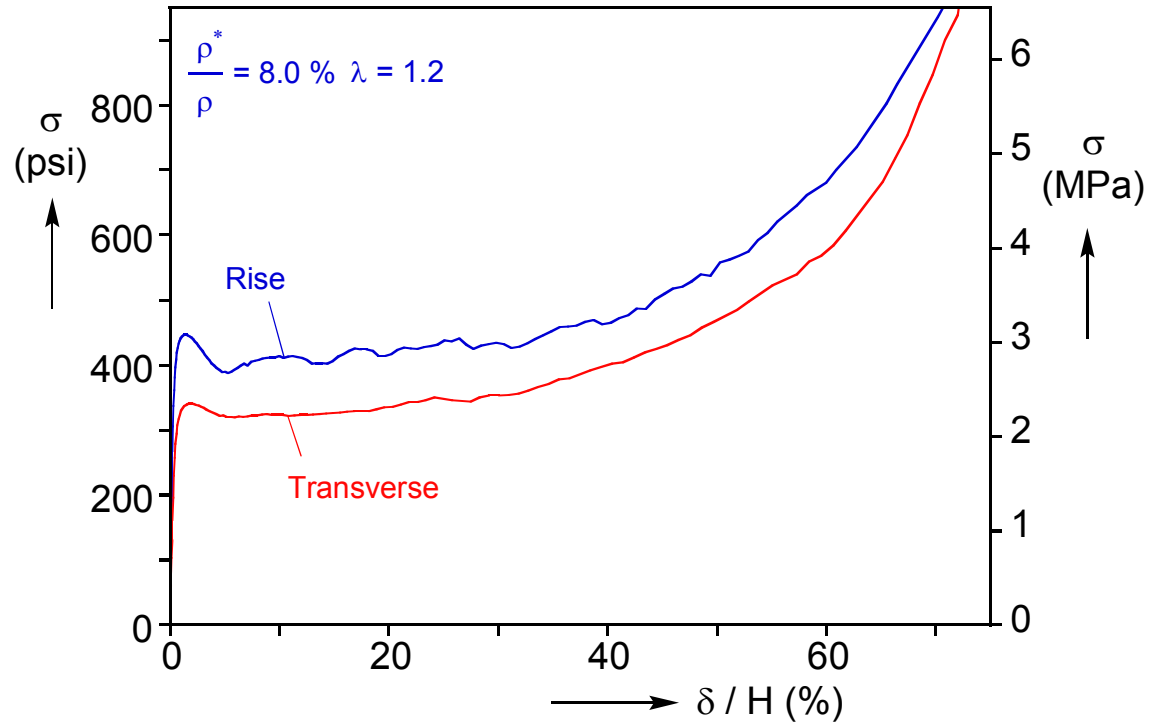


Fig. 3.15 Comparison of calculated crushing responses in the rise and transverse directions.

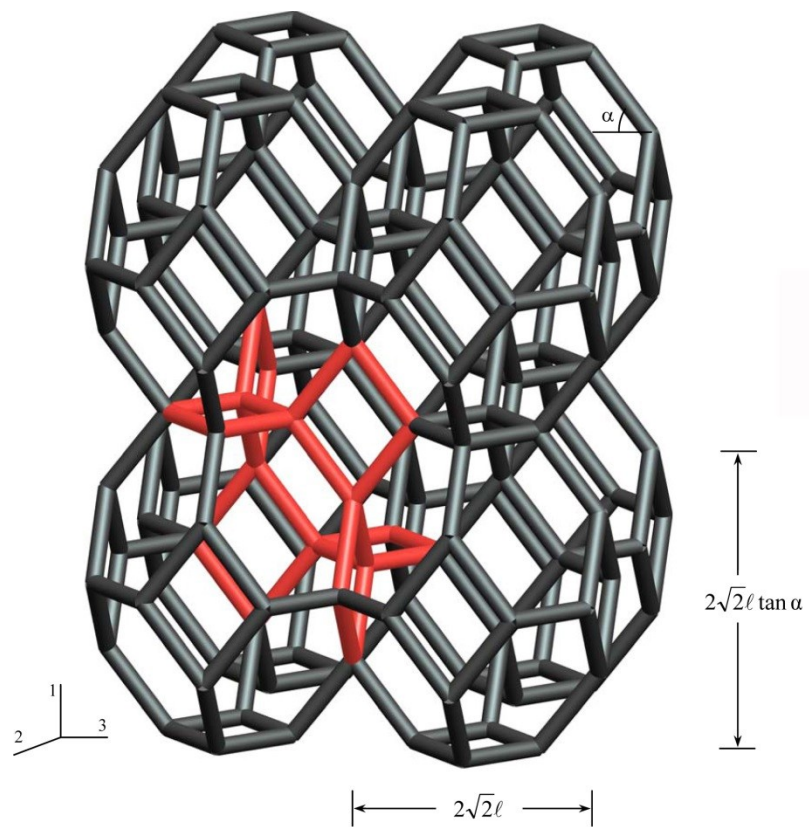


Fig. 3.16 Cluster of anisotropic Kelvin cells and characteristic cell (in red; from Jang and Kyriakides, 2009b).

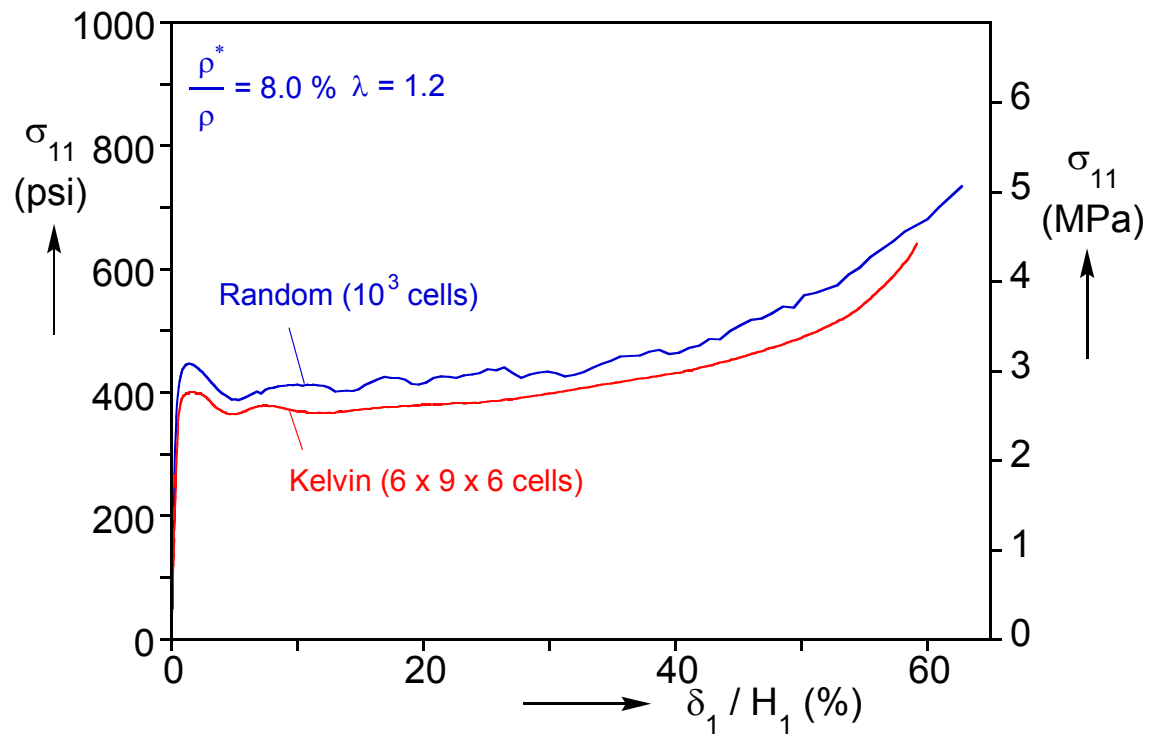
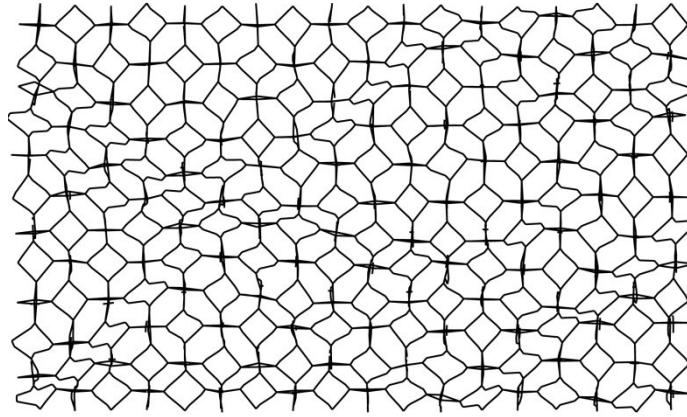
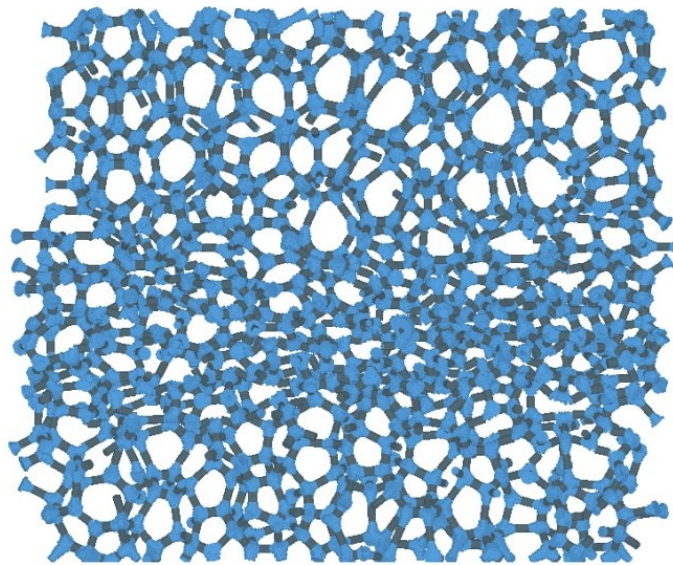


Fig. 3.17 Typical calculated compressive responses in the rise direction using Kelvin cell and random foam models.



(a)



(b)

Fig. 3.18 Typical deformed configurations showing bands of collapsed cells at a normalized shortening $\delta_1 / H_1 \approx 20\%$ for: (a) Kelvin cell model (6x9x6 cells) and (b) random model (10x10x10 cells).

Chapter 4: Review of Dynamic Crushing Experiments and Hugoniot

As mentioned in Chapter 1, it has long been established in shock physics that material systems with adiabatic compression modulus that increases with further compression such as that of foams (e.g., Fig. 3.1), under impact can be expected to develop shocks. Indeed, shocks in foams have been reported by several investigators as outlined in the Introduction. However, the quantitative analysis of experimental observations and results has involved one or more of the following assumptions: (i) that the quasi-static crushing response is a material response, and (ii) that the behavior in the densification regime is representative of the dynamic densification strain. Assumption (i) is clearly refuted by the fact that following the limit load deformation is localized (see Chapter 3 and references). Furthermore, assumption (ii) was recently examined in an experimental study performed by our group and found to be incorrect. This Chapter summarizes the major results of this experimental effort. The principal investigator of these experiments was Andrew Barnes and his results are reported in Barnes (2012). A more complete expose of this effort appears in Barnes *et al.* (2014).

4.1 Direct Impact and Shock Formation

4.1.1 Experimental Set-Up for Direct and Stationary Impact Experiments

Similar to previous studies, foam specimens were crushed dynamically by using a gas gun to fire a mass at a stationary specimen attached to a pressure bar or by accelerating the specimen and a backing mass and impacting the bar. We name the former as *stationary* and the latter *direct* impact tests. The experimental setup used is shown schematically in Fig. 4.1a and in a photograph in Fig. 4.1b. The gas gun has a 60 in (1500 mm) long stainless steel barrel with a 2.015 in (51.2 mm) bore (see Barnes (2012) for more details). The stress in the impacted specimen is monitored using a 96 in

(2440 mm) long pressure bar equipped with three strain gage stations as shown in Fig. 4.1a (SG1-3). To increase the strain measurement sensitivity, the bar diameter was kept at 0.507 in (12.9 mm) which dictated the installation of a 2.49 in (63.2 mm) diameter anvil at the receiving end of the bar as shown in the same figure. This mismatch of impedance implies that the short time response cannot be extracted accurately unless the details of the wave propagation through the anvil-bar interface are modeled completely either analytically or numerically (e.g., see Tan *et al.*, 2005a); such extractions will not be attempted here. The stress in the foam specimen is calculated from

$$\sigma = \left(\frac{A_{bar}}{A_{spec}} \right) E_{bar} \varepsilon_{bar}. \quad (4.1)$$

The deformation of the specimen was monitored using a high-speed digital camera, usually run at 40,000 frames/s at a resolution of 512×256 pixels. The recorded images and the strain gage signals were synchronized by selecting a relevant event as time zero.

4.1.2 Results from a Direct Impact Experiment that Develops Shocks

We use results from a direct impact experiment to illustrate the basic physics of shock formation and propagation in foams. In this case the specimen was accelerated along with a polycarbonate backing mass of 181g to an impact velocity of $V_i = 90$ m/s. The backing mass was chosen so that the kinetic energy of the mass-foam system is about two times the quasi-static crushing energy. The specimen had an initial height of 4.03 in (102 mm) and a relative density $\rho^* / \rho = 8.4\%$. Figure 4.2 shows the recorded stress-time history and Fig. 4.3 a set of images from the high-speed video record that correspond to the numbered bullets on the response (the stationary anvil is on the left and the traveling backing mass is coming in from the right). Image © was taken at $t = 0.025$

ms, image ② at 0.25 ms, image ④ at 0.5 ms and image ⑦ at 0.875 ms. As noted above, the impedance mismatch at the anvil/bar interface tends to smooth out features that have a short rise time. In particular, the signal for $t < 0.3$ ms is distorted and, consequently, rather than an expected initial sharp rise in stress, the recorded signal rises gradually until the time corresponding to image ②. From $t \approx 0.3$ ms to 0.925 ms the stress on the anvil remains relatively constant.

In image ① in Fig. 4.3 the foam has already established contact with the anvil crushing a narrow band of material. In image ② a sharply defined crush front can be seen at the foam-anvil interface. Looking at images ④ and ⑦ the front has clearly propagated towards the incoming backing mass remaining nearly planar. Behind the front, the foam appears significantly crushed and densified while ahead of it the material appears essentially undeformed. It is interesting to observe that the width of the crushed section has increased slightly. At 0.925 ms the front reaches the backing mass and the recorded stress takes an upturn, at the time defined as t_2 . Subsequently, the already crushed foam undergoes further compaction.

Using a slice out of the center of each image of the deforming specimen in the video record, the position-time ($x-t$) diagram shown in Fig. 4.4 is assembled (images are separated by 25 μ s time intervals). On the left is the nearly stationary anvil and on the right is the traveling foam and backing mass (the latter does not come into the field of view immediately). Between times t_0 and t_1 the foam and backing mass are traveling at 90 m/s. The foam front traces a linear trajectory with a slope corresponding to this velocity. The foam-backing mass system strikes the anvil at t_1 and crushing begins at the foam-anvil interface. The crushing front propagates towards the backing mass while the backing mass continues to travel towards the anvil. The position of the crushing front is represented by the locus of points in yellow. This locus of points is slightly curved

indicating some decrease in velocity. The velocity of the backing mass, which is the same as the particle velocity of the intact foam (ahead of the front), is represented by the slope of the locus of points formed by the foam-backing mass interface; it is somewhat curved indicating again a gradual reduction in its velocity. At time t_2 the crush front reaches the backing mass and subsequently the crushed foam undergoes additional compaction. From time t_1 forward the anvil experiences a small motion that is reflected by the slightly curved trajectory of its front edge.

Clearly, the two regimes of deformation separated by a traveling sharp front are pointing to shock dynamics. Figure 4.5a shows schematically a shock propagating in a foam specimen in a direct impact test, such as the one described above, as well as the associated problem variables. The foam specimen has an initial length h_o ; in the partially crushed configuration shown the crushed and intact sections have corresponding lengths h_c and h_i . The velocities of the backing mass (V_b), the crush front (V_c), and of the shock (\dot{s}) are evaluated from the complete video record. The images are separated by 25 μ s so a three-point centered moving average is used to extract these velocities as follows:

$$V_b = \frac{\Delta x_b}{\Delta t}, \quad V_c = \frac{\Delta x_c}{\Delta t}, \quad \dot{s} = -\frac{\Delta h_i}{\Delta t}, \quad (4.2)$$

where $x_c = h_c$, and s is the undeformed length of the crushed section given by $s = h_o - h_i$. Figure 4.5b shows schematically the propagation of a shock in a stationary impact test and the relevant problem parameters. In this case the shock starts on the LHS at the projectile-foam interface and propagates towards the stationary anvil. We note that in cases where the anvil moves, usually slightly, the velocity measures in Eq. (4.2) were corrected to include this motion.

Figure 4.6 shows the absolute values of the three velocities vs. time extracted from the images of the specimen impacted at a velocity of 90 m/s. The fluctuations in the plots, especially for \dot{s} and V_c , are due to the discrete nature of the measurements and due to the difficulty in accurately identifying the position of the shock front—assumed to be a sharp planar discontinuity but in reality has a finite thickness and a wavy profile. Once again t_2 , marked with a dashed line, corresponds to the time when the shock reaches the anvil. The backing mass velocity, whose trajectory is smoother than the other two, is seen to gradually decrease from 90 m/s to approximately 64 m/s at t_2 . Beyond this time the backing mass decelerated rapidly. The shock front velocity is higher than that of the backing mass and of opposite sign (see Fig. 4.5a). Despite the noise in the data a gradual decrease can be clearly seen. The crush front velocity is the lowest and although again noisy appears to remain relatively unchanged.

The direct measurement of the stress on the anvil, the shock velocity, and the particle velocities behind and ahead of the shock are sufficient to completely characterize the dynamic crushing of the foam using the shock conservation laws without invoking any constitutive model for the material.

4.2 Construction of the Hugoniot

4.2.1 Shock Equations

The classical jump conditions in Lagrangian form representing conservation of mass, momentum, and energy applied to plane longitudinal shocks can be expressed as follows (Davison, 2008):

$$\rho_0 \dot{s} [[\rho^{-1}]] + [[V]] = 0, \quad (4.3a)$$

$$\rho_0 \dot{s} \llbracket V \rrbracket + \llbracket \sigma \rrbracket = 0, \quad (4.3b)$$

and
$$\rho_0 \dot{s} \llbracket U + \frac{1}{2} V^2 \rrbracket + \llbracket \sigma V \rrbracket = 0. \quad (4.3c)$$

Here, $\llbracket g \rrbracket = g^+ - g^-$ is the jump operator with g^+ representing the value of a variable ahead of a discontinuity and g^- the value behind it; s is the position of the discontinuity in the undeformed configuration and \dot{s} its Lagrangian velocity. The variables $\{\rho, V, \sigma, U\}$ are respectively the mass density, particle velocity, nominal stress, and strain energy density. Given an initial state $\{\rho, V, \sigma, U\}^+$ the unknown quantities $\{\rho, V, \sigma, U\}^-$ and \dot{s} can be determined from Eqs. (4.3). Typically, the particle velocity or stress behind the shock is imposed. Determination of the remaining variables requires one more measurement, such as that of the shock speed. Thus, the shock state can be established by conducting experiments at different speeds and developing the $V - \dot{s}$ Hugoniot, where V is the particle velocity behind the shock. In the experimental setups shown schematically in Fig. 4.5, one of the velocities is imposed and one of the stresses is measured: (V^+, σ^-) for direct impact tests and (V^-, σ^+) for stationary impact. The measurements were used to develop a relationship between the imposed velocity and the shock speed, i.e., the $V_b - \dot{s}$ Hugoniot (V_b is approximately equal to V^- for stationary impact tests and V^+ for direct impact tests).

Referring again to Fig. 4.5, assuming that the transverse strain is small and can be neglected, the inverse of the density jump $\llbracket \rho^{-1} \rrbracket$ can be expressed as:

$$\left(\frac{1}{\rho^+} - \frac{1}{\rho^-} \right) = \left(\frac{1}{\rho_o} - \frac{h_c}{\rho_o s} \right) = \frac{1}{\rho_o} \left(\frac{s - h_c}{s} \right) = \frac{\varepsilon_H}{\rho_o} \quad (4.4)$$

where ρ_o is the initial density of the material assumed to remain unchanged ahead of the shock and ε_H is the strain behind the shock that we will refer to as the *Hugoniot strain*. Thus, the conservation of mass Eq. (4.3a) can be written as:

$$\dot{s}\varepsilon_H = (V^+ - V^-). \quad (4.5)$$

In addition, (4.3b) and (4.3c) can be written as:

$$\sigma^+ = \sigma^- - \rho_o \dot{s} (V^+ - V^-) = \sigma^- - \rho_o \frac{(V^+ - V^-)^2}{\varepsilon_H}, \quad (4.6)$$

$$\rho_o (U^+ - U^-) = \frac{1}{2} (\sigma^+ + \sigma^-) \varepsilon_H. \quad (4.7)$$

4.2.2 Hugoniot

A series of direct and stationary impact experiments similar to the one described in Section 4.1.2 were conducted covering initial impact velocities of $20 \leq V_i \leq 158$ m/s. Clear shock behavior was observed for impact velocities starting at 60 m/s and higher. In all cases the velocities of the backing mass and shock were evaluated directly from the high-speed video records and were used to generate the $V_b - \dot{s}$ Hugoniot of this foam. As was the case for the results for $V_i = 90$ m/s in Fig. 4.6, the backing mass velocity decreased gradually to some extent as the crush front traversed the specimen. Thus, for each experiment we will report velocities extracted using a three-point centered moving average from the first appearance of the shock until the time it has propagated across the whole length of the specimen. Figure 4.7 shows the $V_b - \dot{s}$ Hugoniot generated using sets of measurements from four direct and two stationary impact tests. Despite some scatter the results exhibit a linear trend. A least squares linear fit of the data

$$\dot{s} = A + BV_b \quad (4.8)$$

yields $A = 35.55$ m/s and $B = 0.9797$ ($R^2 = 0.83$) and is included in the same figure. Although not necessarily expected, the resulting $V - \dot{s}$ linear relationship follows similar trends of Hugoniot developed for many solids (e.g., Marsh, 1980) and some porous materials (e.g., Morris, 1991; Maines *et al.*, 2010; Zaretsky *et al.*, 2012), albeit usually at much higher impact speeds. The constant A is usually considered to correspond to the bulk wave speed of the solid (e.g., Davison, 2008). In foams like the ones analyzed here, this limit is not recovered because the material deforms inhomogeneously even when the impact speed is too low for shock formation (see §4.3 and §5.4).

A second representation of the Hugoniot relating the Hugoniot strain to the backing mass velocity, $V_b - \varepsilon_H$, can also be generated directly from the video images by measuring ε_H as defined in Eq. (4.4). The result is seen in Fig. 4.8 where ε_H is seen to exhibit a strong nonlinear dependence on V_b . An analytical formula for the $V_b - \varepsilon_H$ relationship can be obtained by combining Eq. (4.5) with the linear fit (4.8) of the $V_b - \dot{s}$ Hugoniot, which then yields:

$$\varepsilon_H = \frac{V_b}{A + BV_b} \quad (4.9)$$

This relationship, drawn with a dashed line in Fig. 4.8, is seen to fit the data quite well, which provides confidence in the measurements of \dot{s} and ε_H . At higher velocities, the Hugoniot strain approaches asymptotically the full densification value of about 0.92 for this material. However, this bounding strain level is somewhat artificial as, among other reasons, the lateral strain of the compacted foam is not zero as assumed; in fact it tends to increase with impact velocity.

Included in Fig. 4.8 for comparison is the strain at the completion of the inhomogeneous crushing phase measured in quasi-static experiments (designated as ε_{Do} and depicted by \blacktriangle symbols) and in two dynamic experiments (\blacksquare) that did not develop shocks. The quasi-static value has been estimated to be approximately 0.55 and the other two values at 0.56 and 0.59 (all estimated at the termination of crushing). Thus collectively, the results in Fig. 4.8 demonstrate that the densification strain increases significantly with velocity, a result that refutes the adoption of r-p-p-l approximation of the quasi-static crushing response.

The stress-impact velocity Hugoniot can be generated from the measurements and the conservation of momentum (Eq. 4.6). Figure 4.9 shows first the measured stresses vs. V_b (i.e., σ^- for direct impact and σ^+ for stationary impact). For each set, the stresses on the opposite side of the shock are evaluated using Eq. (4.6) and the measured stress and velocities (e.g., σ^- , $V^+ = V_b$ and \dot{s} for direct impact). Because of the initial rise time, the stress measurements used are in the interval $0.3 \leq t \leq t_2$ ms, where the upper limit represents the time needed for the shock to traverse the whole specimen. The stress behind the shock is seen to increase significantly with velocity while the stress ahead of the shock remains relatively unchanged.

Included in Fig. 4.9 are values of the *initiation stress*, σ_I (marked with \blacktriangle), recorded from four quasi-static crushing experiments (σ_I is the first local stress maximum). It is interesting to observe that the two sets of directly measured values of σ^+ , as well as the four sets evaluated from Eq. (4.6), fall approximately at the same level as σ_I . Prompted by this trend, we assign σ^+ the value σ_I , which together with the linear fit of \dot{s} in (4.6) results in the following expression for σ^- :

$$\sigma^- = \sigma_I + \rho_o V_b (A + B V_b). \quad (4.10)$$

Also included in Fig. 4.9 with dashed lines is the constant value of $\sigma^+ = \sigma_I = 360$ psi (2.48 MPa) as well as the quadratic dependence of σ^- on V_b based on (4.10). Both curves are in very good agreement with the experimental data.

Another interpretation of the results is obtained by considering the relationship between the stress and strain behind the shock, or the $\varepsilon_H - \sigma^-$ Hugoniot. Figure 4.10 shows results from the six shock experiments performed. Using (4.9) to eliminate V_b from (4.10) leads to:

$$\sigma^- = \sigma^+ + \rho_o \varepsilon_H \left(\frac{A}{1 - B \varepsilon_H} \right)^2. \quad (4.11)$$

This expression is also plotted in the figure with a dashed black line. It is seen to follow the trajectory of the data, overestimating the highest velocity data to some degree. This is related to the small deviation between Eq. (4.8) and the corresponding data in Fig. 4.8.

The energy expended across the shock can be evaluated from Eq. (4.7) using the stresses σ^- and σ^+ (one is measured and one is calculated from 4.6) and ε_H . In addition, the foam ahead of the shock is assumed to be undeformed i.e., $\varepsilon^+ = 0$. Figure 4.11 shows the energy per unit volume-velocity ($U_o - V_b$) representation of the Hugoniot, once again using the data measured in the time interval $0.3 \leq t \leq t_2$. The results show that the energy also increases significantly with impact speed. Included in the figure with a dashed line is the estimated relationship using (4.5), (4.6) and (4.8) in Eq. (4.7) to obtain:

$$U_o = \rho_o U^- = \frac{\sigma^+ V^-}{A + B V^-} + \frac{1}{2} \rho_o (V^-)^2. \quad (4.12)$$

This expression follows the experimental data quite well.

For comparison purposes Fig. 4.11 includes the energies under the stress-displacement responses up to the onset of densification, $U_o(\varepsilon_{Do})$, from the two lower velocity experiments that did not develop shocks as well as the corresponding values from three quasi-static crushing experiments (\blacktriangle). Although this comparison is not quite appropriate it shows qualitatively the difference between non-shock and shock behavior.

4.2.3 Effect of specimen density and anisotropy

At this stage it is worth pointing out that the cylindrical specimens used in this study, although originating from the same block of foam as the ones in Jang and Kyriakides (2009a), exhibit some variation in density as well as in anisotropy. Such variations contribute to the observed scatter in the results. As reported, this variation in properties has a corresponding influence on quasi-static crushing responses. Figure 4.12 shows four quasi-static nominal stress-displacement crushing responses. Responses R10-3 and R10-4 are taken from Jang and Kyriakides (2009) while responses QS2 and QS3 were measured from two specimens that originated from the same neighborhood in the foam block as the ones used in the impact experiments of Barnes (2012). Although the responses follow similar trajectories and appear to all densify at about 55% of average compressive strain, their stress trajectories vary to some degree with Exp. R10-3 having the highest and QS2 the lowest one. Consequently, the *initiation* (σ_I) and *plateau* or *propagation stress* ($\bar{\sigma}_P$) as well as the energy absorbed ($U_o(\varepsilon_{Do})$) at the onset of densification exhibit corresponding variations. These differences are partly due to variations in the average density and anisotropy of each specimen. Thus, for example, the X-ray tomography image in Fig. 2.1 (extracted from specimen QS3) shows the major diameter of the elongated cells to be somewhat off the vertical, which is the crushing

direction. The limit load values σ_I from these two experiments appear closer to the values of σ^+ measured in the impact experiments, prompting the adoption σ_I from QS2 in Fig. 4.9 and Eqs. (4.10) - (4.12).

4.3 Impact at Subcritical Velocities

A select number of impact experiments were conducted in the same study at velocities low enough to explore the non-shock dynamic behavior of foams. Figure 4.13 shows the nominal stress-time history recorded in experiment DY13 in which the foam specimen was accelerated with a backing mass of 1561 g and impacted the anvil at a speed of 35.1 m/s. In this case the recorded stress is also plotted against the net shortening of the specimen δ , normalized by its initial length h_o , in Fig. 4.14. Included in the same figure for comparison is the corresponding response from one of the quasi-static experiments performed on a specimen of the same geometry (QS3).

As in the previous results, the recorded stress does not exhibit the initial sharp rise seen in the quasi-static response because of the mismatch at the anvil/bar interface. This mismatch distorts the stress up to $t \approx 0.3$ ms. Beyond this time, the stress is seen to remain nearly constant until the whole specimen is crushed. Interestingly, the stress plateau is seen in Fig. 4.14 to be at about the same level as in the quasi-static response.

Figure 4.15 shows a select set of images from the ones of the photographic record which correspond to the numbered bullets on the stress history in Figs. 4.13 and 4.14. At first impact with the anvil, a narrow zone of the material comes into contact with it and deforms. Collapse then initiates further away from the anvil, presumably due to crushing of local weaker cells, designated as site A. The deformation in site A spreads while simultaneously localized deformation initiates at a new site close to the mid-length of the undeformed specimen, designated as site B. Image ② in Fig. 4.15 at 0.475 ms shows the

growth of local deformation at both sites A and B. The neighborhood of zone B has also developed some out of plane deformation in the form of bending. As crushing continues, the section between zone A and B is significantly compacted, and at approximately $t = 1.175$ ms a third zone of collapse, designated as C, has developed closer to the backing mass (see image ⑥). Subsequently, localized deformation becomes increasingly less pronounced and harder to discern as deformation becomes more uniform (e.g., image ⑨ at 1.55 ms). Concurrently, the stress in Fig. 4.13 is starting to rise.

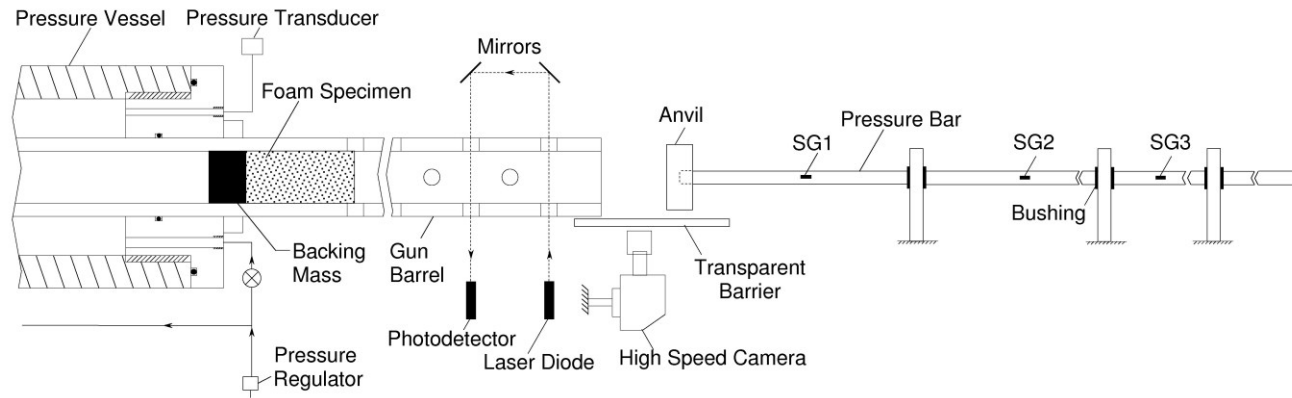
Figure 4.16 shows the velocity of the backing mass vs. time, which is seen to remain relatively unchanged for about the first two milliseconds. By about 1.5 ms, a significant amount of the kinetic energy has been consumed and the backing mass is starting to decelerate. Furthermore, after this time the anvil-pressure bar system is also starting to move.

In summary, at impact velocity of 35.1 m/s the specimen starts to deform at the anvil, but subsequently deformation localizes at other sites along the length, presumably where the material is somewhat weaker. Although we are limited to surface observations, the localization bands do not have any preferred directions but instead meander across the specimen where weaker sites may exist. The local bands broaden and multiply with time while the recorded stress remains relatively unchanged. This behavior is definitely reminiscent of that observed in quasi-static experiments where the development and spreading of localized buckling and crushing inside the specimen was monitored using X-ray tomography (see Chapter 3 and references).

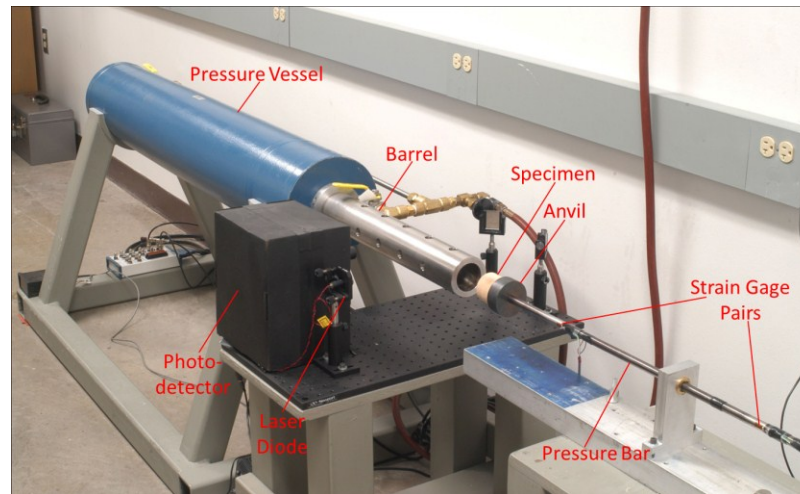
Experiment DY9 in which the specimen was impacted at 39 m/s exhibited the same general behavior. At these two impact velocities the stress recorded at the anvil remained nearly constant until most of the specimen was crushed and their average values were 381 psi for DY13 and 416 psi for DY9 (plotted in Fig. 4.9 with ■). In other

words, stress levels that are similar to quasi-static crushing initiation and plateau stresses. If there is a dynamic enhancement of the stress level, as reported by others, it is rather small and difficult to discern due to the noted scatter between specimens introduced by small variations in density and anisotropy. The main effect of inertia appears to be an increase in the densification strain induced during the stress plateau as seen in Fig. 4.14.

As mentioned earlier, the results in Fig. 4.8 clearly refute the r-p-p-l assumption. In the way of improving on the strictness of this assumption, some investigators adopted an estimate of ε_H based on the rising part of quasi-static responses like the ones in Fig. 4.12. To evaluate the validity of this assumption, included in the $\varepsilon_H - \sigma^-$ Hugoniot shown in Fig. 4.10 with dashed lines are: (i) the compressive stress-shortening response from one of the quasi-static experiments beyond the onset of densification ($\delta/h_o \geq 0.55$) and (ii) the rising branch of the stress-shortening response recorded in the experiment with $V_i = 35.1$ m/s (DY13, $\delta/h_o \geq 0.60$). Comparing the quasi-static and dynamic results, it is clear that the shock-induced strain is significantly higher than that induced quasi-statically at the same stress. The low velocity dynamic response is approximately parallel to the quasi-static one but is also to the left of the $\varepsilon_H - \sigma^-$ data that follow a less steep trajectory. The results clearly indicate that: (a) the Hugoniot strain is strongly dependent to impact velocity and (b) the shock-induced strain is significantly larger than values induced quasi-statically at the same stress. Consequently, quasi-static crushing responses cannot be used to calculate the Hugoniot.



(a)



(b)

Fig. 4.1 Experimental set up used to perform the impact tests. (a) Schematic and (b) photograph.

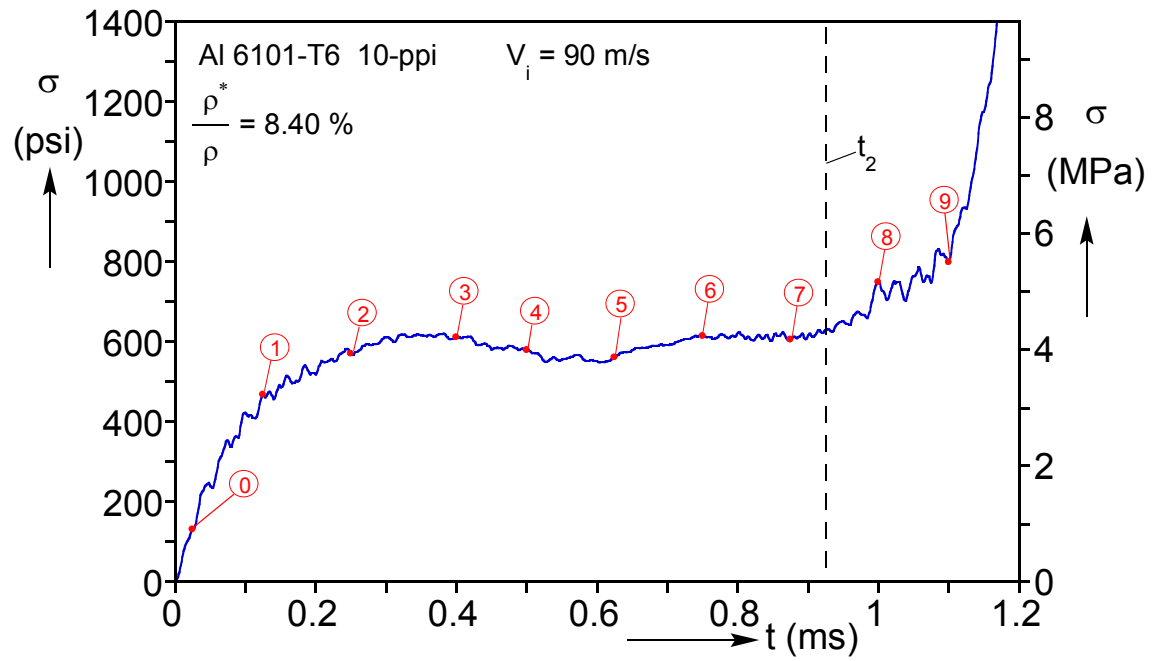


Fig. 4.2 Proximal stress-time history from a direct impact test on a foam specimen with initial impact speed of 90 m/s.

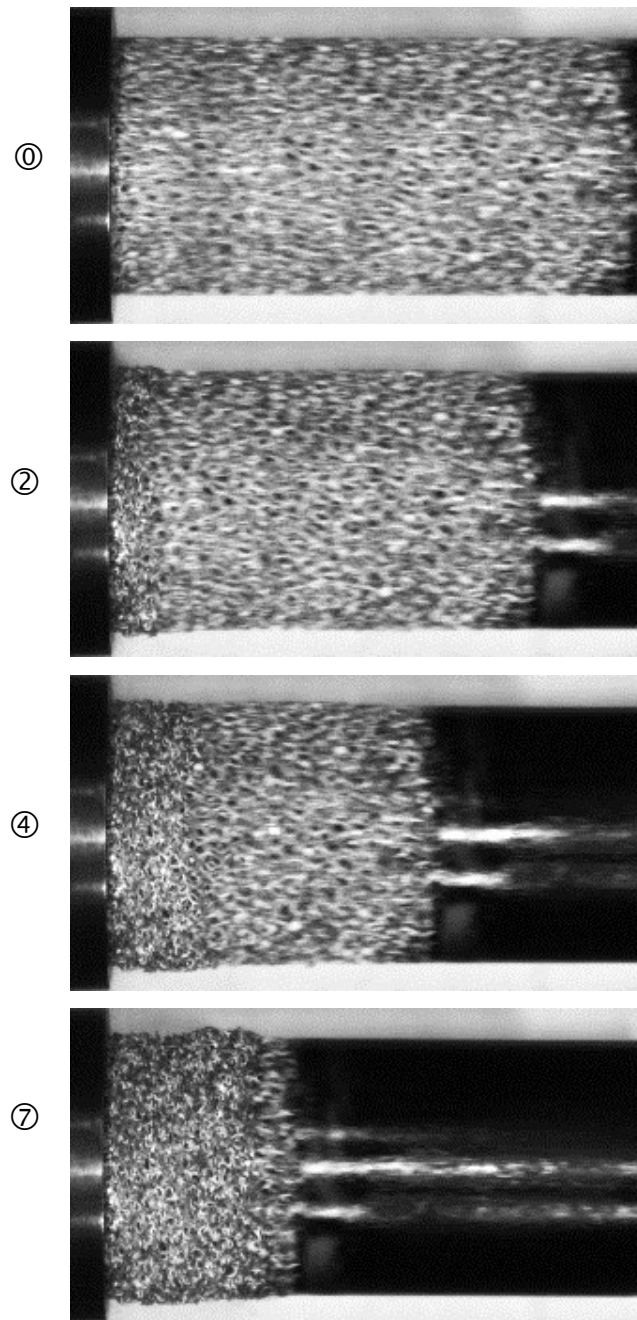


Fig. 4.3 Sequence of images from the high-speed video recording corresponding to times marked on the stress history with numbered bullets.

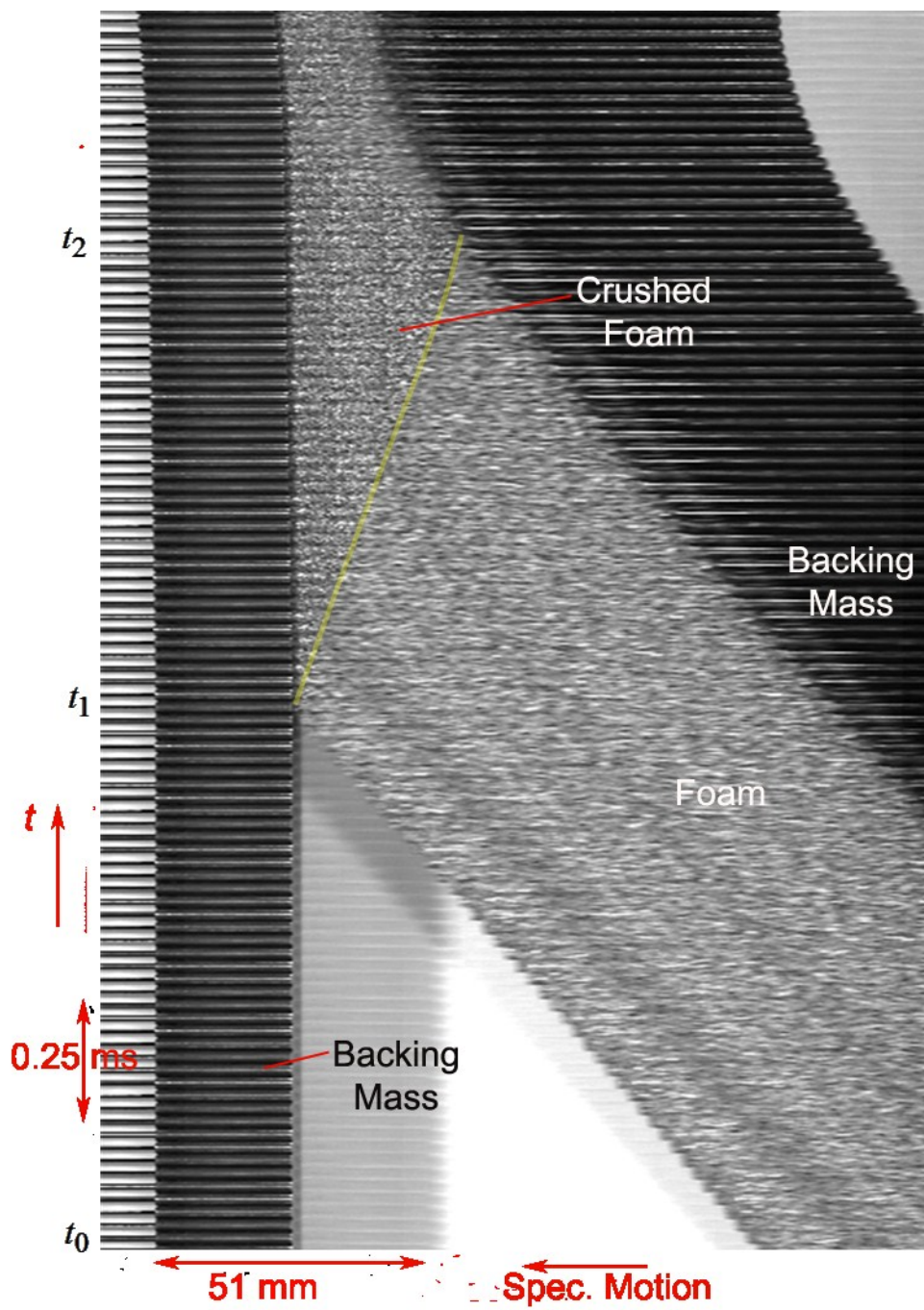
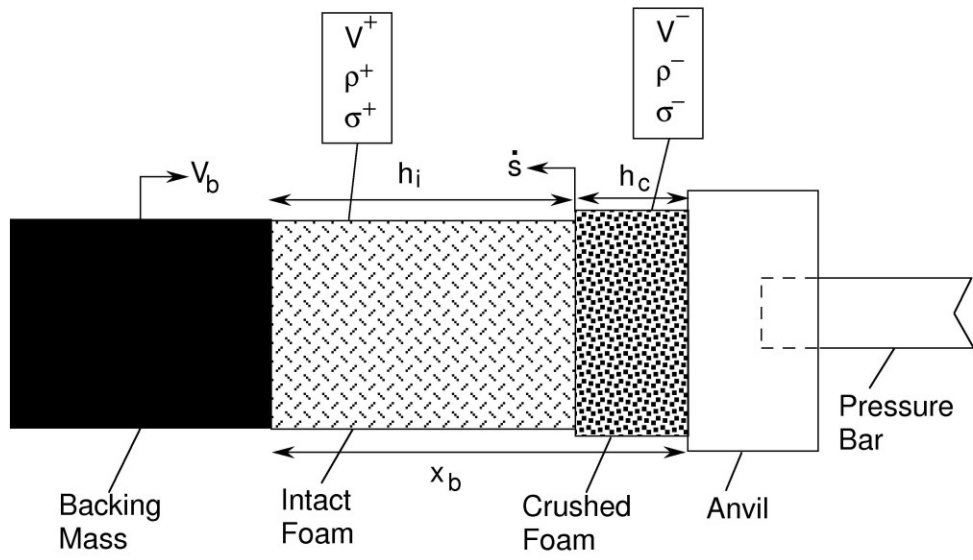
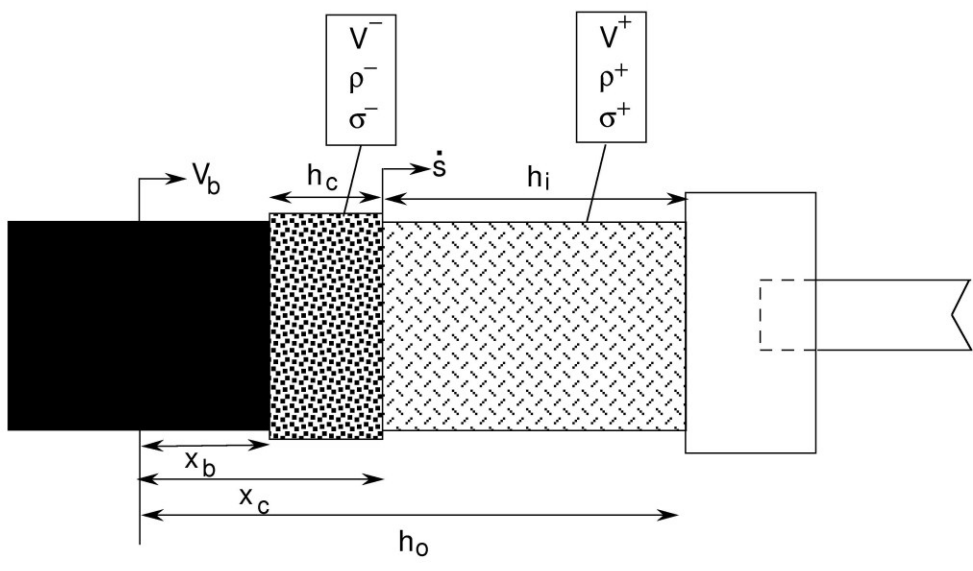


Fig. 4.4 Position vs. time diagram of a slice of foam from a direct impact experiment at $V_i = 90\text{ m/s}$.



(a)



(b)

Fig. 4.5 Definition of shock and other problem variables for a (a) direct impact test and (b) stationary impact test.

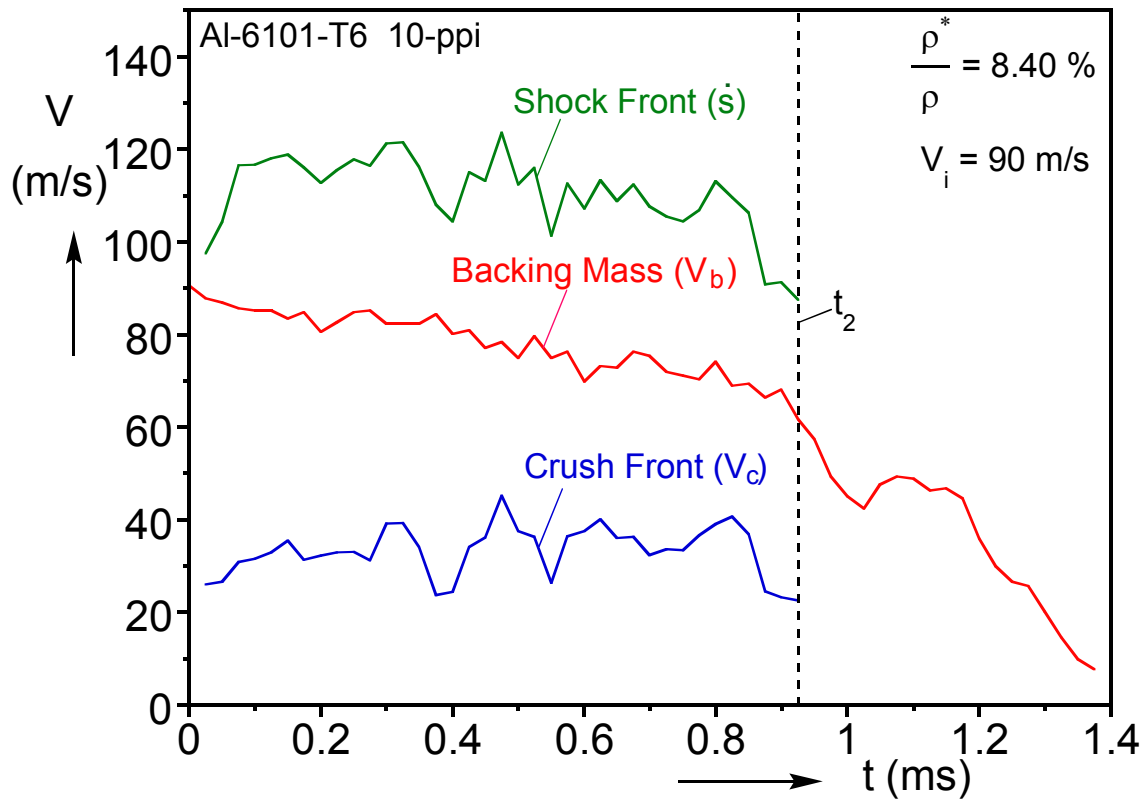


Fig. 4.6 Velocity profiles for a direct impact test at $V_i = 90 \text{ m/s}$.

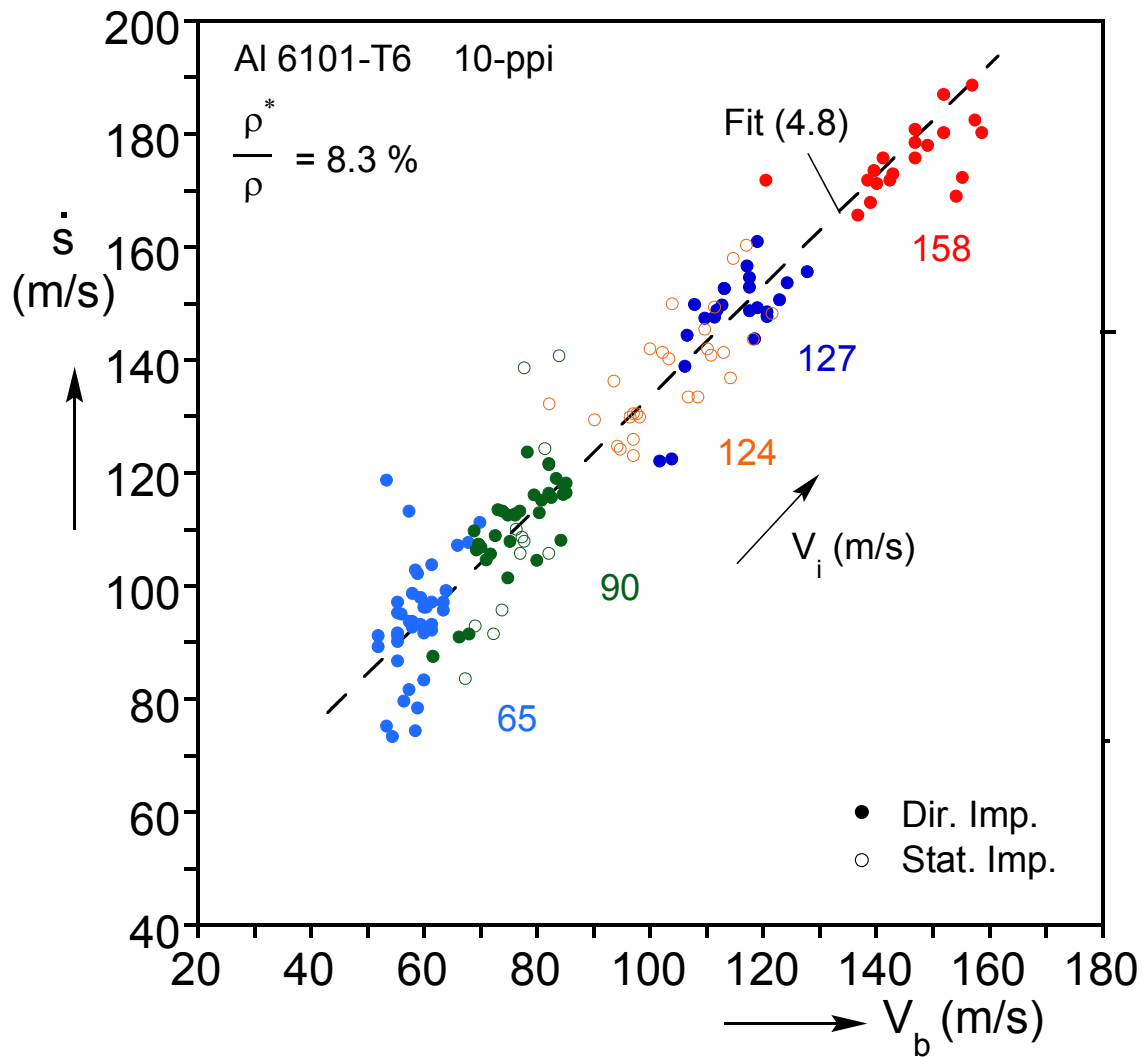


Fig. 4.7 Shock speed-backing mass velocity Hugoniot assembled from several shock experiments.

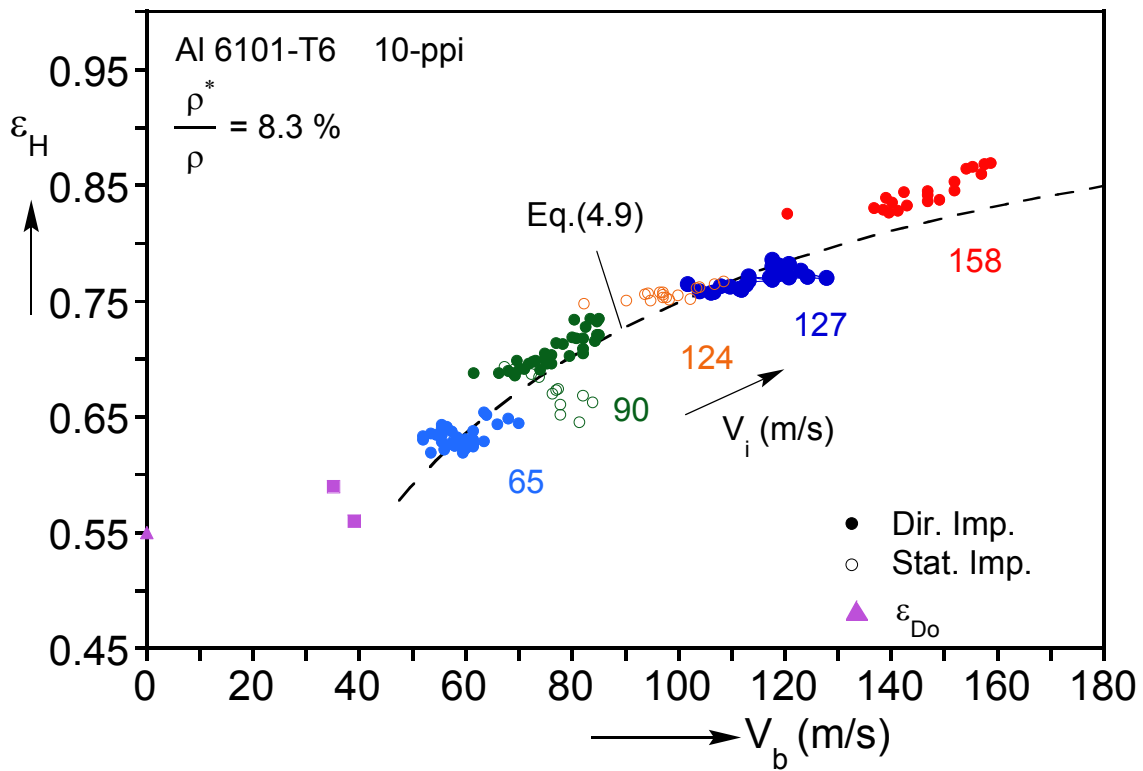


Fig. 4.8 Hugoniot strain-backing mass velocity assembled from several shock experiments.

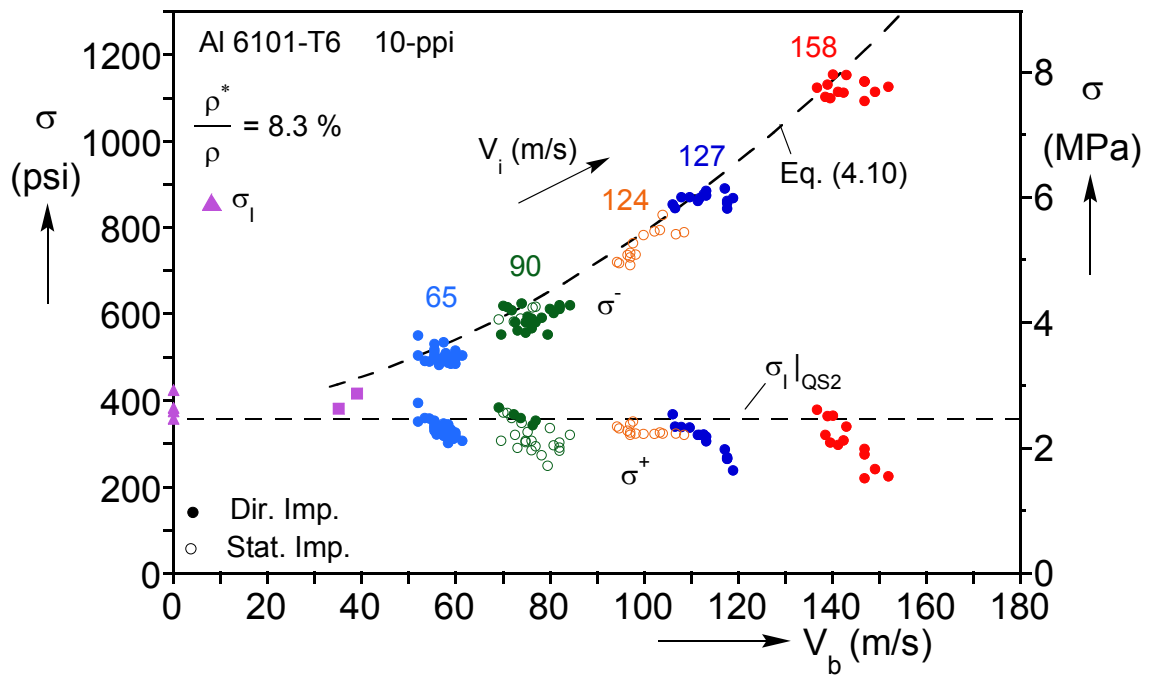


Fig. 4.9 σ^- and σ^+ vs. backing mass velocity assembled from several shock experiments.

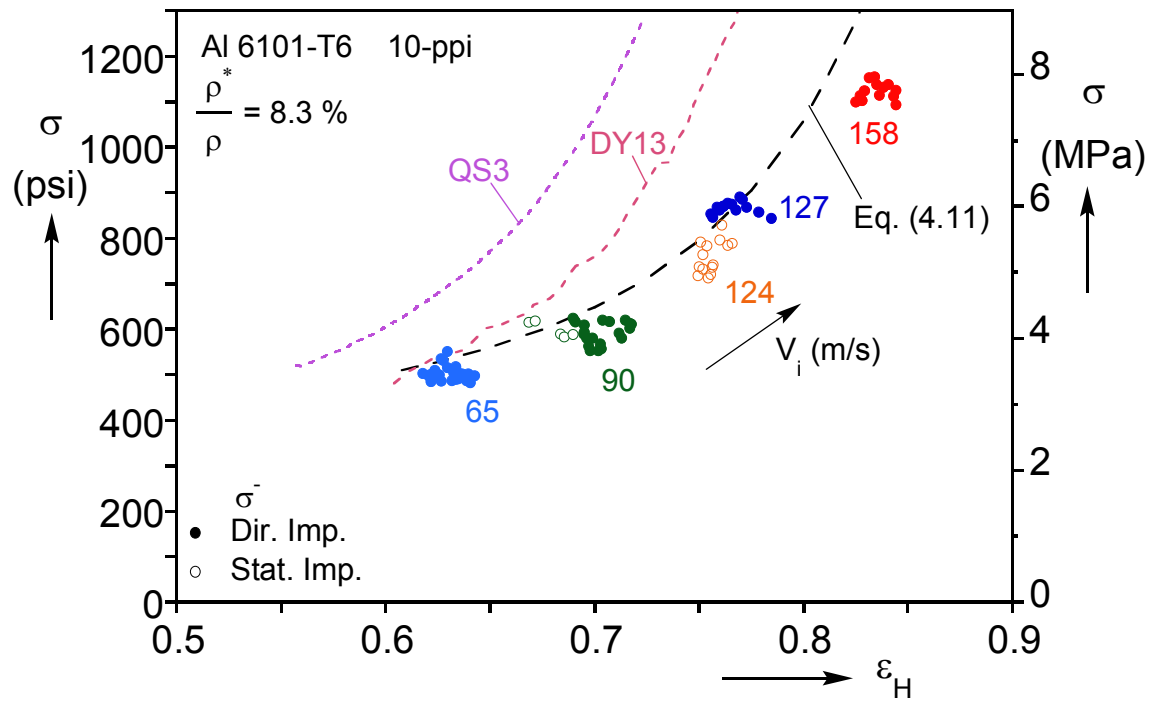


Fig. 4.10 Stress-Hugoniot strain plot from the impact experiments. Included are the convex parts of the responses from QS3 and DY13.

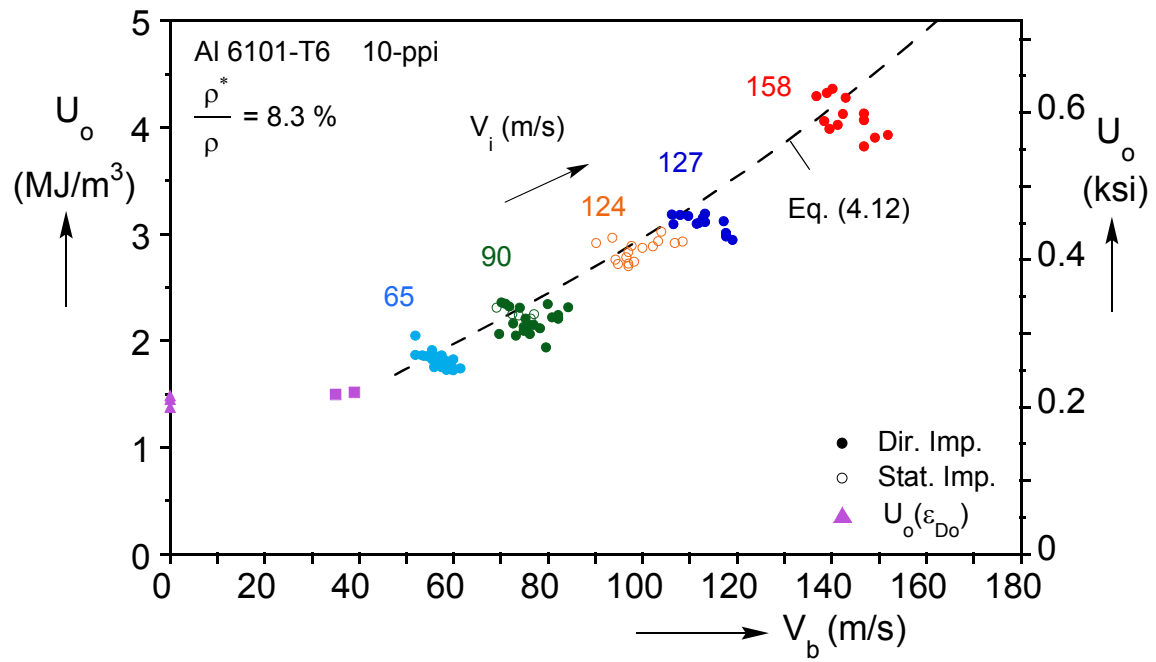


Fig. 4.11 Strain energy expended across a shock vs. backing mass velocity.

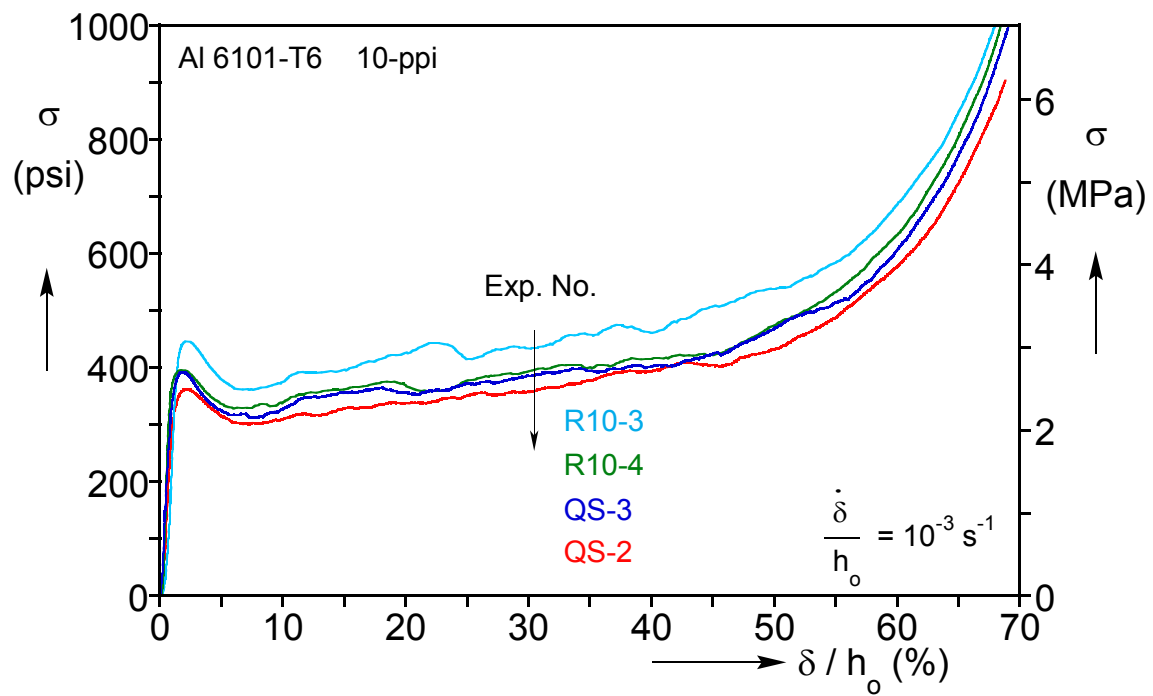


Fig. 4.12 Set of quasi-static nominal stress-displacement crushing responses from the same foam as that used in the impact experiments. The variation in the responses is due to small difference in density and anisotropy between the specimens.

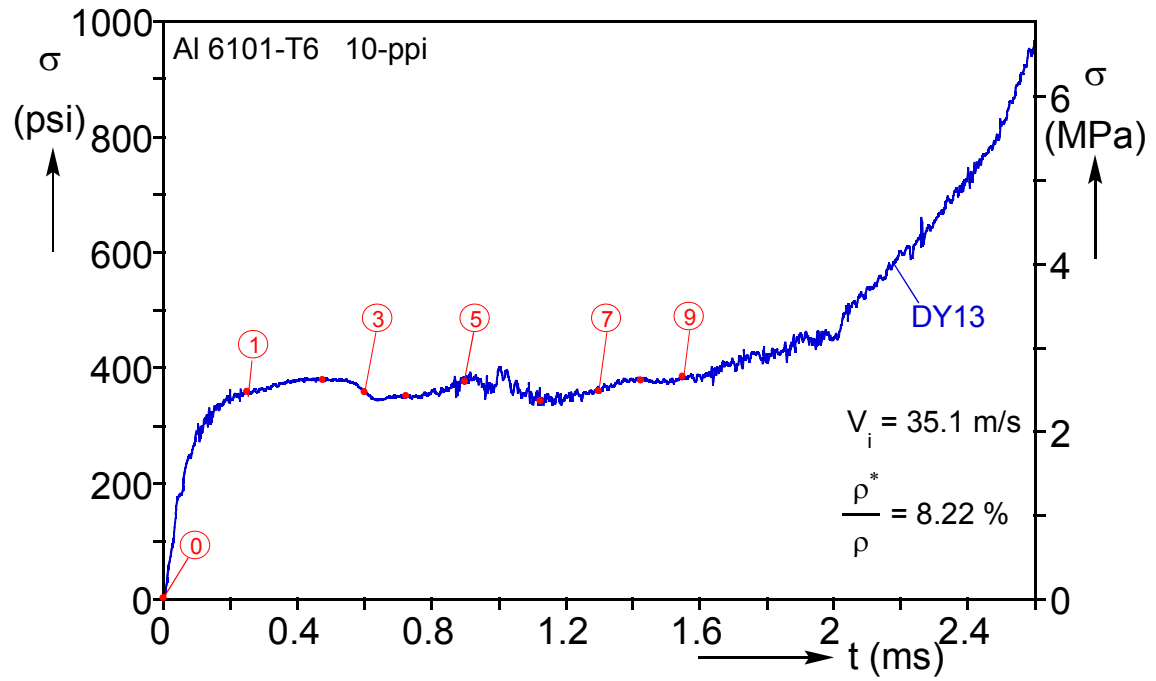


Fig. 4.13 Stress history from a direct impact test with $V_i = 35.1 \text{ m/s}$.

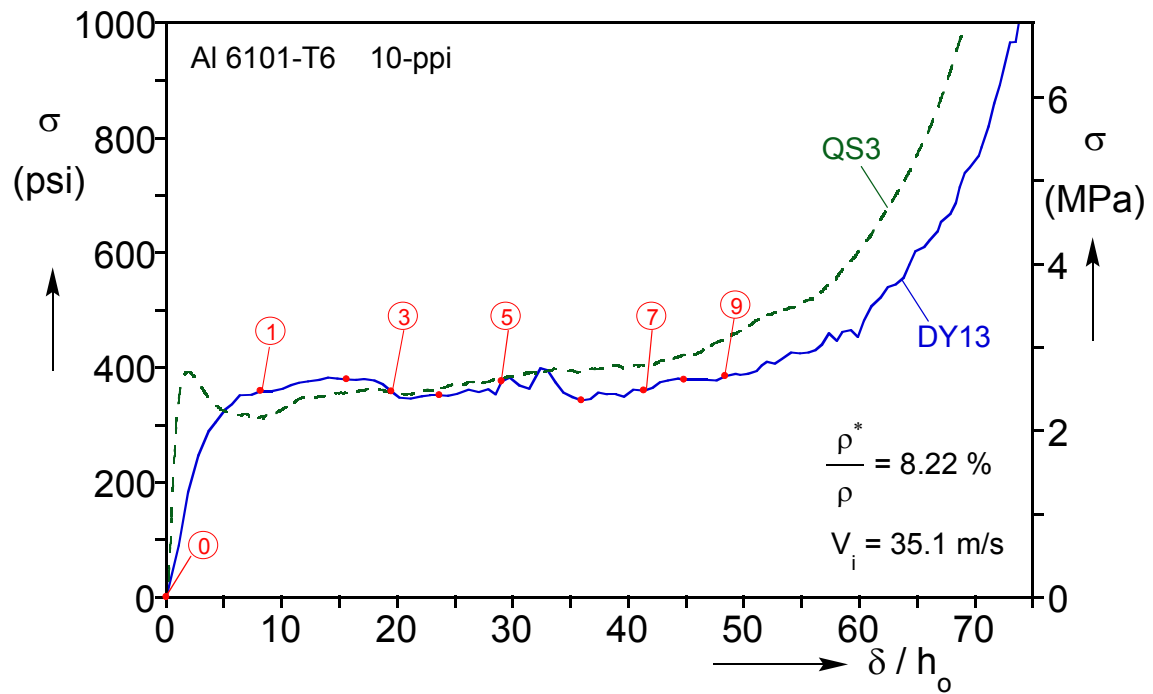


Fig. 4.14 Stress-displacement response from the same experiment.

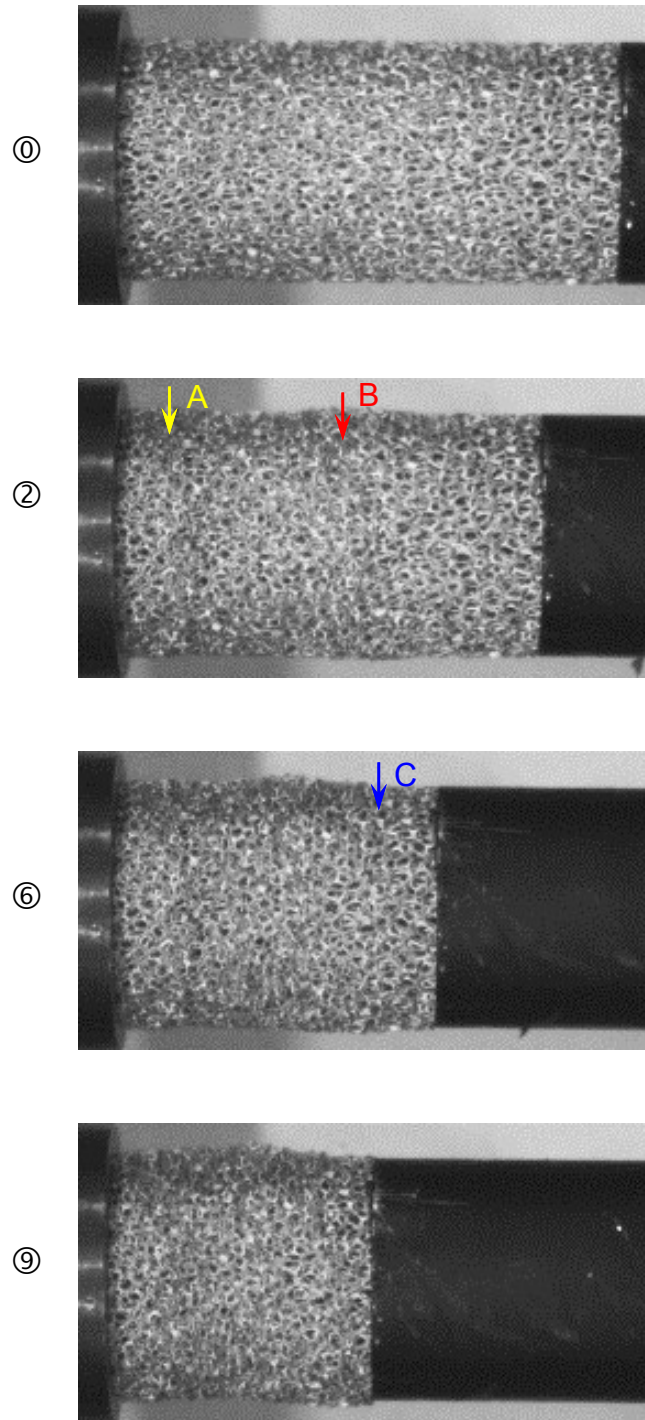


Fig. 4.15 Sequence of images from the high-speed video recording corresponding to times marked on the stress history in Fig. 4.13 with numbered bullets.

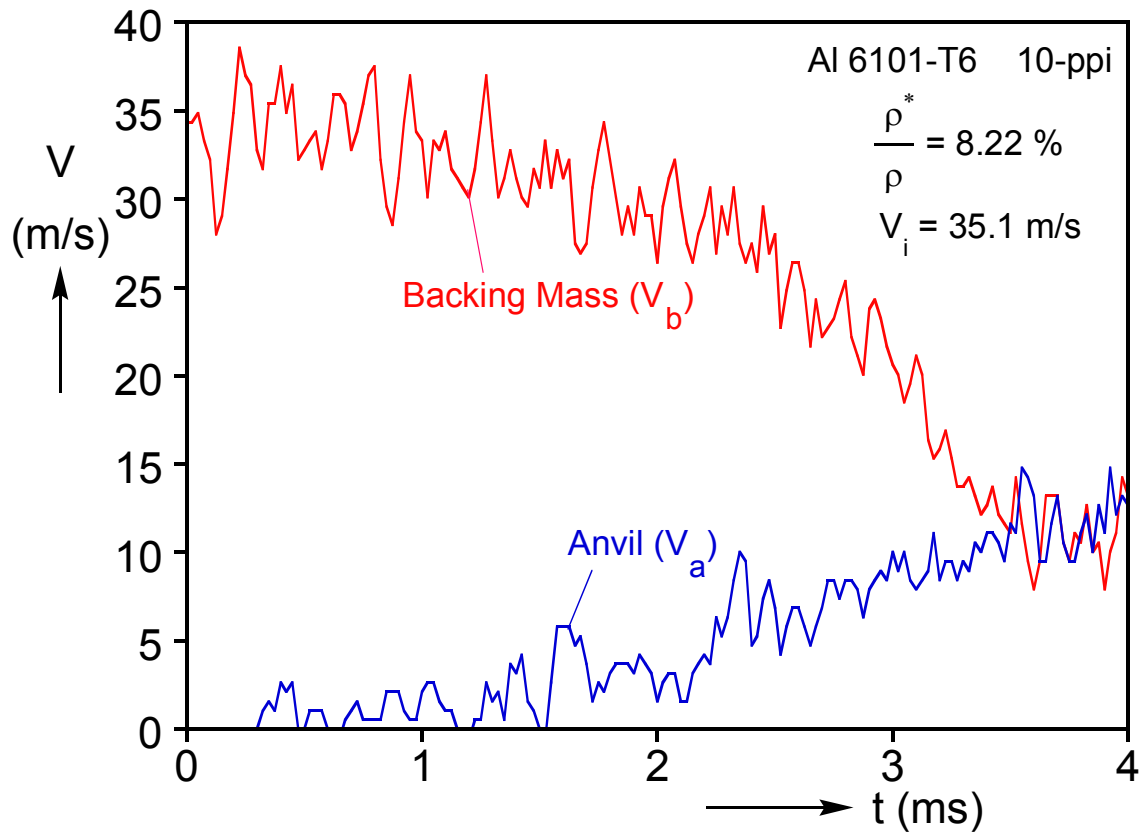


Fig. 4.16 Velocity profiles for direct impact test at $V_i = 35.1$ m/s.

Chapter 5: Dynamic Crushing Simulations

The most relevant work on modeling of dynamic crushing of cellular materials to the present effort comes from the in-plane crushing of honeycomb. Honeycomb is a 2D cellular material that exhibits similar behavior under quasi-static crushing to that of space-filling foams (e.g., see Zhang and Ashby, 1992; Klintworth and Stronge, 1988; Papka and Kyriakides, 1994, 1998a, 1998b). We particularly mention results from three groups that highlight some of the physical aspects of dynamic crushing that were reported in Barnes *et al.* (2014) and in previous experimental efforts: Hönig and Stronge (2002a, 2002b) impacted FE models of hexagonal honeycomb at different speeds and reported inertia driven differences in the initiation of localization, and dynamic enhancement of the crushing stress and the dissipated energy. Ruan *et al.* (2003) using a purely hexagonal honeycomb model and a wider range of impact velocities observed the transition to shock behavior and the formation of shocks above a certain speed. Zou *et al.* (2009) used a similar model to study more in depth the behavior at lower impact speeds, the transition to shock behavior, and the purely shock behavior at higher velocities. They quantified the dynamic stress enhancement and observed that when shocks develop the stress behind the shock remained at the level of the quasi-static initiation stress.

The behavior of space filling foams under impact is examined in this chapter using random foam models such as those described in Chapter 2. The performance of such models is first evaluated by direct comparison of simulations of the dynamic impact experiments reported in Chapter 4. The models are subsequently used to enrich the experimental observations and to elucidate the sub-critical behavior and its transition to shock behavior.

5.1 Dynamic Model

5.1.1 Domain Size, Density and Anisotropy

The majority of the models used here started as cubical spatially periodic random soap froth with 12^3 cells. The periodicity was removed and the models were cropped down to $12 \times 8 \times 8$ cells. An affine deformation was then applied to the microstructure by amplifying the projection of ligaments in the rise direction by a factor $\lambda = 1.1$, while the projections of ligaments in the other two directions retain their original lengths. This value of anisotropy is smaller than the value used in Chapter 3 (and in Gaitanaros *et al.*, 2012) in order to reflect the differences observed in the crushing specimens used (see §4.2.3 and Fig. 4.12).

An important aspect of the dynamic model is that now the density must match that of the actual foam. In other words the mass of the intersecting beam ligaments at each node must be corrected. The scheme used is described in section 2.3.3. By contrast in quasi-static calculations the extra material at the nodes was only corrected for the estimation of the cross sectional area variation (see section 2.3.1).

An example of the skeletal version of a $12 \times 8 \times 8$ cell model is shown in Fig. 5.1. The model will be impacted along the x_1 -direction with the ends in this direction coming into contact with a planar backing mass on one side and a rigid plane that represents the anvil on the other as shown in Fig. 5.2. To facilitate this contact these two ends were slightly cropped so that all edges are co-planar.

5.1.2 Quasi-Static Response

Using the new model size and the anisotropy, we first demonstrate here that the model reproduces accurately the quasi-static crushing of the new set of specimens tested. The corresponding calculated stress-displacement response is shown in Fig. 5.3. Included

in the figure is the quasi-static response measured for specimen QS3 that originated from the same neighborhood of the mother foam block as the impacted specimens (see §4.2.3 and Fig. 4.12). Figure 5.4 shows a sequence of corresponding deformed configurations of a full width slice of the model taken from approximately the middle of the domain. The calculated response tracks the measured one in most respects: the initial elastic stiffness, the first load maximum, the stress plateau and its extent up to an average strain of about 60%. Regarding the densification branch, the model is slightly more compliant than the actual foam as indeed was the case for the results presented in Chapter 3 (see also Gaitanaros *et al.*, 2012). As is the case in experiments, following the stress maximum the deformation localizes at the weakest site in the specimen, which in this case is about one-third of the height from the bottom. In image ①, at a displacement of about $0.05 h_o$, a series of collapsed cells have formed a somewhat disorganized band at this location. It is worth mentioning that this band has a 3D relief across the specimen. In images ② and ③ cell collapse spreads upwards to neighboring cells but in images ④ and ⑤ a second crushing front develops, this time at a location one third of the height from the top. Presumably this takes place because the upward progression of the first crush zone was inhibited by stiffer cells near the mid-height of the specimen. Interestingly, the new band is inclined in the opposite direction from the first one. Beyond point ⑤, crushing starts to affect the upper and lower edges of the specimen that are somewhat stiffer due to the support they receive from the boundaries; consequently, the recorded stress shows a gradual increase that continues until the whole specimen is crushed. Densification, somewhat arbitrarily, is assumed to begin at an average strain of about 55%.

5.2 Dynamic Crushing and Shocks

5.2.1 Initial and Boundary Conditions

We now use similar random models to simulate crushing by impact as performed in the experiments reviewed in Chapter 4. For computational efficiency the size of the model remains at $12 \times 8 \times 8$ so in order for the time response to correspond to the one of the experiments, the length of the model is scaled to that of the specimens (i.e., 4 in—102 mm—for most cases). Both direct and stationary impact simulations are performed. The initial transient and smoothening of the crushing responses introduced by the area discontinuity between the anvil and the pressure bar in the experimental results (see Fig. 4.2) is avoided here by having the specimen contact rigid planes at both ends as shown in Fig. 5.2. Direct impact is simulated by attaching the specimen to a rigid mass M_b that is assigned an initial velocity V_i ; the two in turn impact a rigid stationary plane as shown in Fig. 5.2a. For stationary impact, the foam model is attached to a stationary rigid plane and is impacted by a rigid planar mass assigned an initial velocity that again corresponds to the one of the experiments simulated (Fig. 5.2b). In both types of simulations M_b is chosen such that ratio M_b / M_f matches that of the corresponding experiment ($M_f \equiv$ mass of foam model).

5.2.2 Simulation of Direct Impact that Develops Shocks

The modeling framework outlined above is now used to simulate the direct impact experiment with initial impact speed $V_i = 90$ m/s. The backing mass-foam mass ratio, M_b / M_f , is assigned the experimental value of 3.837 and the foam-mass system is given an initial velocity of 90 m/s. The foam impacts the stationary plane and immediately cell crushing commences next to it. Figure 5.5a shows a plot of the nominal stress (force/foam undeformed cross sectional area) exerted on the rigid plane (σ^-) and

Fig. 5.5b the stress felt by the traveling mass (σ^+). The stress response measured through the pressure bar in the corresponding experiment is included with a dashed line in Fig. 5.5a for comparison. Figure 5.6 shows a set of deformed configurations of an axial slice of the model that correspond to the numbered bullets on the responses in Fig. 5.5. The shock is seen to start on the left and propagate to the right consuming the specimen within 1 ms.

On impact, stress σ^- exhibits a sharp rise but quickly drops down to a relatively ragged plateau. The extent of the initial stress peak is governed by the time step chosen to extract the data from the numerical solution and thus it will not be further scrutinized. The stress on the distal (σ^+) is due to elastic wave action and consequently its rise is delayed somewhat until the stress wave traverses the length of the specimen. Furthermore, σ^+ follows much lower stress level and is smoother than σ^- . In image ① at $t = 0.125$ ms, cells adjacent to the stationary plane have crushed forming a relatively sharp front that we define as the “shock”. Subsequently, in images ② to ⑦ the shock propagates to the right leaving behind it crushed cells while ahead of it the cells appear undeformed. An enlarged view of the shock front in image ④ at $t = 0.503$ ms is depicted in Fig. 5.7. The front can be seen to be reasonably planar but the discrete and random nature of the cellular microstructure implies that it has a width that is of the order of one-half of a cell diameter. The number of undulations in the stress response is probably related to the number of cells in the model along the crushing direction. The amplitude of the undulations is also influenced by the fact that as the shock is traversing the specimen it encounters some “stronger” and some “weaker” cells. Since the force transmitted to the stationary plane at a given time represents the integral of the resistance encountered at that instant, the force can vary with axial position. The undulations continue until the

shock reaches the moving plane on the right (⊗ at $t = 0.987$ ms) when the stress takes an upward trajectory.

The σ^- response measured in the corresponding experiment included in Fig. 5.5a with a dashed line, is seen to be in good agreement with the mean value of the calculated one for $t > 0.3$ ms. It has a level of about 610 psi (4.21 MPa), which is higher than the quasi-static crushing level. As mentioned in Chapter 4, the discontinuity in cross sectional areas at the anvil-bar interface masks the initial transient and has a smoothing effect on the recorded stress level. This will be further examined in the next section with the help of a more representative model of the experimental setup.

Returning to Fig. 5.5b, the stress on the moving plane rises smoothly to a level just under 400 psi (2.76 MPa) and traces a plateau for about 0.2 ms. It then drops to a local minimum and subsequently hovers at a stress level that is somewhat below 400 psi. It is interesting that this stress picks up earlier than at the proximal end probably because as the shock approaches the rigid plane it may interact with it. Included in the figure is the initiation stress ($\hat{\sigma}_I$) from the quasi-static crushing calculation on the same model reported in Fig. 5.3. As observed in the experiments, this value appears to bound the σ^+ response from above (a similar observation was made in Zou *et al.* (2009) for in-plane impact of regular honeycomb).

The calculation of the velocities and other problem variables is extracted from the solution as follows. The velocity of the backing mass, V_b , is evaluated by tracking its position in time. The time history of V_b is drawn with solid line in Fig. 5.8 together with the corresponding one from the experiment. The analysis is seen to track very closely the deceleration of the backing mass experienced in the experiment so that when the shock consumes the specimen ($t_2 = 0.93$ ms) the velocity is reduced to about 60 m/s.

As mentioned above, although the shock front is essentially planar it has a rather ragged relief and thus determination of its position with time must be performed with care. The dashed red line drawn in Fig. 5.7 shows the best estimate of its position in image ④, which came from approximately the mid-width position. This is repeated at different locations across the width and similarly from the corresponding skeletal views (e.g., Fig. 5.1). The average of these estimates produces $h_c(t)$ and $h_i(t) = h_b(t) - h_c(t)$. The position of the front in the undeformed configuration is then $s(t) = h_o - h_i(t)$ and its velocity is the time derivative $\dot{s}(t)$. The velocity of the crush front is given by $V_c = \dot{h}_c(t)$. The resultant shock and front velocities are compared to the experimental results in Fig. 5.8. Because of the relatively small number of cells in the model, fewer data points can be extracted from the analysis. However, the calculated trajectories are generally smoother than the measurements and follow the trend of the experiments quite well.

Another illustration of the shock formation and propagation appears in Fig. 5.9a that shows a position-time plot of a narrow strip taken out of the crushing model. The first image at the bottom shows the foam and backing mass approaching the stationary plane. The subsequent 14 images, separated by 0.082 ms, show the initiation of crushing on the impacted plane and the propagation of the crushing front towards the approaching backing mass. The last image at the top at $t = 1.066$ ms shows the foam fully crushed. A more quantitative plot of the dynamic events is shown Fig. 5.9b where $x - t$ trajectories of a number of points along the length of the strip are plotted (x represents positions measured from the impacted end—Lagrangian frame). Included is the trajectory of the backing mass, which quantifies its gradually decreasing velocity. The different points are seen to initially follow the trajectory and velocity of the backing mass but, starting from the bottom and moving up, one by one comes to a stop as it enters the crushed zone and

then stays at rest until the crush front reaches the backing mass at about 1 ms. Beyond this point, the crushed foam undergoes additional compaction as indicated by the sloping of the trajectories for $t > 1$ ms.

5.2.3 Effect of the Anvil-Bar Interface

In the way of trying to reproduce the experimental results, and at the same time demonstrate the effect of the anvil/bar discontinuity on the measured response, we repeat the direct impact simulation of 90 m/s but now include the bar as well as the anvil in the model. Thus the stationary plane is replaced with a linearly elastic solid anvil-bar system as shown in Fig. 5.10. In view of the square cross section of the foam model, the bar and anvil have square cross sections also but are assigned the same area ratios as in the experiment, that is $A_{\text{anvil}}/A_{\text{bar}} = 25$. They are both meshed with 8-node solid elements and are assigned the mechanical properties of steel: elastic modulus $E = 30 \times 10^3$ ksi (207 GPa), Poisson's ratio $\nu = 0.3$, and mass density $\rho = 0.2932$ lb/in³ (8120 kg/m³). To avoid complications from reflecting waves, the end of the bar is assigned nonreflecting boundary conditions. This also allows use of a shorter bar as shown in the same figure.

Figure 5.11a shows the stress σ^- recorded at the far end of the model bar. The initial sharp spike recorded on the rigid plane (Fig. 5.5a) has been replaced by a smooth rise up to a time of approximately 0.3 ms followed by a relatively flat plateau at about 600 psi (4.14 MPa) that continues until about 1.0 ms. Furthermore, the anvil-bar system has also “filtered out” the stress undulations seen in the corresponding response from the rigid boundary in Fig. 5.5a. Included in the figure is the corresponding response measured in the experiment, which is seen to follow the calculated one quite well. A small difference is that in the calculation the pickup in stress at the end of crushing is somewhat delayed.

Figure 5.11b shows the stress recorded at the distal end (σ^+ , Anal.), which of course remains the same as the one from the calculation without the anvil-bar boundary reported earlier in Fig. 5.5b. For completeness, we also use the bar calculated stress, σ^- , together with the appropriate velocities in Eq. (4.6) to evaluate the stress on the distal end as was done in the experiment. This response is included in Fig. 5.11b (Anal. Bar) together with the one calculated in a similar manner in the experiment. The two are seen to be similar missing the initial rise of the actual response exhibited for $t < 0.3$ ms.

5.2.4 Constant Velocity Impact

Thus far, we have simulated the process used to conduct the direct impact experiments, as described in Chapter 4. In other words, the backing mass and specimen were assigned an initial velocity and a kinetic energy sufficient to fully crush the 4-inch (102 mm) long foam. Under these conditions the velocities of the backing mass and material ahead of the shock gradually drop. Numerical modeling provides the option of prescribing the moving plane at the distal end at a constant velocity, which produces cleaner results. Therefore, the 90 m/s impact simulation is now repeated but the moving rigid plane is assigned a constant velocity. Figure 5.12a shows the calculated stresses acting on the proximal and distal end planes and Fig. 5.12b shows the variation of the three relevant velocities with time (compare with Fig. 5.8). The prescribed moving plane velocity (V^+) is now constant and so is the velocity of the shock, \dot{s} (within the accuracy of the measurements). The stress behind the shock (σ^-) again exhibits a similar initial sharp rise followed by a stress plateau with an initial level of about 610 psi (4.21 MPa) that lasts until $t \approx 0.28$ ms. Beyond this point, the stress fluctuates about a mean value of about 670 psi (462 MPa) with a somewhat larger amplitude that is comparable to that of the undulations in Fig. 5.5a. By contrast, the corresponding stress level in Fig. 5.5a

exhibits a small gradual drop due to the decreasing value of V^+ and \dot{s} . Because the impact velocity is constant, the shock traverses the specimen earlier than in Fig. 5.5a and σ^- starts to rise earlier, about 0.8 ms after first impact. The stress ahead of the shock, σ^+ , is similar to the one in Fig. 5.5b with a plateau of around 400 psi (2.75 MPa) up to 0.3 ms followed by a somewhat lower level plateau that lasts until the shock goes through the specimen. Because of the constant V^+ and the nearly constant \dot{s} , the lower plateau is smoother with a somewhat higher level than the corresponding one in Fig. 5.5b.

5.2.5 Effect of Cell Size

The main random foam cell model used in this study has a domain of $12 \times 8 \times 8$ cells. In order for the time events to correspond to those recorded in the experiments, the model was scaled to have the same length as the actual foam specimens tested. This results in rather large cells that promote more discrete behavior (Fig. 5.5a). This issue is now further scrutinized using a model with 18 cells in the crushing direction ($18 \times 8 \times 8$ cells). This model was assembled from a 10^3 periodic domain soap froth by joining two adjacent sides together, and removing redundant vertices on the shared cube face. The model is dressed with beam elements in a similar fashion ending up with the same relative density. Anisotropy of $\lambda = 1.1$ was introduced, the periodicity was removed from all sides, and all sides were cropped down to end up with an $18 \times 8 \times 8$ cell model. The same scaling as before was applied making the 18-cell direction 4.0 in (102 mm) long. Since the original soap froth model was generated independently from the 12^3 model used to produce the results presented thus far, it has a different monodisperse microstructure. Therefore, the results will also serve as a test of the effect of differences in the random microstructure on shock formation and the dynamic crushing results in general.

Figure 5.13a shows the calculated σ^- and σ^+ stress histories for a simulation of the 90 m/s direct impact experiment. Figure 5.14 portrays a set of deformed configurations that show the evolution of the shock through the model foam (again slice shown taken through the mid-width). The more numerous cells along the length, the higher aspect ratio, and the difference in the random microstructure can be clearly seen by comparing the initial configurations, ©, in Figs. 5.14 and 5.6. For completeness, the three relevant velocities are compared to the experimental ones in Fig. 5.13b. The backing mass velocity follows very closely the experimental record and the same can be said about the shock and crush front velocities. One can see however, that this longer cell model enables the extraction of more data points with improved accuracy for the latter two velocities. The σ^- history follows essentially the same path as the 12-cell long model—included in Fig. 5.13a with a dashed line. The main difference is that the stress undulations are more numerous with different characteristics. This confirms that they are related to the number of cells along the length of the model and to the exact nature of the random microstructure encountered by the shock as it moves across. The calculated σ^+ stress history is also similar to the one in Fig. 5.5b. Thus, overall we can conclude that the number of cells along the length of the model does not influence the major issues of concern, that is the velocity of the shock, the stresses induced in front and behind it, and the energy absorbed. Furthermore, the different random microstructure used here did not affect the major results of interest in any significant way either.

5.2.6 Direct Impact at Different Velocities

All impact experiments performed were simulated numerically using the same relative density $12 \times 8 \times 8$ cell model assigned the initial kinetic energy used in each experiment. The behavior was found to follow along the same general trends as the one

described for the 90 m/s direct impact simulation. The calculated σ^- and σ^+ stresses vs. time for initial impact velocities of 65, 75, 90, 127 and 158 m/s are compared in Fig. 5.15 ($V_i = 75$ m/s is included for completeness even though an experiment was not performed at this velocity). To accommodate this comparison, in each case time is normalized by h_o / \bar{s} where h_o is the height of the model (4.0 in—102 mm) and \bar{s} is the average velocity of the shock. This normalizing variable approximately represents the time it takes the shock to consume the specimen. So, with this normalization the stress histories become analogous. Consequently, in Fig. 5.15a the calculated σ^- stresses are seen to follow the same trends for the five cases but at different average stress levels. In addition, the stress undulations are seen to occur at very similar normalized times but their amplitudes decrease with V_i . So for the 65 m/s simulation the amplitude of the undulations has decreased significantly. The mean stress levels follow closely the experimental values in Fig. 4.9 and the termination of the stress plateaus are seen to be nearly coincident. The subsequent rising parts of the responses have different slopes because, among other reasons, the time normalization adopted is not appropriate for the additional compaction phase that takes place.

Figure 5.15b shows the corresponding σ^+ stress histories. They are all much smoother, trace similar stress plateaus that are at about 400 psi (2.76 MPa), and pick up somewhat earlier than the corresponding σ^- values. The small shifts in the initial rises are also caused by the normalization adopted.

5.3 Hugoniot: Comparisons of Experiments and Analysis

The 12×8×8 cell model was used to generate impact results for velocities in the range of 50-200 m/s. To ensure consistency in the results these calculations were performed at constant impact velocities ($V^+ = \text{const.}$) in the manner described in §5.2.4.

Figure 5.16 shows the experimentally generated $V_b - \dot{s}$ Hugoniot together with the numerically generated results ($V^+ - \dot{s}$, \blacktriangle). Included also with dashed lines are linear best fits of the experimental and numerical data. The fit of the numerical results gives $\dot{s} = A + BV^+$, with $A = 28.454$ and $B = 0.996$ ($R^2 = 0.9997$). This nearly perfectly linear fit is in quite good agreement with the experimental data. It has nearly the same slope as the fit of the experiments but a slightly lower intercept (see §4.2.2).

The numerical runs were used to also extract the strain behind the shock (Hugoniot strain ε_H). Figure 5.17 shows a comparison between the experimental and numerical $V - \varepsilon_H$ Hugoniot curves. A power-law fit of the numerical data is also included. The numerically calculated values of ε_H follow a similar dependence on velocity as the experimental data. The fit is slightly higher than the data at lower velocities and slightly lower at the highest velocity. At the last impact velocity analyzed (200m/s) ε_H reached a value of 0.87.

Figure 5.18 compares the $\sigma^- - V^+$ Hugoniot with the corresponding experimental one. The stress behind the shock, σ^- , follows the approximately quadratic increase with velocity of the measurements. Included in the figure are the stresses ahead of the shock σ^+ . The levels remain essential constant with velocity at about 390 psi (2.69 MPa), again in concert with the experimental values. For both sets the numerical results exhibit minimal scatter and are in very good agreement with the measurements. The lowest velocity for which shock results are included is 50 m/s. The fit of the calculated data is seen to approach from above the constant σ^+ level, with the transition from no-shock to shock behavior estimated to be between 40 and 50 m/s. Finally, included in the figure is the initiation stress ($\hat{\sigma}_I$) of the calculated quasi-static response from the same model (391.5 psi—2.70 MPa). This stress level, also drawn with a dashed

line, is seen to be a close upper bound of the calculated σ^+ stresses, which confirms the assumption reported in Chapter 4.

5.4 Impact at Subcritical Velocities

The same family of foam models was used to first simulate one of the subcritical impact speed experiments described in the previous chapter and then to perform a parametric study that covers impact velocities in the range of 5-50 m/s. We start with a direct simulation of the 35.1 m/s impact experiment (see §4.3). In this case, for clearer visualization of the deformation patterns that develop, the 18×8×8 cell model is used. In concert with the experiment, the model includes the bar and anvil (see Fig. 5.10), and the backing-foam mass ratio is assigned the experimental value of 33.9. Figure 5.19a shows the calculated nominal stress history at the proximal end along with the corresponding experimental one. The stress recorded at the distal end is plotted vs. time in Fig. 5.19b while a set of corresponding deformed configurations are included in Fig. 5.20. Figure 5.21 presents a comparison of the measured and calculated backing mass velocities. The calculated velocity is seen to track the experimental one very well but its trajectory is smoother. It is also worth noting that 2 ms into the crushing process the velocity has dropped to 29.3 m/s.

The stress measured at the end of the bar follows a trajectory that is very similar to the experimental one. Because of the anvil/bar interface, the expected initial transient in the response is again filtered out. For $0.3 < t < 1.8$ ms the response exhibits a relatively flat plateau with an average value of about 415 psi (2.86 MPa), in other words a somewhat higher level than the initiation stress of the corresponding quasi-static (QS) crushing calculation indicated in the figure with a dash line ($\hat{\sigma}_I = 399$ psi—2.75 MPa). As in the experiment, the stress picks up at about 2.0 ms. The stress at the distal end is

not influenced by the presence of the anvil and so it exhibits an initial maximum that is essentially at the level of the QS initiation stress. Note that the experimental response shown is evaluated from the stress history measured by the pressure bar and consequently is influenced by the anvil/bar interface. The calculated response subsequently follows a somewhat lower plateau than the stress in Fig. 5.19a at a level of about 375 psi (2.59 MPa). This stress starts rising at about 1.6 ms forming a short duration second plateau that ends at about 2.4 ms.

The deformed configurations in Fig. 5.20 show the crushing to first develop at the stationary plane on the LHS. In configuration ①, shock-like behavior appears to be taking place but the front is less well defined than at higher impact speeds and leaves behind cells that are not fully crushed. This is also illustrated in configuration ② where in addition crushing has commenced at a second site marked with a red arrow. Remembering that the image represents a slice at mid-width of the model, this is a manifestation of a wider crushing zone. In image ③, the torturous propagation of the crushing front on the LHS has continued, but cell crushing at the second site has increased. Interestingly, cell crushing has now also initiated at a third site indicated with a yellow arrow in the image. In image ④, the new crush zone on the right now covers the full width of the model. Its inclination is opposite to that of the main crushing front, leaving between the two a trapezoidal shaped wedge of intact material. This pattern is incompatible with planar deformation and consequently the specimen develops some local bending. In image ⑤, this wedge has also been nearly crushed but the bending remains. A narrow zone of nearly intact cells adjacent to the moving backing mass on the RHS is also observed. At this point the stress on the moving mass on the RHS starts to increase while the stress on the opposite end remains at a lower level. This increase may result from interaction between stress waves emanating from the moving mass and the

moving crushing front. In image ⑥, most of the specimen has crushed although some relatively undeformed cells remain dispersed throughout the model. The stress on the RHS is traversing a local plateau at a higher level and the stress on the stationary plane starts to rise.

From the results we can conclude that at this impact velocity, the model exhibits shock behavior initially but subsequently develops multiple crushing sites very much mimicking the corresponding experiment. The plateau stress at the proximal end is somewhat higher than the quasi-static initiation stress, an indication of moderate enhancement by inertia. The stress at the distal end is initially close to the QS stress but drops somewhat below it during the main crushing event.

We now present results from a wider study of sub-critical impact velocities. For consistency this is performed with the same $12 \times 8 \times 8$ cell model. Furthermore, in order to sharpen the transition to shock formation, the impact velocity is kept constant throughout the simulation. Results from impact velocities of 5-50 m/s are compared. Figures 5.22a and 5.22b show respectively the calculated proximal and distal end stresses plotted against the normalized end displacement ($\delta/h_o \equiv \bar{\delta}$) for four impact speeds. Included for comparison are corresponding results for QS crushing. In order to contrast the subcritical and critical crushing behavior, Fig. 5.23 shows sets of deformed configurations from each impact speed at average displacements of $\bar{\delta} = \{0.10, 0.15, 0.20, 0.25, 0.35\}$ (marked in the figures with \times).

In the QS case, the stress follows the usual trend with an initial stress maximum followed by a stress plateau that extends to $\bar{\delta} \approx 55\%$. Cell crushing initiates at a site approximately three rows of cells from the bottom. Cell collapse propagates upwards but without a well-defined front, as bands of crushing develop at multiple sites (see image at $\bar{\delta} = 20\%$). In the fourth image, the crushing zone in the upper third of the model has

consumed the full width of the model and intact cells remain between the two crushing zones. In the image at $\bar{\delta} = 35\%$, the two zones of crushing have nearly coalesced, leaving behind intact cells close to the ends. By $\bar{\delta} \approx 55\%$, the remaining cells crush also and the stress takes an upward trajectory.

At impact speed of 5 m/s, deformation localizes at exactly the same site as in the QS case and the two stresses develop a local maximum that is at the same level. Subsequently, in contrast to the QS case, crushing first propagates downwards and the upwards spreading is delayed until the third image while the two stresses are at about the same level as in the QS response. Localized crushing initiates also in the same upper site but at $\bar{\delta}$ levels of 25% and higher. The propagation of crushing is also completed here by $\bar{\delta}$ of about 55% and beyond this point the two stresses follow the trajectory of the QS case.

When the model is impacted at 20 m/s, the domain remains free of shocks and crushing initiates and evolves, including the development of multiple crushing sites, in a very similar manner as in the 5 m/s case. Furthermore, the two stresses follow similar trajectories that are also almost identical to the QS one. This implies that energy absorbed by the end of the stress plateaus is also similar to that of the QS case. In other words, no significant enhancement of stress or energy absorption can be reported up to this impact speed.

The behavior starts to change at impact velocity of 35 m/s and higher. Here, crushing initiates at the impacted plane creating what we may call, a “weak shock” front. Soon thereafter, however, the site where localization first initiated in the QS case also collapses (see $\bar{\delta} = 0.15$). Subsequently, the “shock” as it propagates upwards catches up to this site as illustrated in the images for $\bar{\delta}$ of 20% and 25%. At higher values of $\bar{\delta}$ (e.g., 35%), localized crushing has also initiated in the second site in the upper third of

the model. In other words, the mixed shock/non-shock behavior observed in the non-constant crushing speed for $V_i = 35.1$ m/s experiment and simulation in Fig. 5.20 is repeated here. We thus conclude that for this foam 35 m/s impact lies in a transitional regime from non-shock to shock behavior. This conclusion is also supported by the recorded stresses in Figs. 5.22a and 5.22b. The stress at the proximal end is seen to have separated from the trajectories of the lower impact speeds indicating some inertial enhancement. The stress at the distal end follows a stress plateau that is at about the level of the initiation stress of the QS case, but picks up somewhat earlier and develops a similar second plateau as the case in Fig. 5.19b.

At impact of 50 m/s the model clearly exhibits shock behavior, i.e., localized crushing initiates at the proximal end forming a clear shock front that propagates at a well-defined speed from one end to the other. Behind it, the foam is crushed and the stress is higher as illustrated in Fig. 5.22a. In front of it, the foam is essentially uncrushed and the stress hovers at about the level of the initiation stress of the QS case.

In summary, for impact speeds of 20 m/s and lower crushing initiates at the weakest site, spreads locally until localization becomes preferred at another site, followed by third and so on. In other words, the crushing evolves in a manner that is similar to the QS case. Furthermore, the stress trajectories followed at the proximal and distal ends are similar in all respects to the QS one and so is the induced deformation. Thus, in this velocity regime inertia effects are very limited if any. Between 25 and 35 m/s inertial effects start to have more influence. Crushing initiates at the proximal end, the corresponding stress starts to increase and separate from the one recorded at the distal end, and the induced strain is somewhat larger. However, crushing continues to also initiate at other sites, so the overall behavior is closer to the QS one but at an increasing stress and strain. At 50 m/s the models exhibit clear shock behavior with all

characteristics associated with it. Thus, the transition to shock behavior is gradual rather than abrupt. Although this conclusion could be influenced to some degree by the size of our model, we place the transition to shock behavior take place between 40-50 m/s.

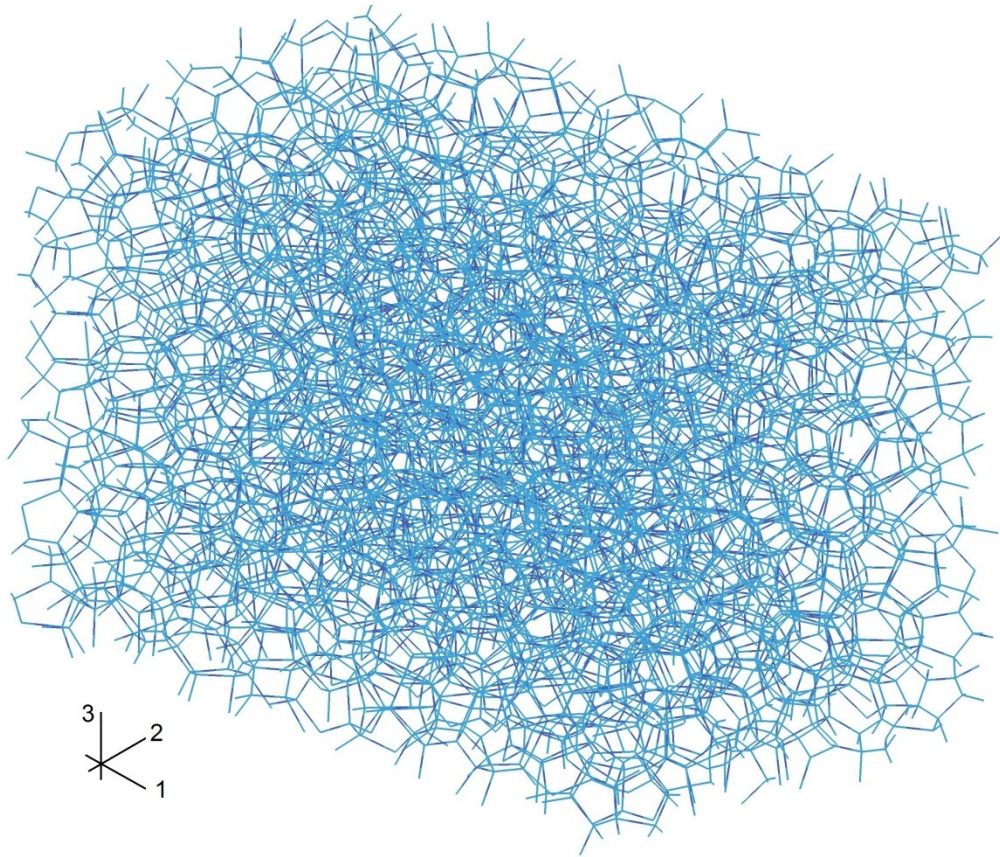
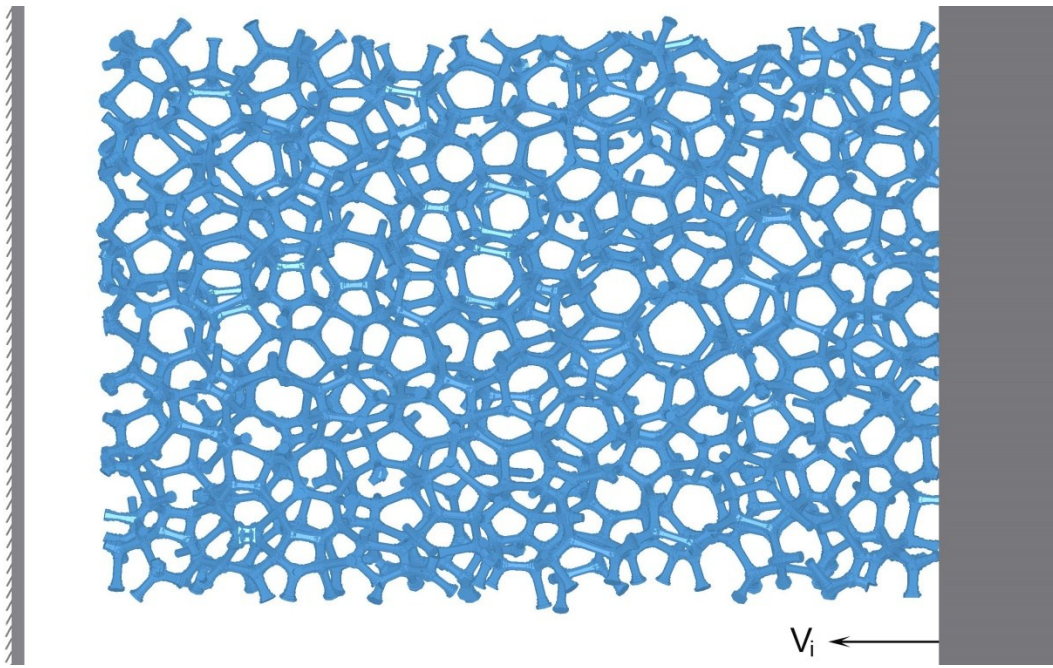
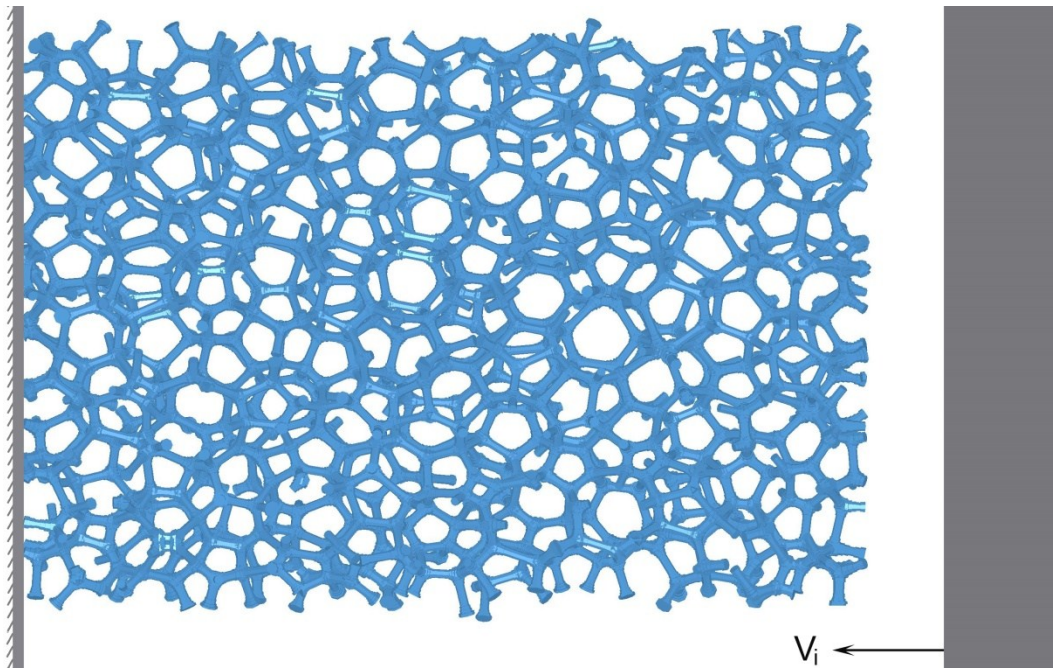


Fig. 5.1 Three dimensional rendering of random soap froth with $12 \times 8 \times 8$ cells.



(a)



(b)

Fig. 5.2 Foam models for (a) direct and (b) a stationary impact.

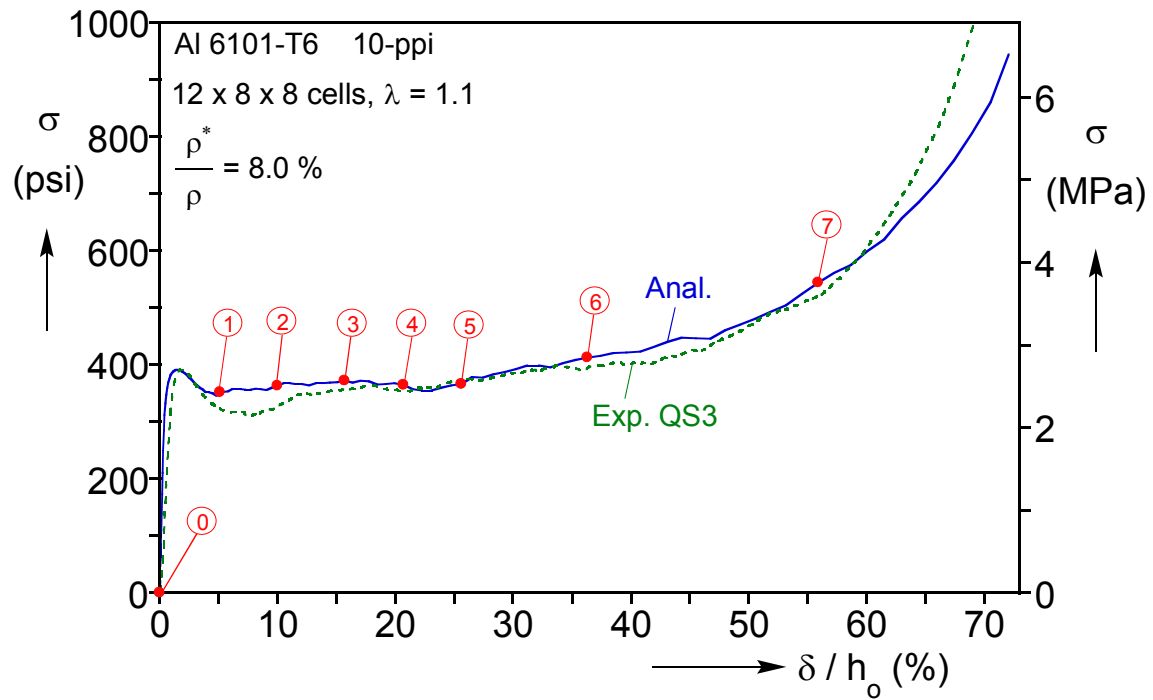


Fig. 5.3 Comparison of calculated and measured quasi-static stress-displacement responses using the 12×8×8 cell model.

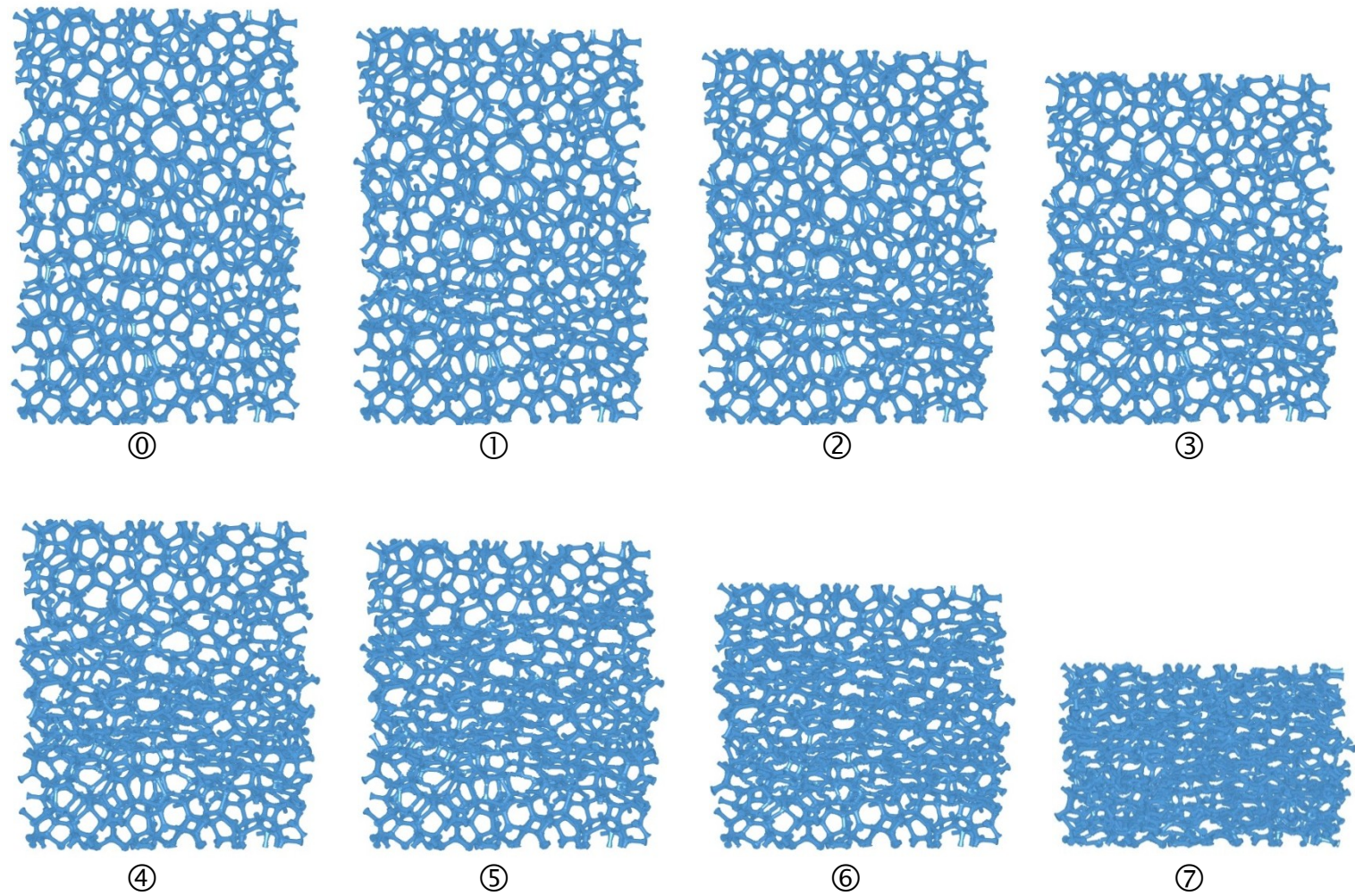
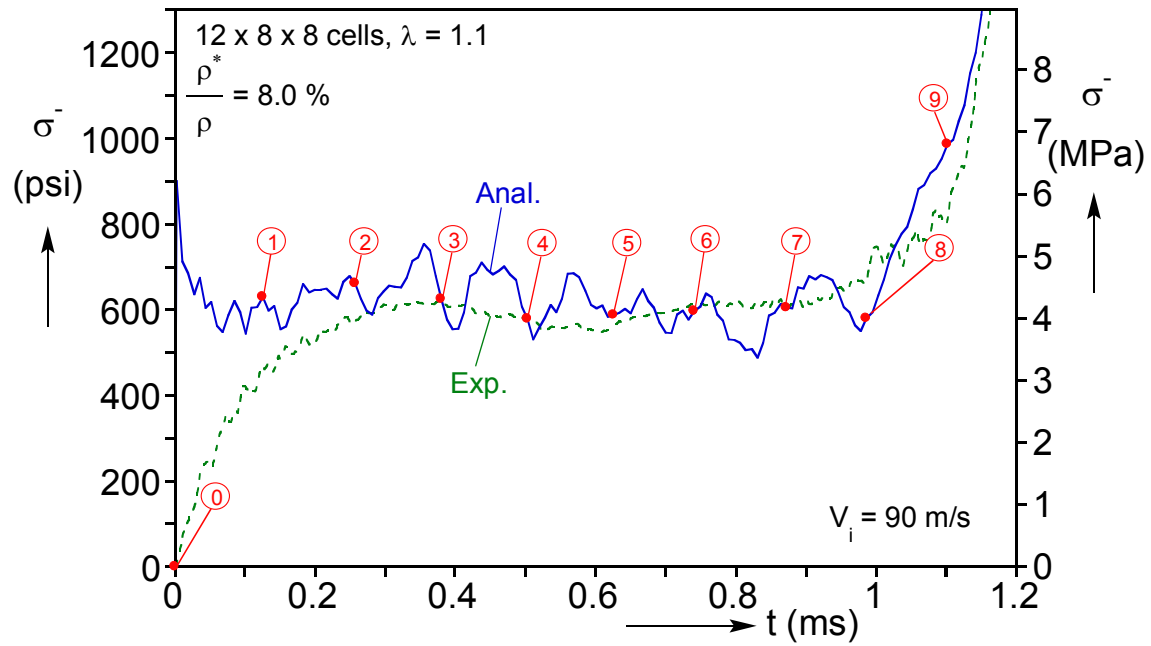
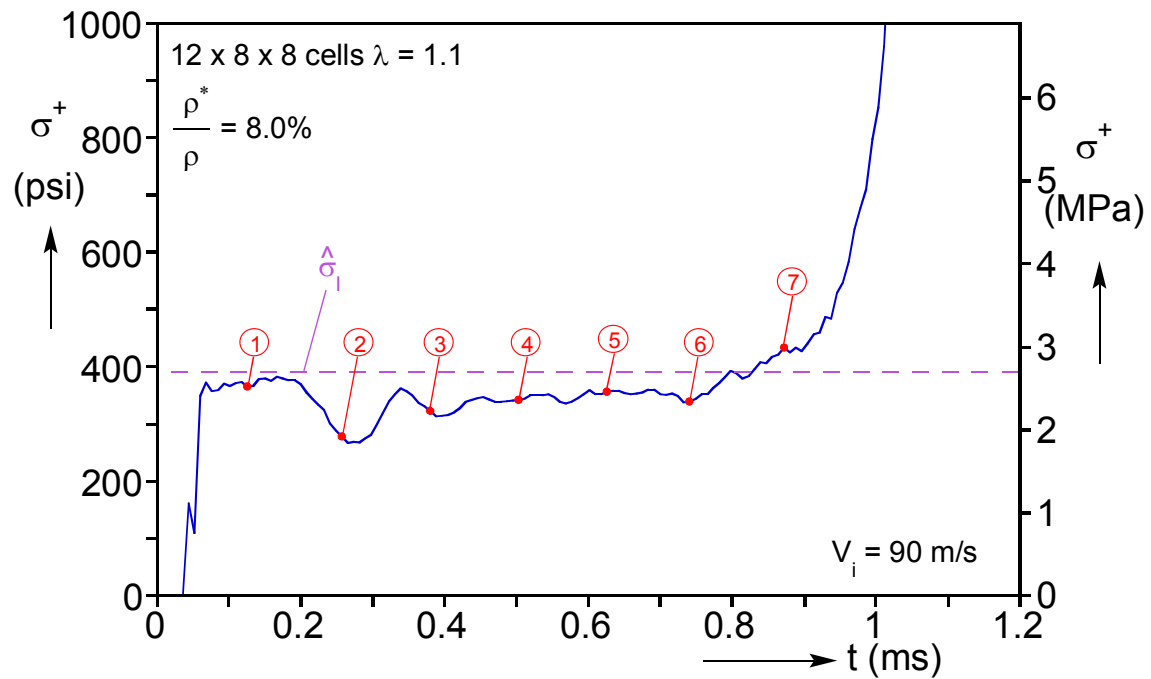


Fig. 5.4 Sequence of deformed configurations corresponding to the numbered bullets on the response in Fig. 5.3.



(a)



(b)

Fig. 5.5 (a) Proximal and (b) distal stress-time histories from a simulation of the 90 m/s direct impact speed experiment.

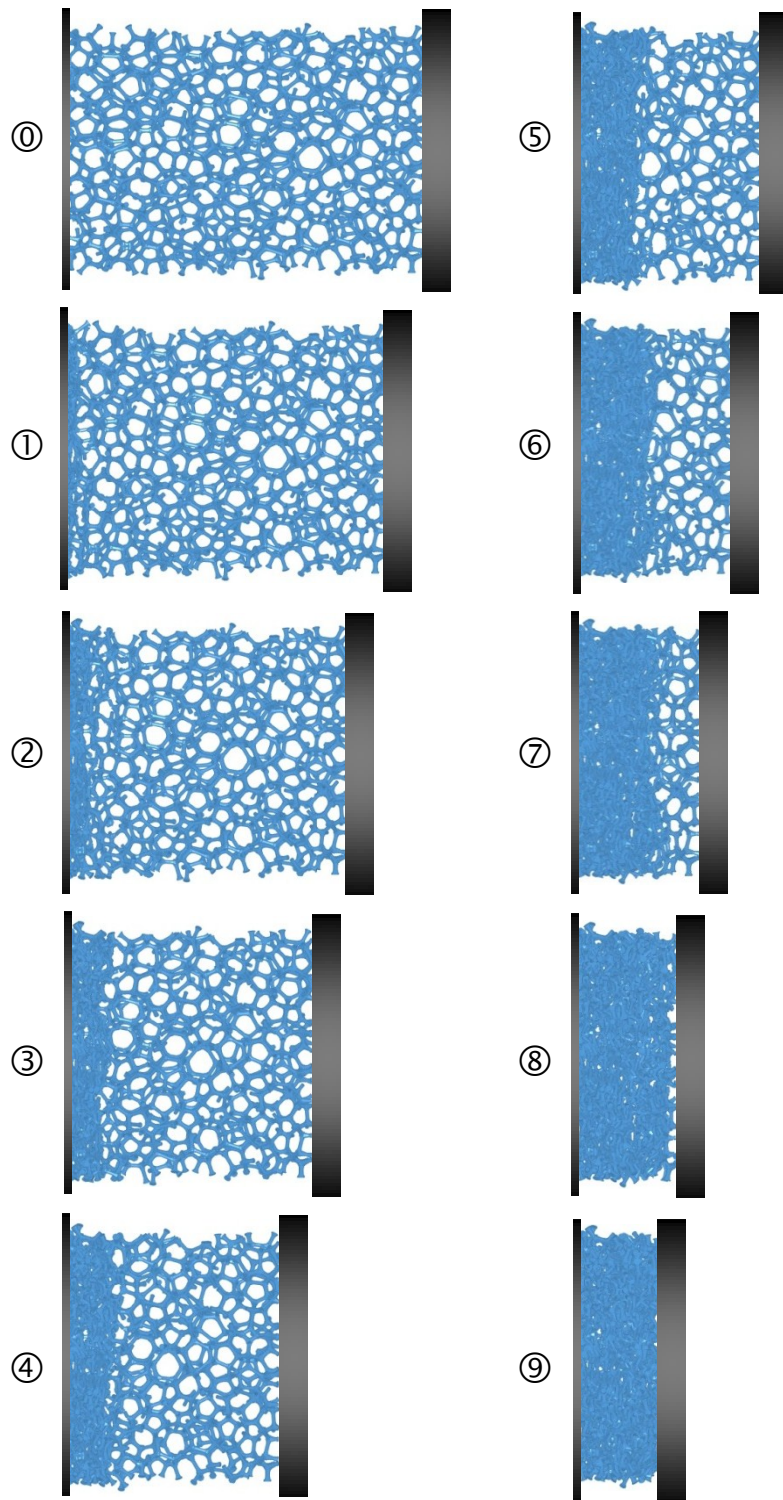


Fig. 5.6 Sequence of deformed configurations corresponding to times marked on the stress histories in Fig. 5.5 with numbered bullets.

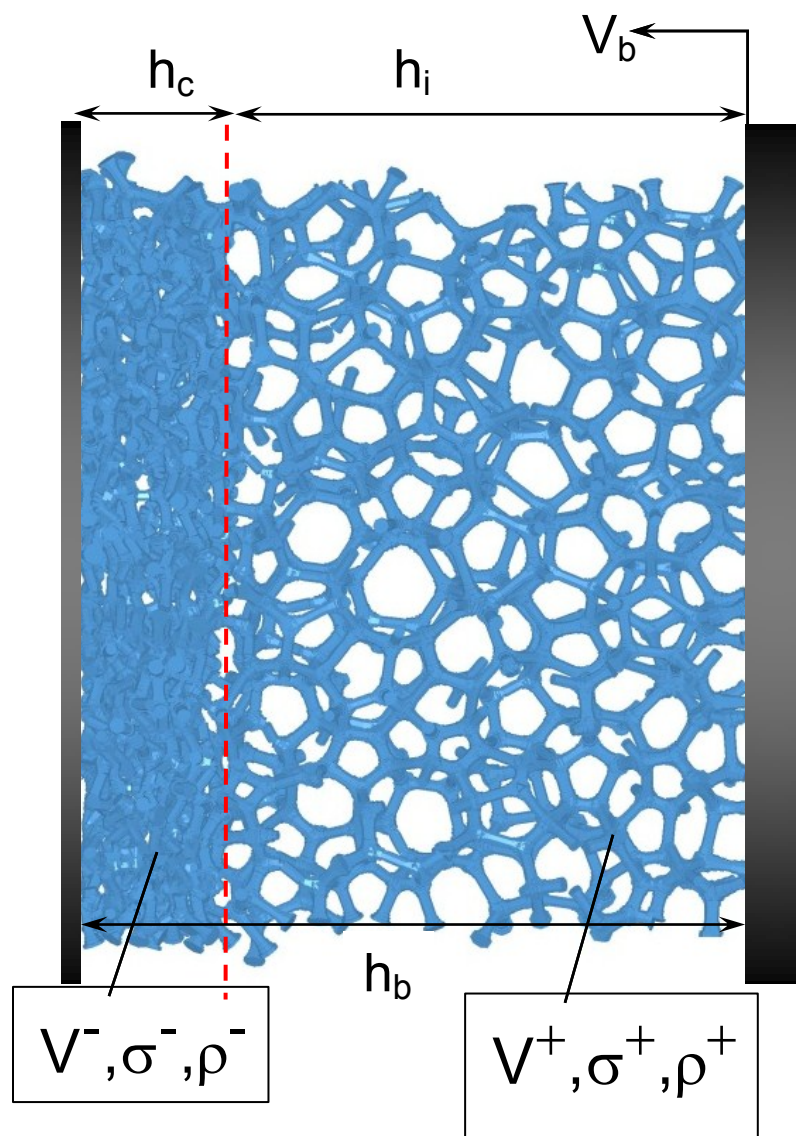


Fig. 5.7 Enlarged view of the model showing the propagating shock.

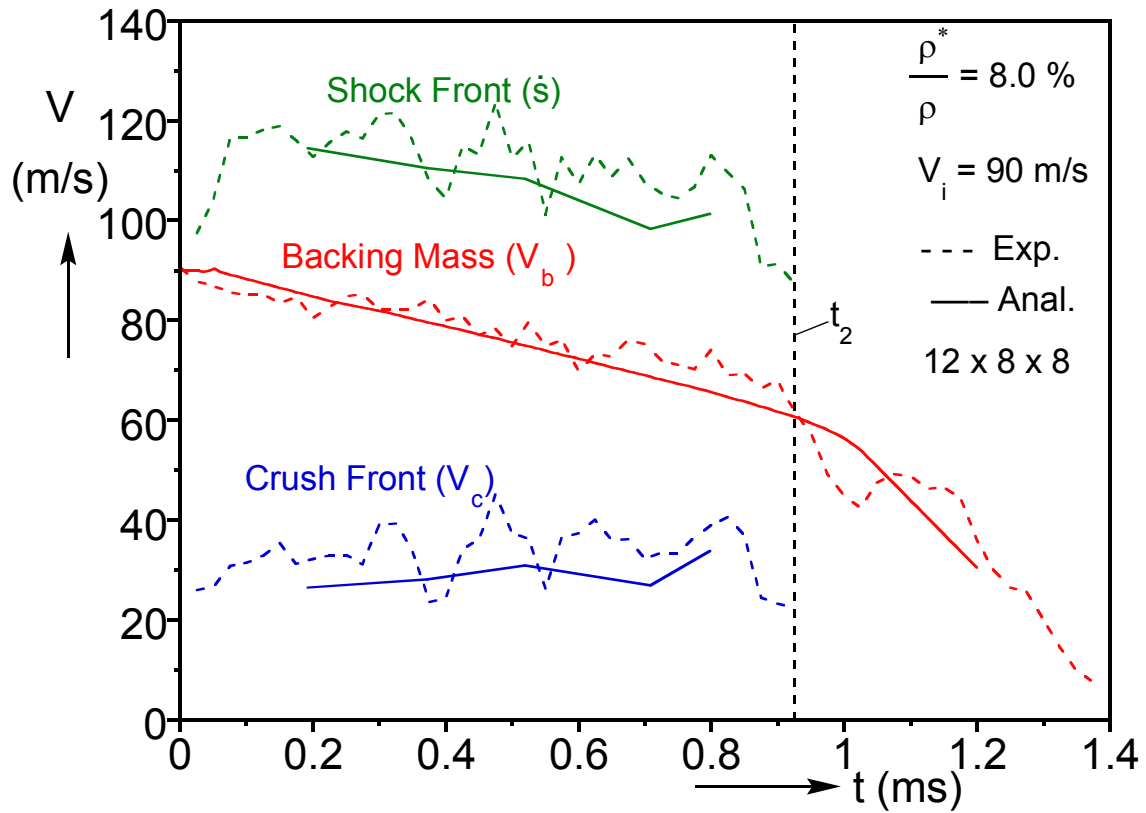
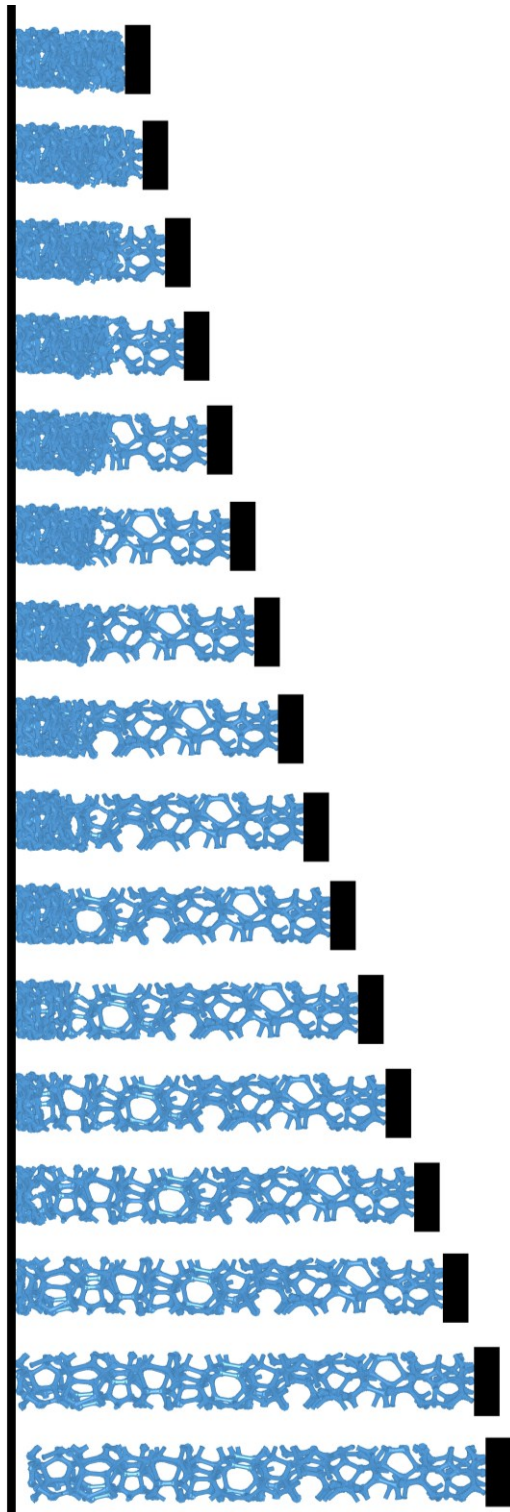
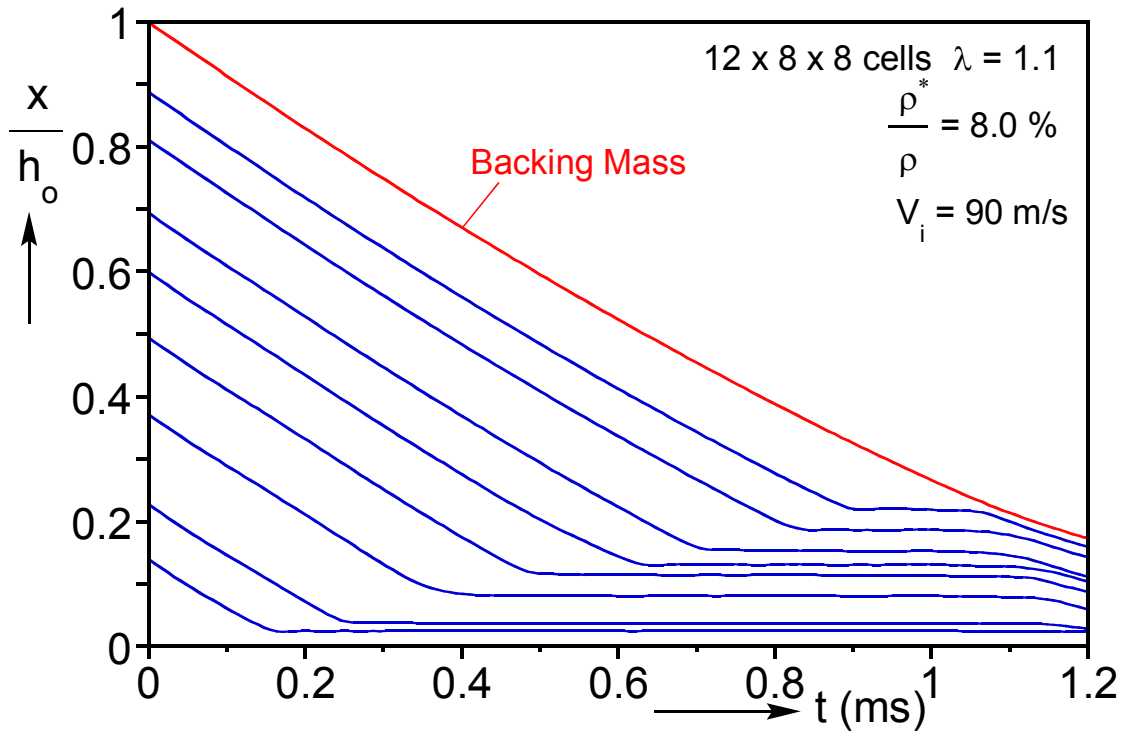


Fig. 5.8 Comparison between measured and calculated velocity-time profiles for the 90 m/s direct impact speed experiment.



(a)



(b)

Fig. 5.9 (a) Position vs. time diagram of a strip extracted from the model. (b) Position vs. time trajectories of several model nodes along the impact direction ($V_i = 90$ m/s).

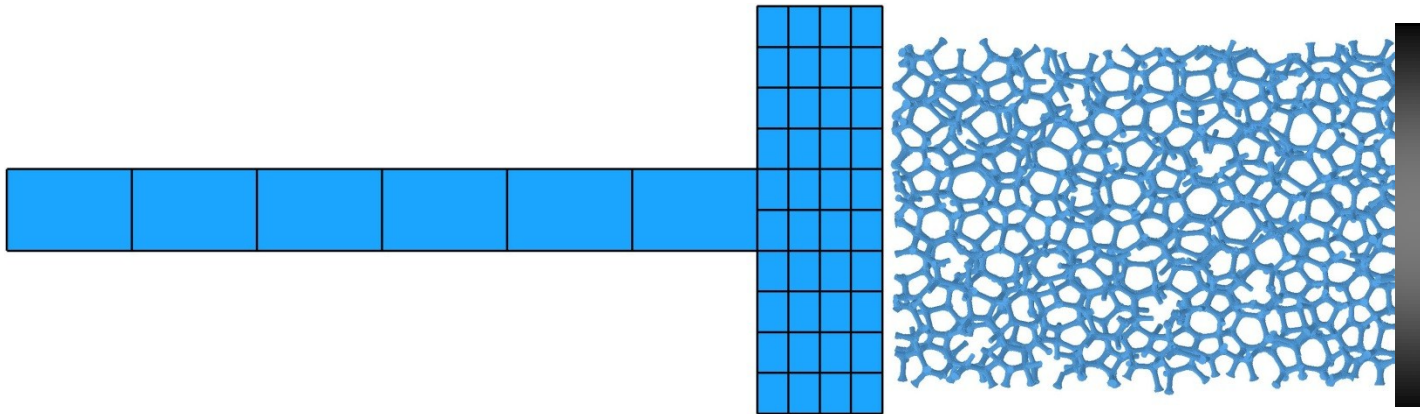
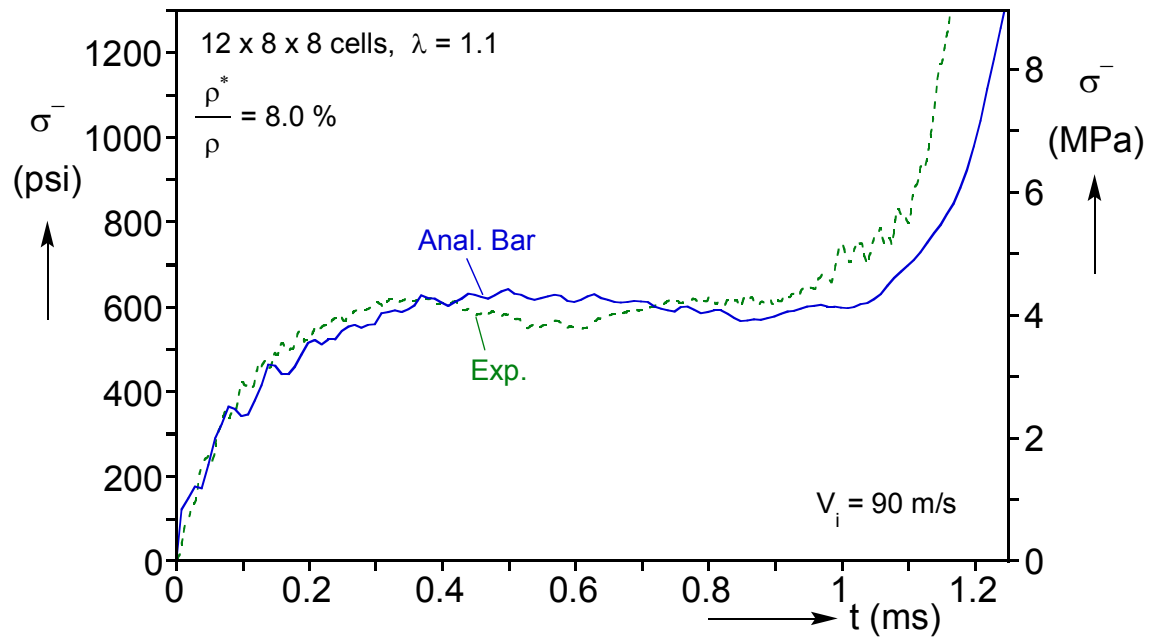
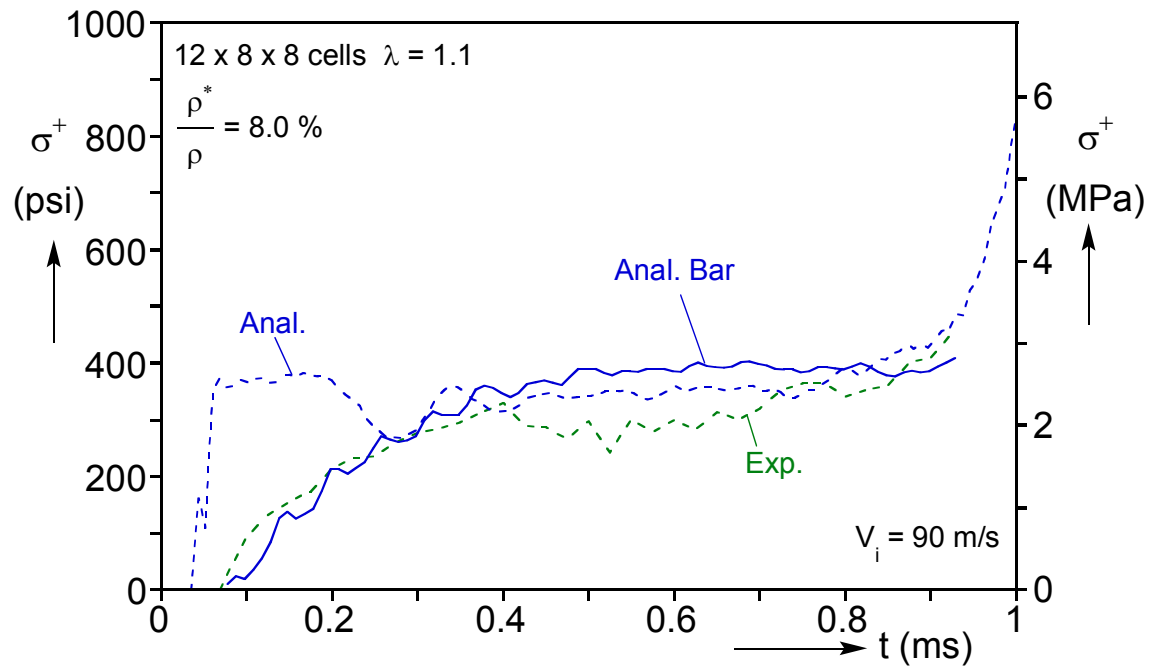


Fig. 5.10 Model showing the foam and the anvil-pressure bar system.

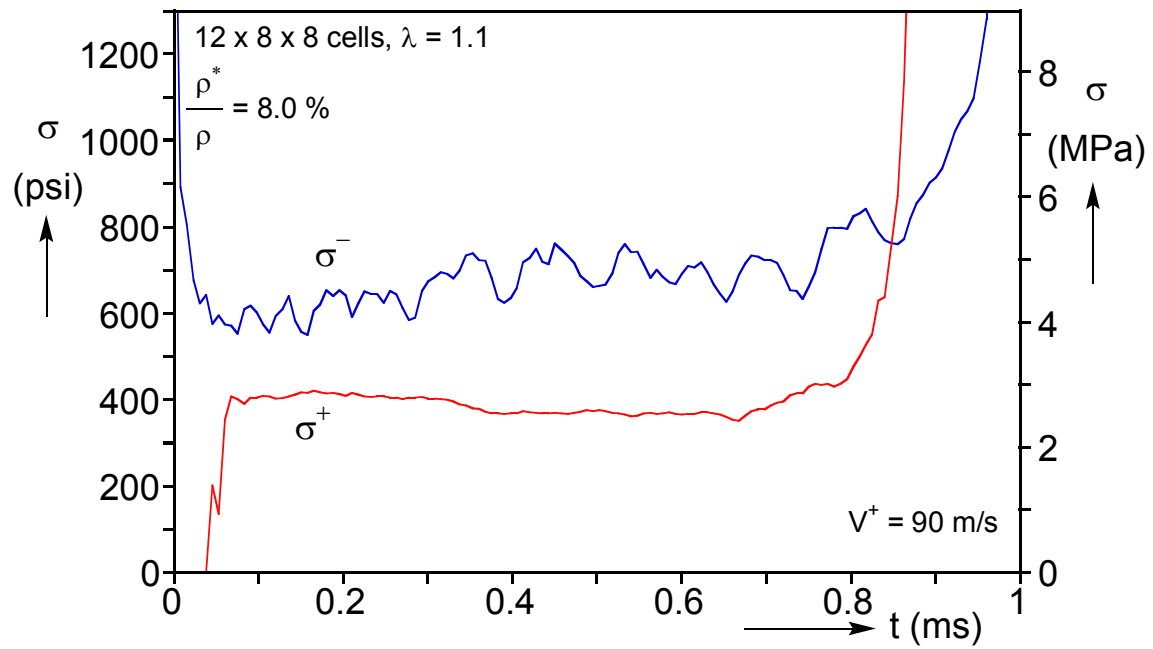


(a)

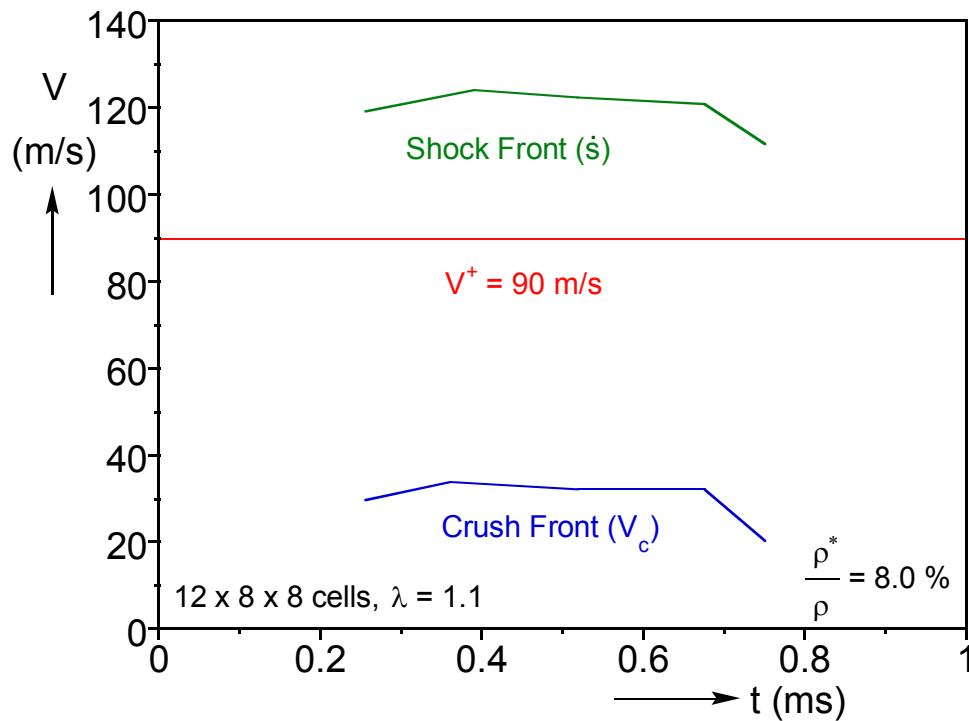


(b)

Fig. 5.11 (a) Proximal and (b) distal stress-time histories from a direct impact simulation that includes the anvil and pressure bar ($V_i = 90$ m/s).

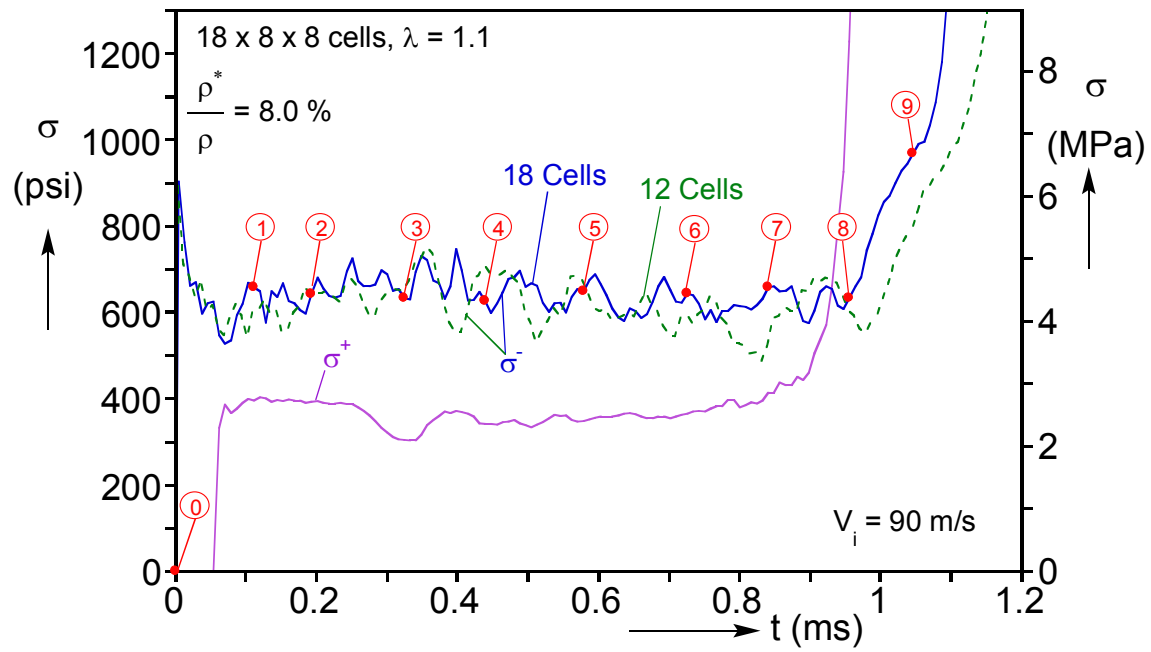


(a)

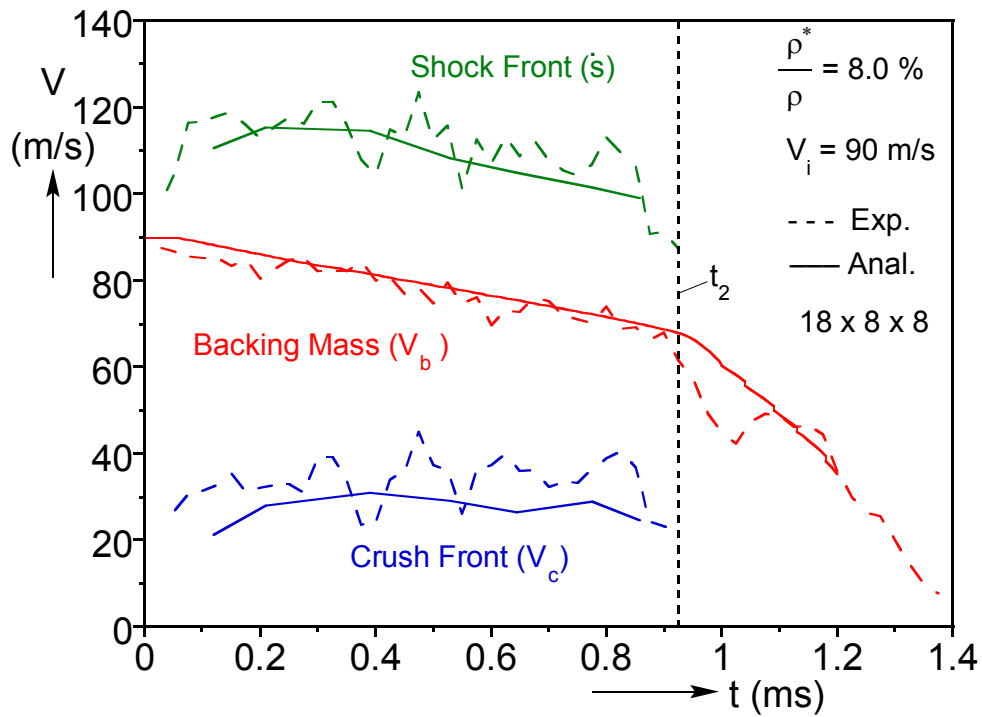


(b)

Fig. 5.12 (a) Proximal and distal stress-time histories from a direct impact simulation with a constant impact velocity of 90 m/s. (b) Velocity-time profiles from the same simulation.



(a)



(b)

Fig. 5.13 (a) Proximal and distal stress-time histories from a direct impact simulation using an $18 \times 8 \times 8$ cell model ($V_i = 90$ m/s). (b) Velocity-time profiles from the same simulation and the corresponding measured ones.

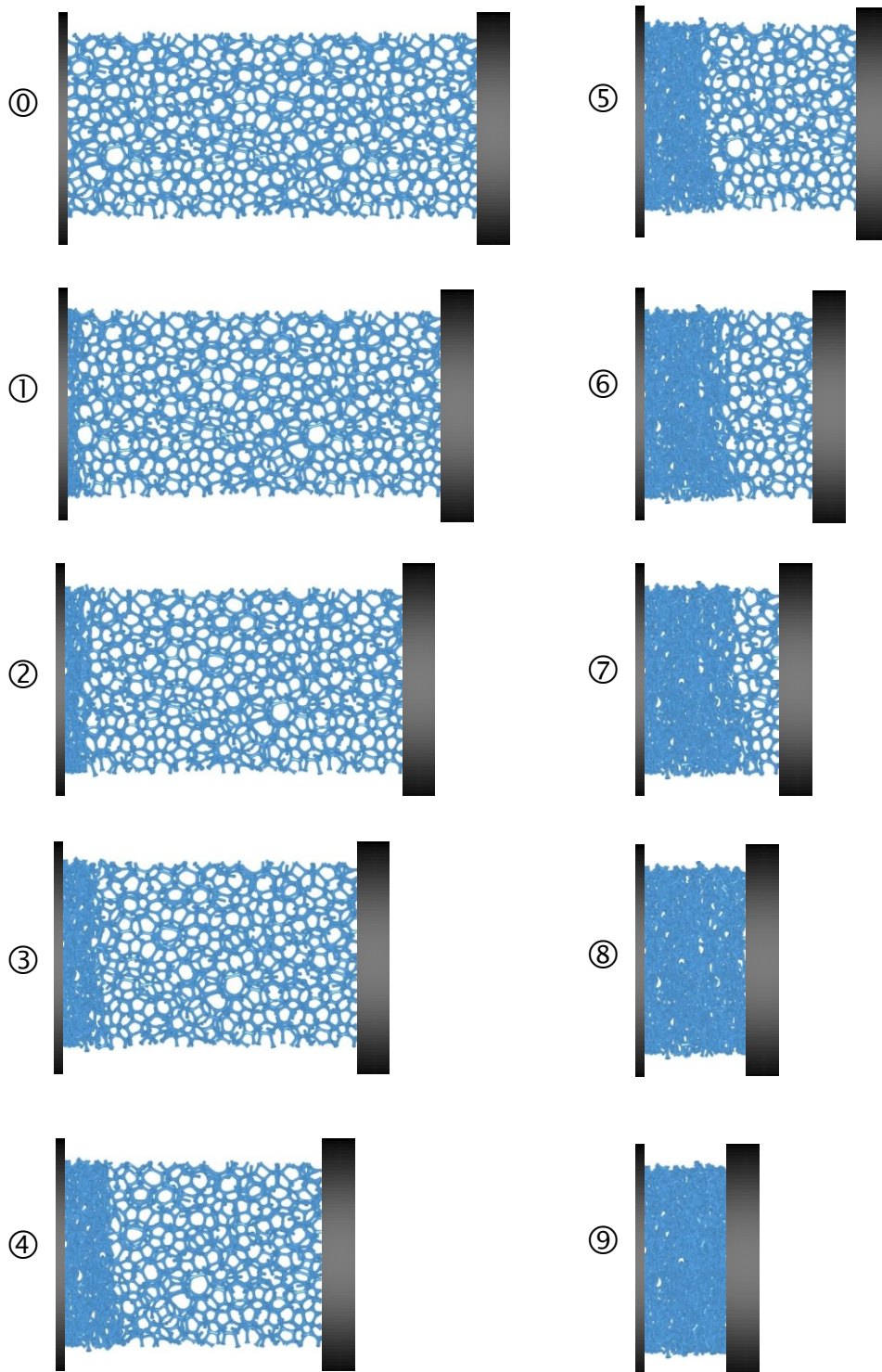
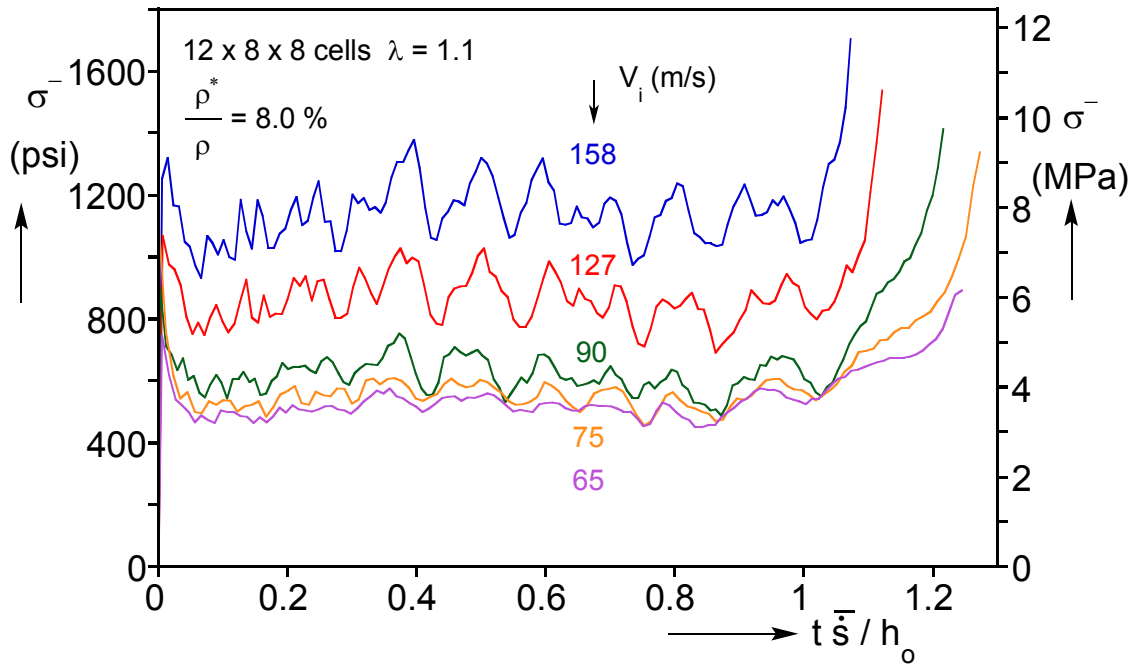
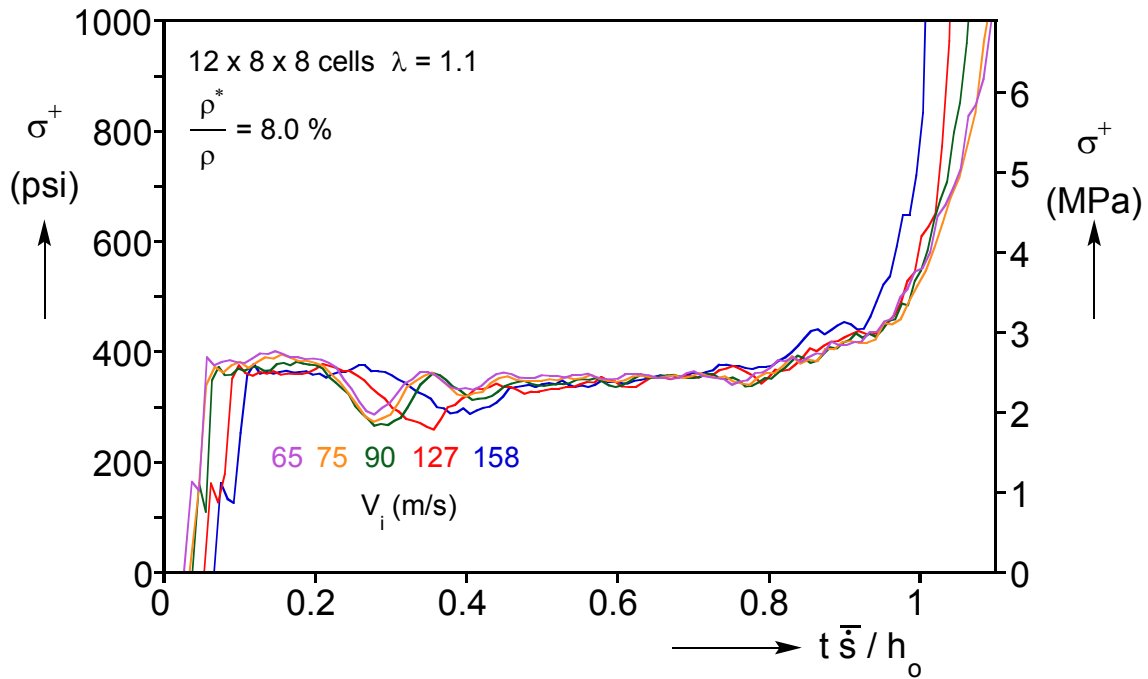


Fig. 5.14 Sequence of deformed configurations corresponding to times marked on the stress history in Fig. 5.13 with numbered bullets.



(a)



(b)

Fig. 5.15 (a) Proximal and (b) distal stress-time histories from direct impact simulations at different impact speeds.

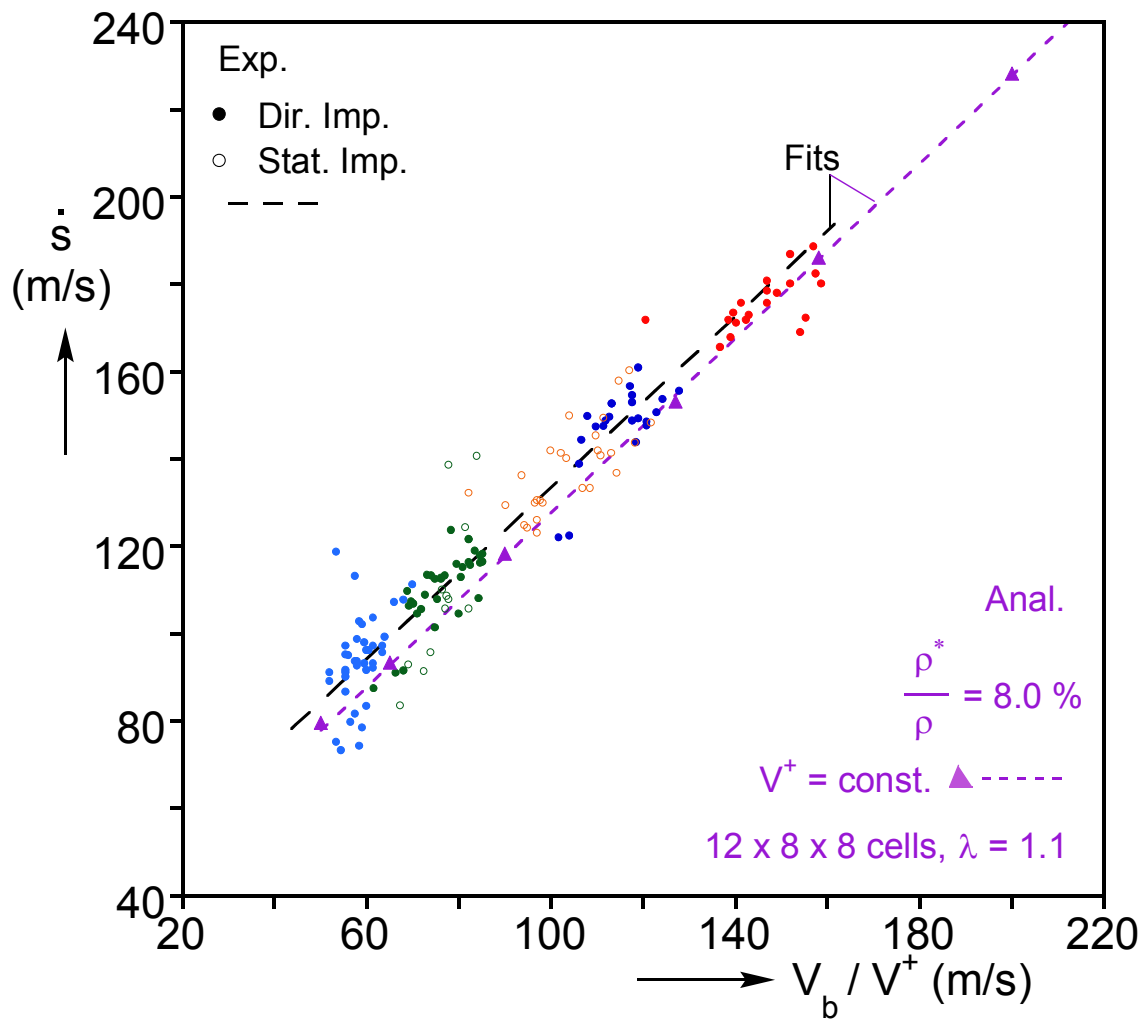


Fig. 5.16 Comparison of experimental and calculated shock speed-backing mass velocity Hugoniot (calculations performed at constant impact speed).

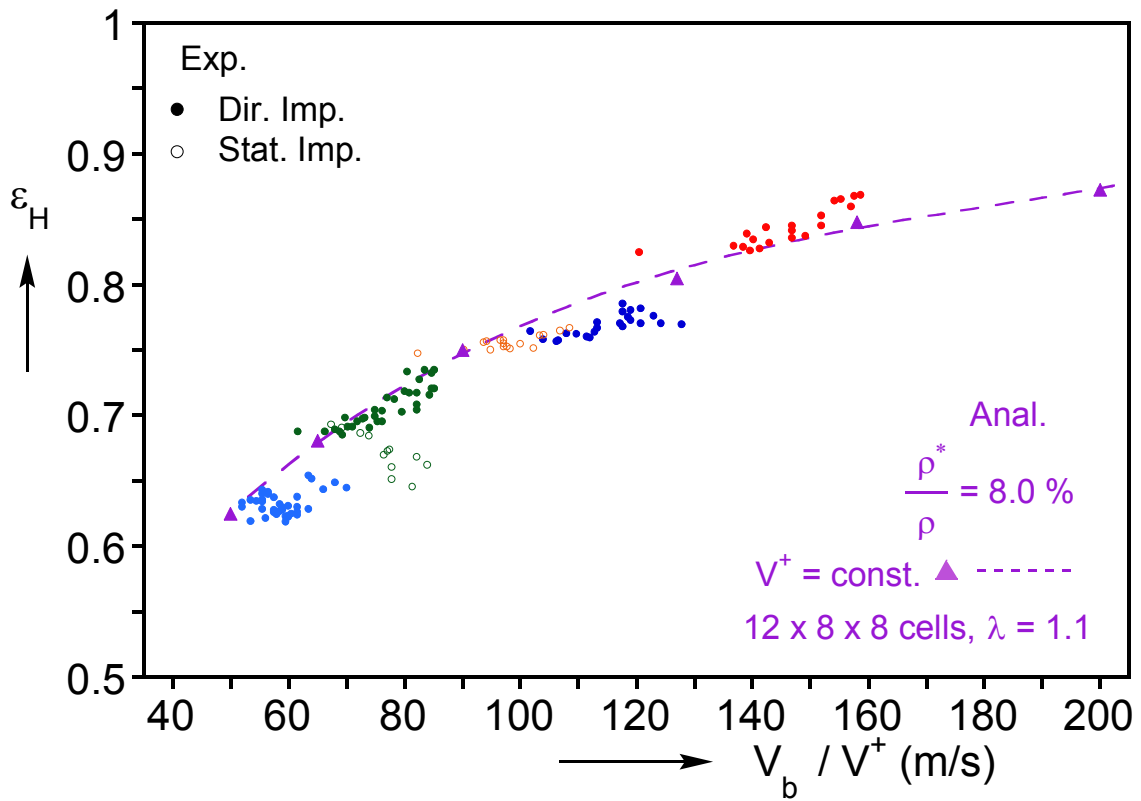


Fig. 5.17 Comparison of experimental and calculated Hugoniot strain-backing mass velocity (calculations performed at constant impact speed).

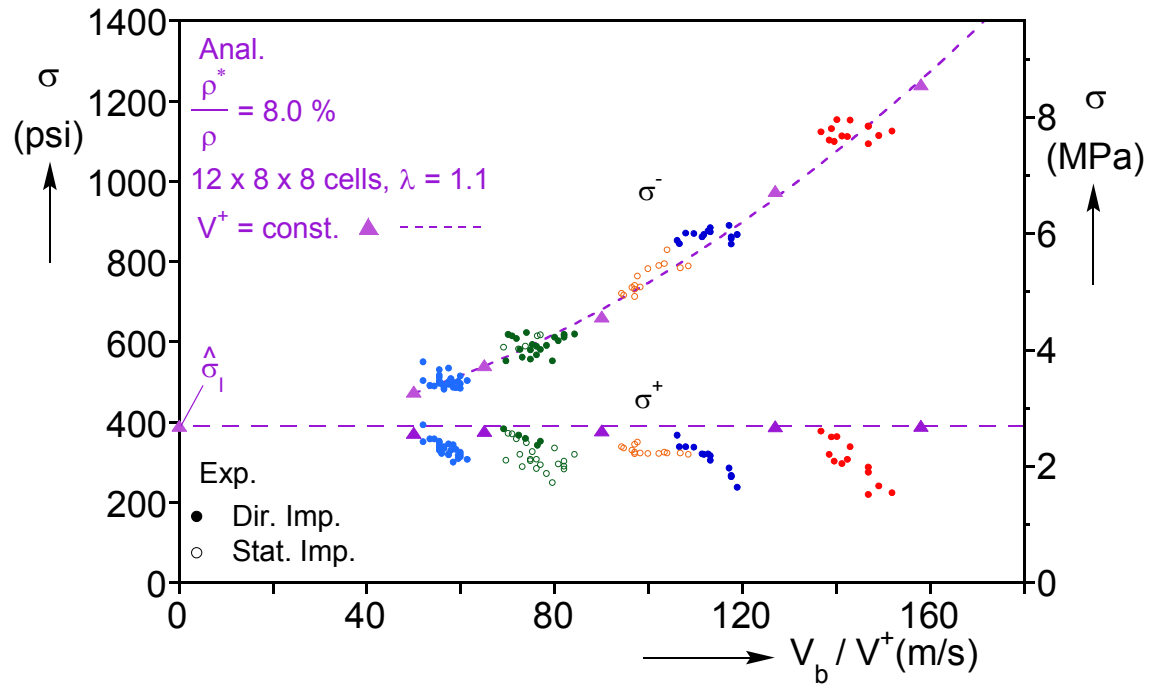
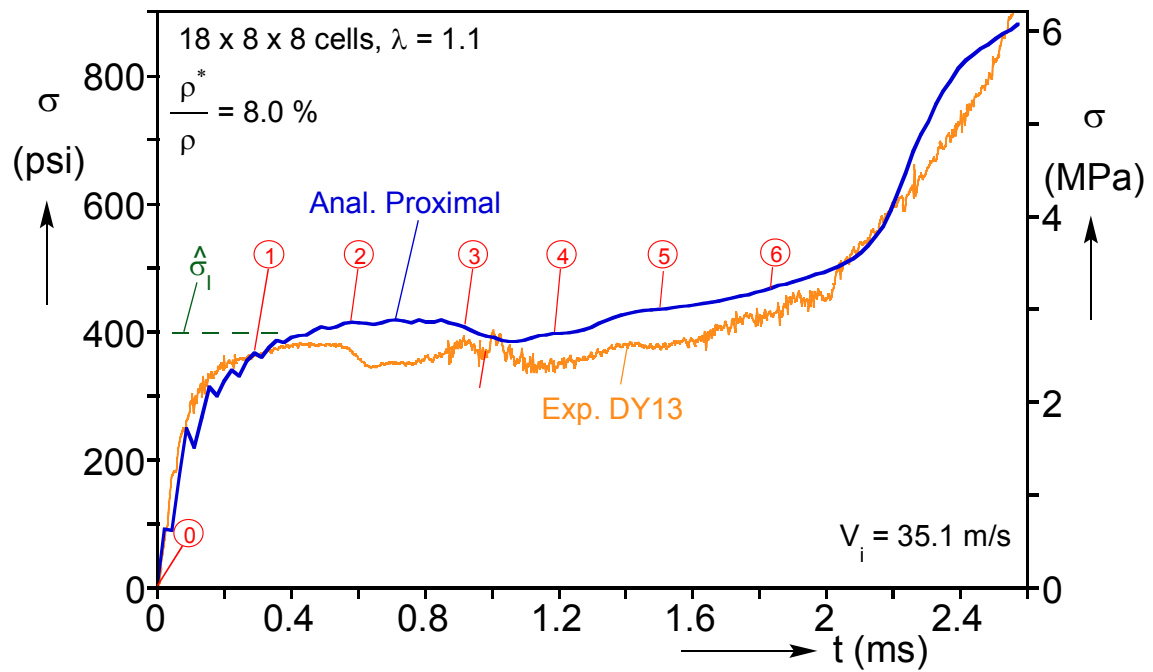
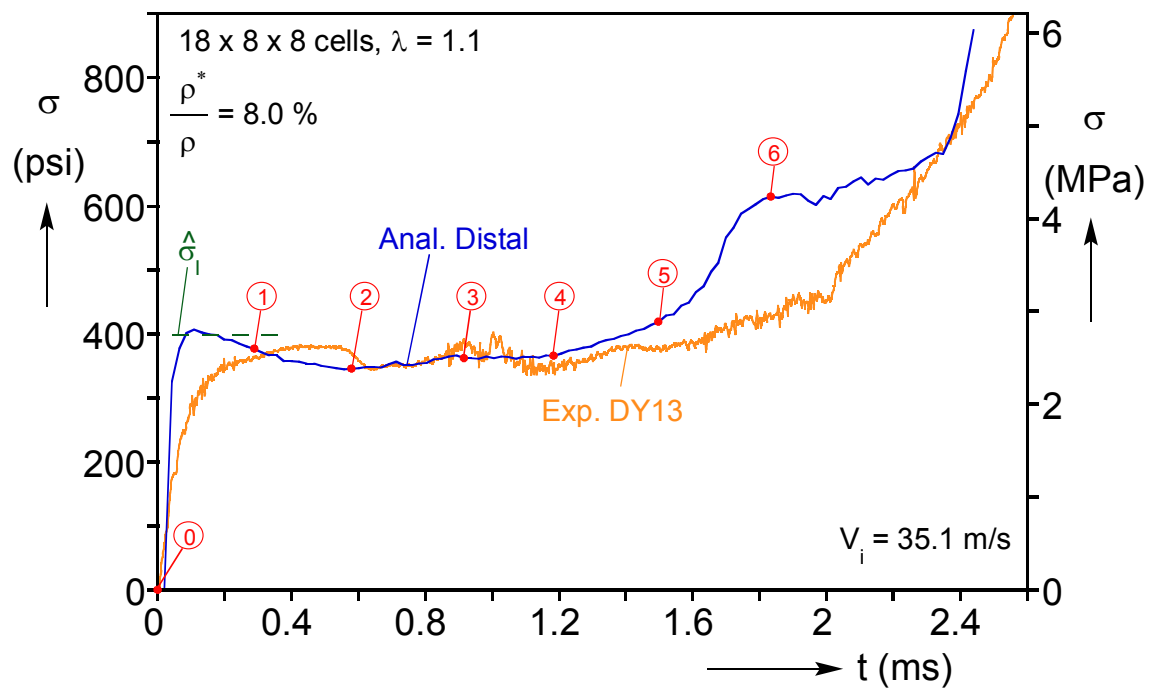


Fig. 5.18 Comparison of experimental and calculated proximal (σ^-) and distal (σ^+) stresses vs. backing mass velocity (calculations performed at constant impact speed).



(a)



(b)

Fig. 5.19 (a) Proximal and (b) distal stress-time histories from a direct impact simulation using an $18 \times 8 \times 8$ cell model ($V_i = 35.1$ m/s).

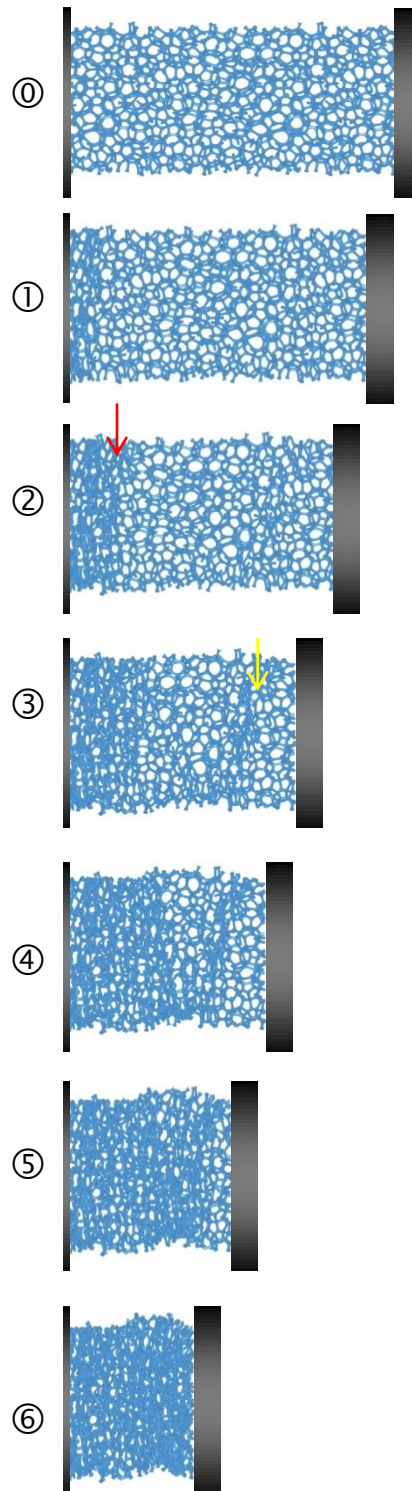


Fig. 5.20 Sequence of deformed configurations corresponding to times marked on the stress histories in Fig. 5.19 with numbered bullets.

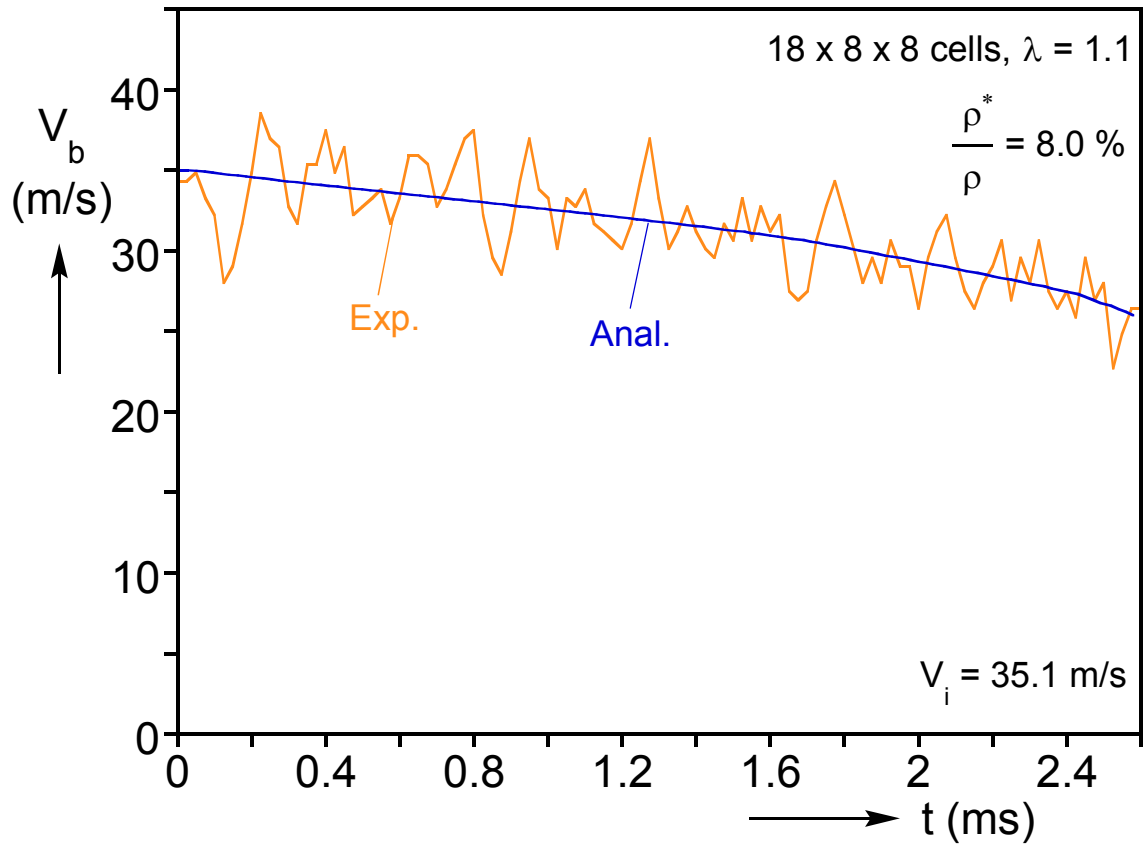
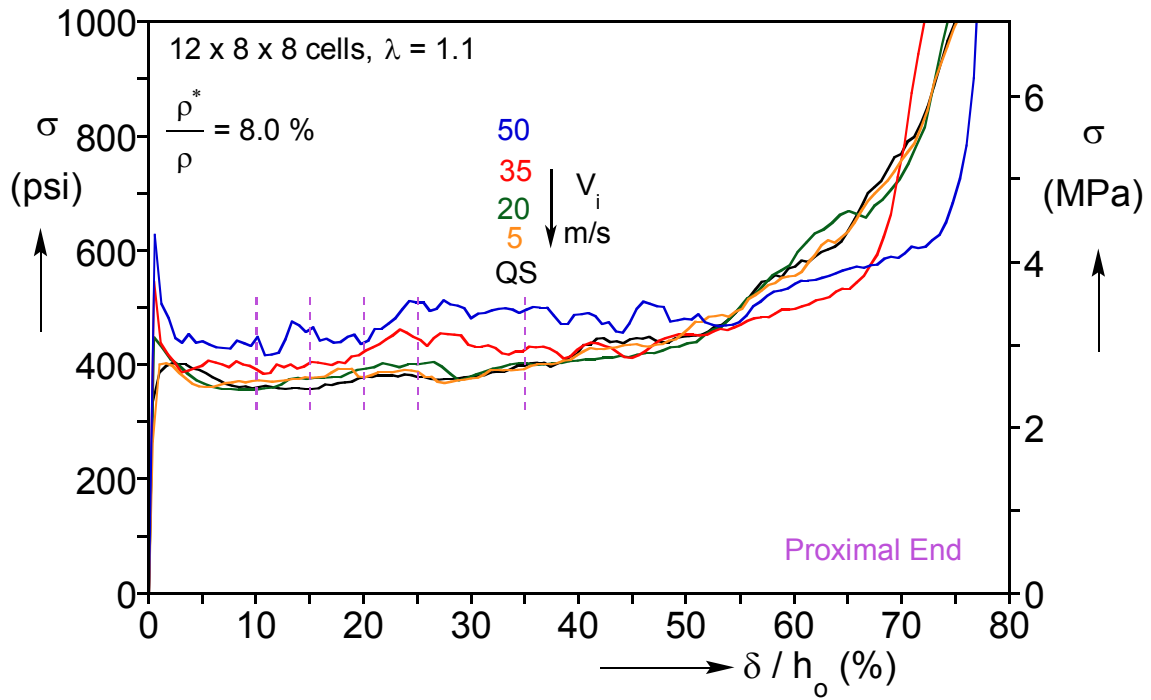
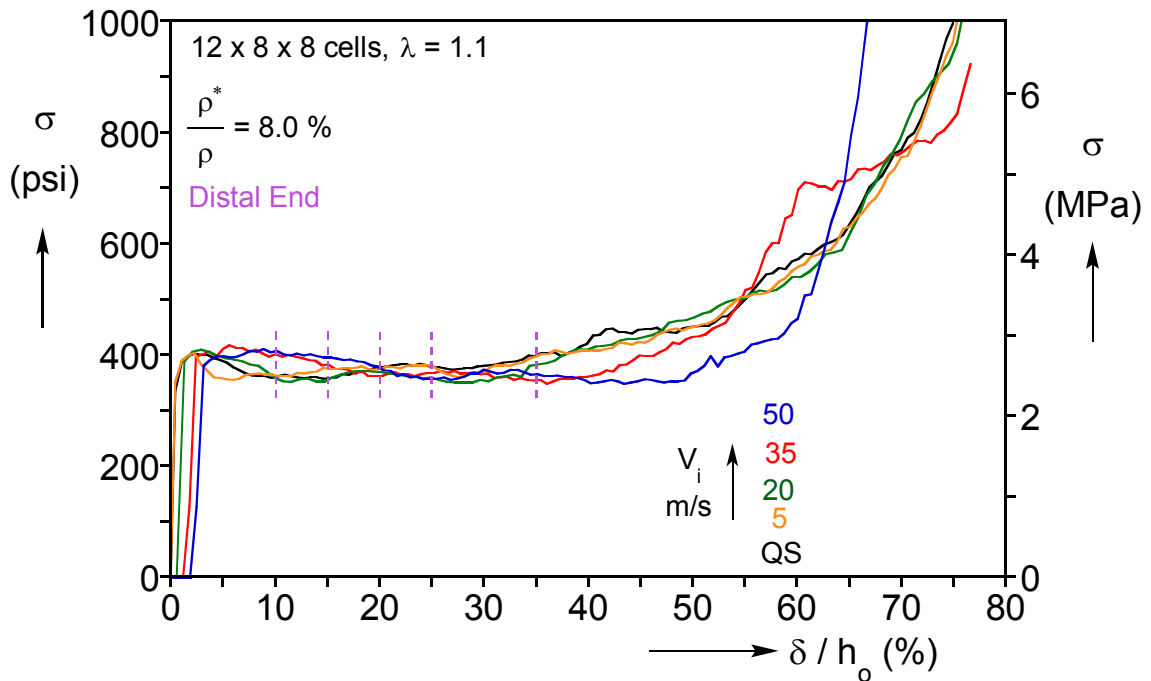


Fig. 5.21 Comparison of measured and calculated backing mass velocities for 35.1 m/s impact speed.



(a)



(b)

Fig. 5.22 (a) Proximal and (b) distal stress-displacement responses from several mainly subcritical constant impact speed calculations using the same 12x8x8 cell model.

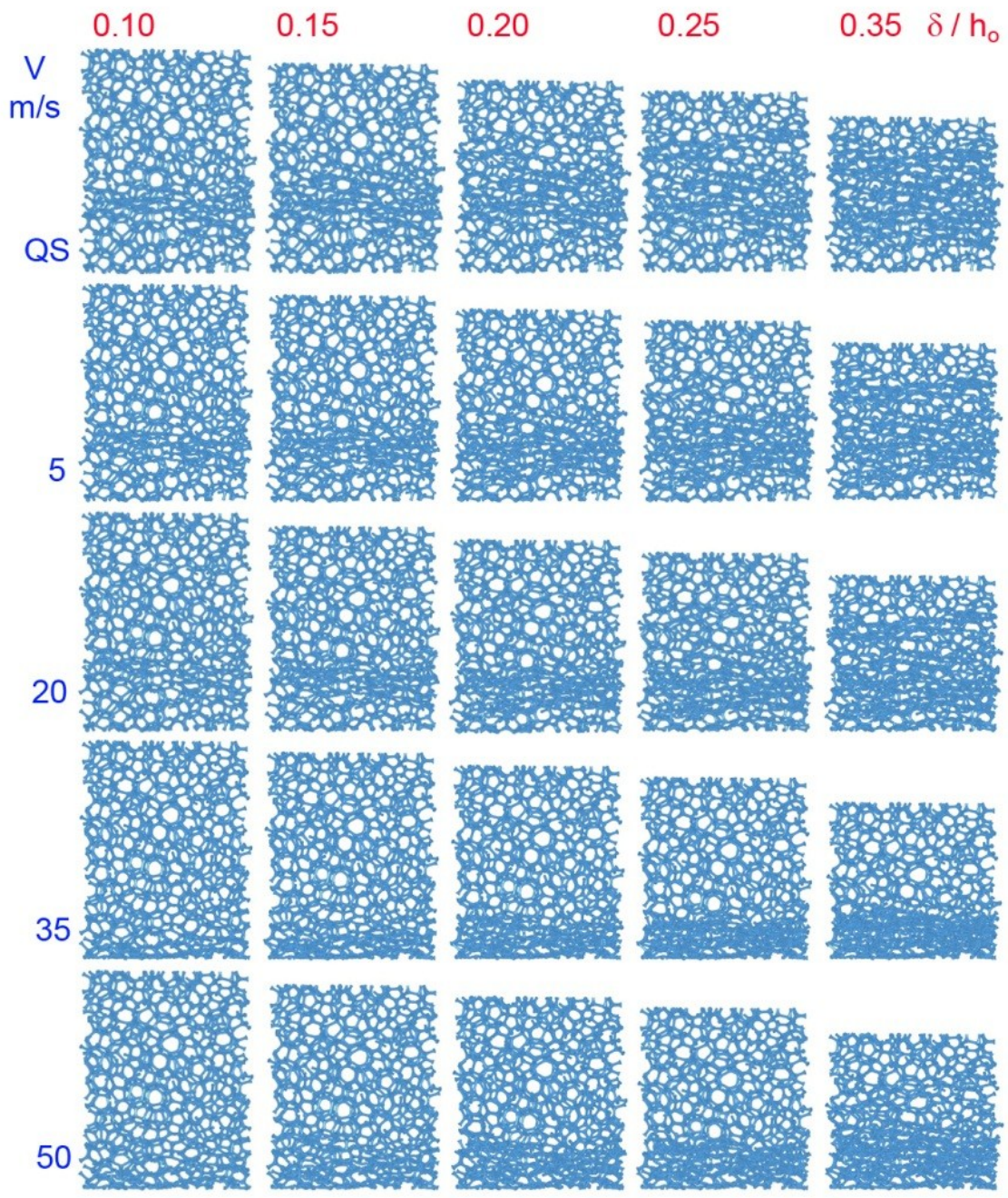


Fig. 5.23 Deformed configurations at the same displacements from several constant impact speed calculations (correspond to responses in Fig. 5.22).

Chapter 6: Foam Density and Energy Absorption

One of the main uses of foams is in impact mitigation and blast protection applications exploiting their excellent energy absorption characteristics. As pointed out in previous chapters, all mechanical properties from the initial elastic behavior to densification are governed by the relative density, the mechanical properties of the base material and the microstructure. In this Chapter we consider open-cell Aluminum foams with a range of relative densities and with the same random microstructure as the ones examined in Chapters 2-5. The foams generated numerically are then crushed first quasi-statically and subsequently dynamically from sub- to super-critical impact speeds in order to establish their energy absorption characteristics. For quasi-static crushing these include the limit and plateau stresses and the extent of the stress plateau. In the shock regime, the parameters include the stresses on either side of the shock, the Hugoniot strain, and the strain energy expended across the shock. In addition, the effect of relative density on the transition from quasi-static to shock behavior is examined.

For all results presented here, a domain that facilitates both quasi-static and dynamic crushing simulations is used. Random soap froth of 12^3 cells is cropped down to $12 \times 10 \times 10$ cells. Anisotropy with a factor $\lambda = 1.1$ as described in §2.2.2 is then applied to the microstructure. For the ERG Duocel® (<http://www.ergaerospace.com>) aluminum foam, manufacturing constraints impose a practical range of relative densities around 3-12%. Following the procedure described in Chapter 2 and Appendix A, we use the *same* random microstructure and construct four different models with relative densities of 3.7, 5.6, 7.8 and 10%.

6.1 Quasi-static Crushing For Varying Density

Each of the four new foam models was crushed quasi-statically in the manner described in Chapter 3. The calculated stress-displacement responses of the four foams are shown in Fig. 6.1a. The responses are qualitatively very similar, all displaying an elastic part, a relatively smooth stress plateau and the densification regime. As expected, the levels of the initiation stress are seen to be increasing with density from about 106 psi for the 3.7% foam to 586 psi for the 10% foam. This is shown in Fig. 6.1b where the initiation and propagation stresses are plotted against relative density. They both appear to trace an approximately linear trajectory that does not pass through the origin. Included in the figure is a least squares linear fit for σ_I ($R^2 = 0.9966$) that gives

$$\frac{\hat{\sigma}_I}{\sigma_y} = 0.0026 \left(\frac{\rho^*}{\rho} \right) - 0.006. \quad (6.1)$$

This is in agreement with results of Jang et al. (2010) but differs from the results of Gibson and Ashby (1997) where no distinction is made between σ_I and σ_P and the relationship is directly proportional to $(\rho^* / \rho)^{3/2}$. This difference is important as these stress values play a pivotal role in the design of foam structures.

Each response terminates into a second stiffening branch i.e., the densification regime. The plateau terminates “earlier” (points identified in Fig. 6.1a as III) as the foam becomes more dense and the response appears to stiffen. Included in Fig. 6.1b are the values of the densification strain for the four foam densities. The densification strain decreases with density but also in a linear manner therefore a least squares fit for this variable is also included in the same figure. The linear fit ($R^2 = 0.9953$) gives

$$\varepsilon_D = 0.7087 - 2.2142 \left(\frac{\rho^*}{\rho} \right). \quad (6.2)$$

For the densification strain Gibson and Ashby (1997) report a linear trend also but with different coefficients, i.e. $\varepsilon_D = 1 - 1.4(\rho^* / \rho)$.

Figure 6.2 shows a sequence of configurations for each of the four foams from sections taken at approximately the center of the domain. Images in the first column show the foam undeformed. One readily notices that ligaments become bulkier as density increases. Images in columns I and II correspond to deformed configurations from all densities at normalized displacements $\bar{\delta}$ equal to 10 and 30% respectively (marked as I and II in Fig. 6.1a). In column I, all foams have localized in the same area and then crushing propagates upwards, forming a second band of collapsed cells that can be seen in images II. One of the effects of increasing density is earlier contact between ligaments of the collapsing cells. This leads to a less compact local crushing which translates into smaller local crushing strain with increasing density. This decrease in crushing strain is more clearly seen in the configurations of column III, where all cells have collapsed and densification initiates. At this stage, the normalized shortening $\bar{\delta}$ is approximately equal to the densification strain ε_D . The height of the foam right before densification initiates varies from $0.37 h_o$ for the 3.7% foam to $0.52 h_o$ for the 10% foam.

The total strain energy density before densification commences is given by:

$$U = \int_0^{\varepsilon_D} \sigma(\varepsilon) d\varepsilon. \quad (6.3)$$

The strain energy density is calculated for the four foams and the results are shown in Fig. 6.3a as a function of relative density. The energy is affected by the increase of the plateau stress and the decrease of the densification strain associated with an increase in

the density. However, since the stress difference is much larger, the strain energy density increases in an approximately linear manner. The specific energy is plotted vs. relative density in Fig. 6.3b. It is interesting to notice that the increase in the specific energy is much smaller than the one in strain energy density. For example, a foam of 5.6% relative density with the same mass as a 10% foam (but different volumes), can absorb almost the same amount of energy but with almost half the limit stress, which in turn is connected to the force transmitted through the foam.

6.2 Direct Impact Simulation for Different Densities

We now use the same four models to investigate the effect of relative density on the dynamic behavior of the foam. Each of the four foams is crushed under direct impact with imposed constant velocity in the manner described in §5.2.4. A 90 m/s velocity is chosen so that impact will lead to shock type crushing for all foams. The effect of density to the transition from quasi-static to shock type crushing will be examined later.

Figures 6.4a and 6.4b show the calculated stress acting on the proximal distal ends respectively for all foams. The qualitative nature of the responses is similar for all densities and with the responses reported in Chapter 5. That is, the stresses behind the shock (σ^-) exhibit a similar initial sharp rise followed by a stress plateau with several undulations, while the stresses ahead of the shock (σ^+) are smoother and each trace a plateau bounded by the corresponding initiation stress $\hat{\sigma}_I$. It is also clear from Figs. 6.4a and 6.4b that both stresses behind and ahead of the shock increase significantly with relative density. This increase though is not of the same magnitude; the difference for example between the stress levels for the foams with 8% and 10% relative density are about 300 psi for σ^- and 200 psi for σ^+ . This difference can be explained using the jump condition for the stresses derived from the conservation of linear momentum:

$$\sigma^- = \sigma^+ + \rho_o \dot{s} V = \sigma^+ + \rho_o \frac{V^2}{\varepsilon_H} \quad (6.4)$$

Included in Fig. 6.4b are the corresponding quasi-static initiation stresses. As reported in §4.2.2 and §5.3 σ^+ follows closely σ_I and is independent of the crushing velocity. Therefore, this stress increases with relative density in the same way as shown in Fig. 6.1b for $\hat{\sigma}_I$. The stress σ^- behind the shock is also influenced by ρ_o and \dot{s} or ε_H , as they are connected through the relationship $\dot{s}\varepsilon_H = V$. From Figs. 6.4a and 6.4b it is obvious that the more dense foams crush faster and their stresses pick up earlier. This means that \dot{s} is increasing with density while ε_H decreases (a result somewhat expected from the similar trend of ε_D).

The effect of relative density on the shock velocity and the Hugoniot strain can be seen more clearly with help of the deformed configurations shown in Fig. 6.5. In the first column the foam is again undeformed. Images I show the early formation of shocks at the corresponding impact planes. Images in column II depict the shock propagating towards the moving plane. It is obvious from these images that the shock moves faster as density is increasing, which is also attributed to the higher local compaction that less dense foams can achieve. The smaller compaction is more clearly seen in images III which correspond to the time that all cells have collapsed and the foam is about to undergo a second compaction. To summarize, σ^- increases with relative density by (a) the increase of σ^+ ($\sim \sigma_I$) and (b) the increase of the term $\rho_o \dot{s}$ or equivalently of ρ_o / ε_H . The effect of the relative density, through the increase in the stresses and the decrease of the Hugoniot strain, on the total energy expended across the shock is examined in the next section.

6.3 Effect of Relative Density on the Hugoniot

The new random foam model is now used to examine the effect of density on all representations of the Hugoniot. For this purpose, constant velocity direct impact simulations are performed in the range of 50-160 m/s in the manner described in §5.3. Figure 6.6 shows the calculated $V^+ - \dot{s}$ Hugoniot. As expected, its linear trend holds for all densities. Included also with dashed lines are linear best fits of the data. The lines have approximately equal slopes. However, as density increases the curve moves upward since \dot{s} is increasing.

The same simulations were subsequently used to also extract the Hugoniot strain ε_H . Figure 6.7 shows a comparison of the four $V^+ - \varepsilon_H$ Hugoniot curves. The strain follows a similar asymptotic trajectories as that reported in §4.2.2 and §5.3. The smaller compaction that was reported earlier at higher densities, translates the Hugoniot strain curve downwards. It is interesting to note that the difference between the strain curves varied with impact speed but the curves come closer together at higher speeds.

The $\sigma^- - V^+$ and $\sigma^+ - V^+$ Hugoniot representations are shown in Fig. 6.8. The stress behind the shock, σ^- , follows a quadratic increase with velocity for all densities. The trajectories are not parallel as their differences increases with velocity because of the term $\rho_o \dot{s}$ in Eq. (6.4). By contrast, the σ^+ levels are nearly constant for all densities and their separation is approximately the same as the corresponding one of σ_I (levels marked on the ordinate)

The energy expended across the shock Hugoniot can be evaluated from

$$U_o = \rho_o U = \hat{\sigma}_I \varepsilon_H + \frac{1}{2} \rho_o V^2. \quad (6.5)$$

Figure 6.9a shows the strain energy per unit volume-velocity ($U_o - V_b$) representation of the Hugoniot. The results show that the strain energy increases significantly with impact

speed and density. Included in the figure at zero velocity are the calculated energy absorbed under quasi-static crushing. It is noteworthy that the separation between the strain energy density curves increases significantly with impact speed. In Fig. 6.9b the specific energy $U = U_o / \rho_o$ is also plotted vs. velocity. Similar to the case for quasi-static crushing, the energy absorbed per unit mass has a smaller variation with relative density.

6.4 Effect of Density on the Transition to Shock Formation

The last part of this study examines how the velocity at which shock formation commences is affected by the relative density. Observing in Fig. 6.6 that the upward translation of the Hugoniot with relative density is modest, a significant change of the transition velocity is not expected. For this reason, we will compare here the two extreme cases, i.e., results from the foams with 3.7% and 10% relative densities. Several calculated stress-normalized displacement responses for each foam density impacted at different speeds are shown in Figs. 6.10a and 6.10b. The 3.7% foam is seen from Fig. 6.10a to have responses very similar to the quasi-static one for impact velocities up to approximately 15 m/s. When the impact speed is increased to 30 m/s, the response starts to pick up by about 10% implying a different type of collapse mechanism. The same can be inferred for the 10% foam (6.10b) but with an increase in the transition velocity. In this case, velocity up to 25 m/s produces a response that is essentially at the same level as the quasi-static one. The stress increases for impact speed of about 40 m/s and higher. Therefore, it appears that the critical velocity increases by about 10 m/s when the density changes from 3.7% to 10%.

In support of these observations, Fig. 6.11 shows deformed configurations corresponding to a normalized displacement $\bar{\delta}$ of about 10% for all velocities (marked

as I in Figs. 6.10a and 6.10b). The 3.7% density foam, when crushed under a 15 m/s impact velocity, localized at the same location where collapse initiated quasi-statically. By contrast, when impacted at 30 m/s the first cells to collapse are the ones adjacent to the impact plane (and an intermediate regime of crushing behavior as the one described in §5.4 initiates). The same holds for the 10% relative density foam but at higher velocities. Initial localization of quasi-static type occurs for up to 25 m/s impact speed while above 40 m/s collapse initiates at the impact plane.

In summary, an increase in the critical velocity of about 10 m/s is observed between the foams of 3.7% and 10% relative density.

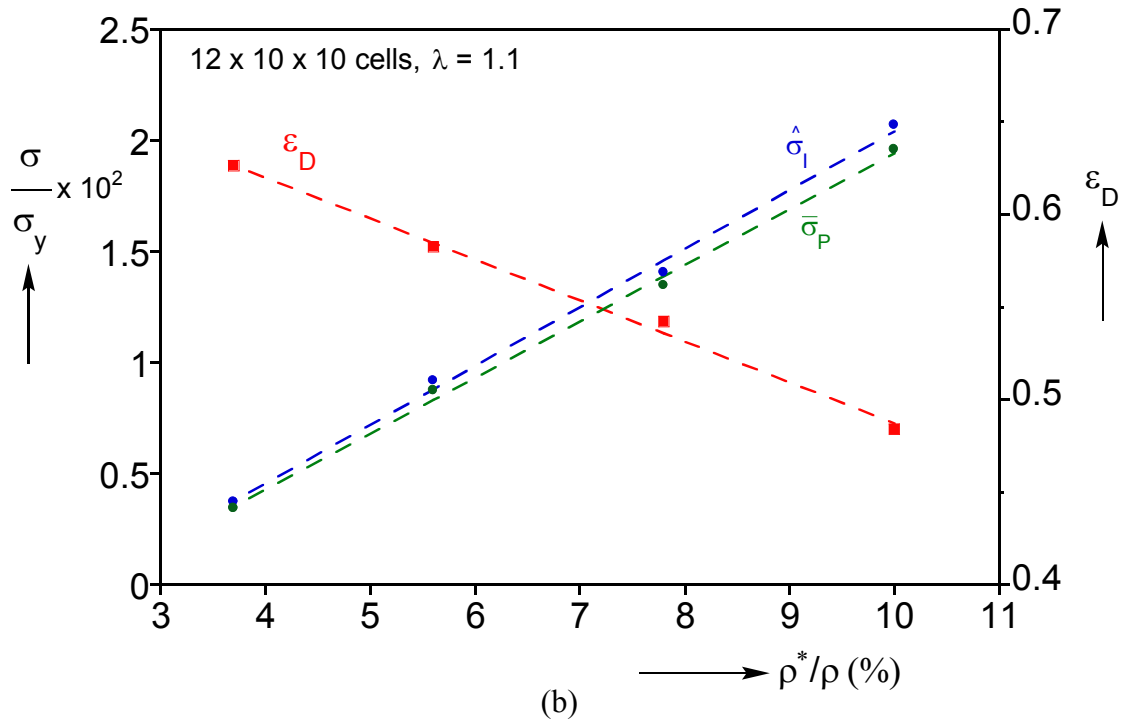
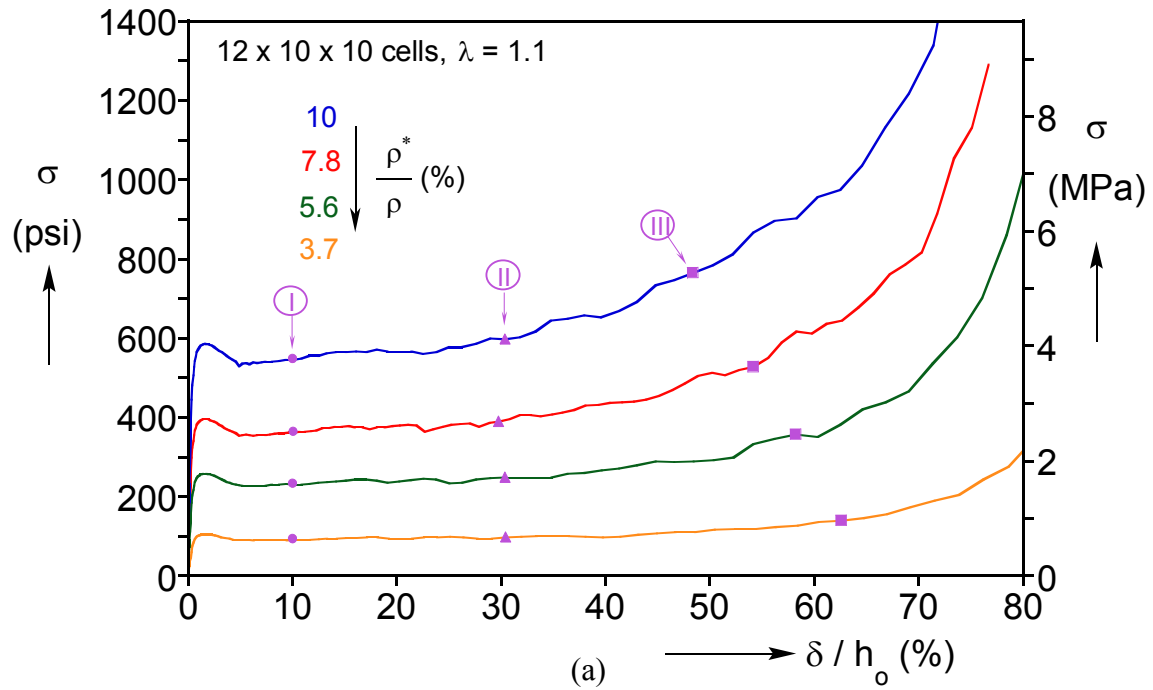


Fig. 6.1 (a) Quasi-static crushing responses for different relative densities. (b) Initiation stress, plateau stress and densification strain vs. relative density.

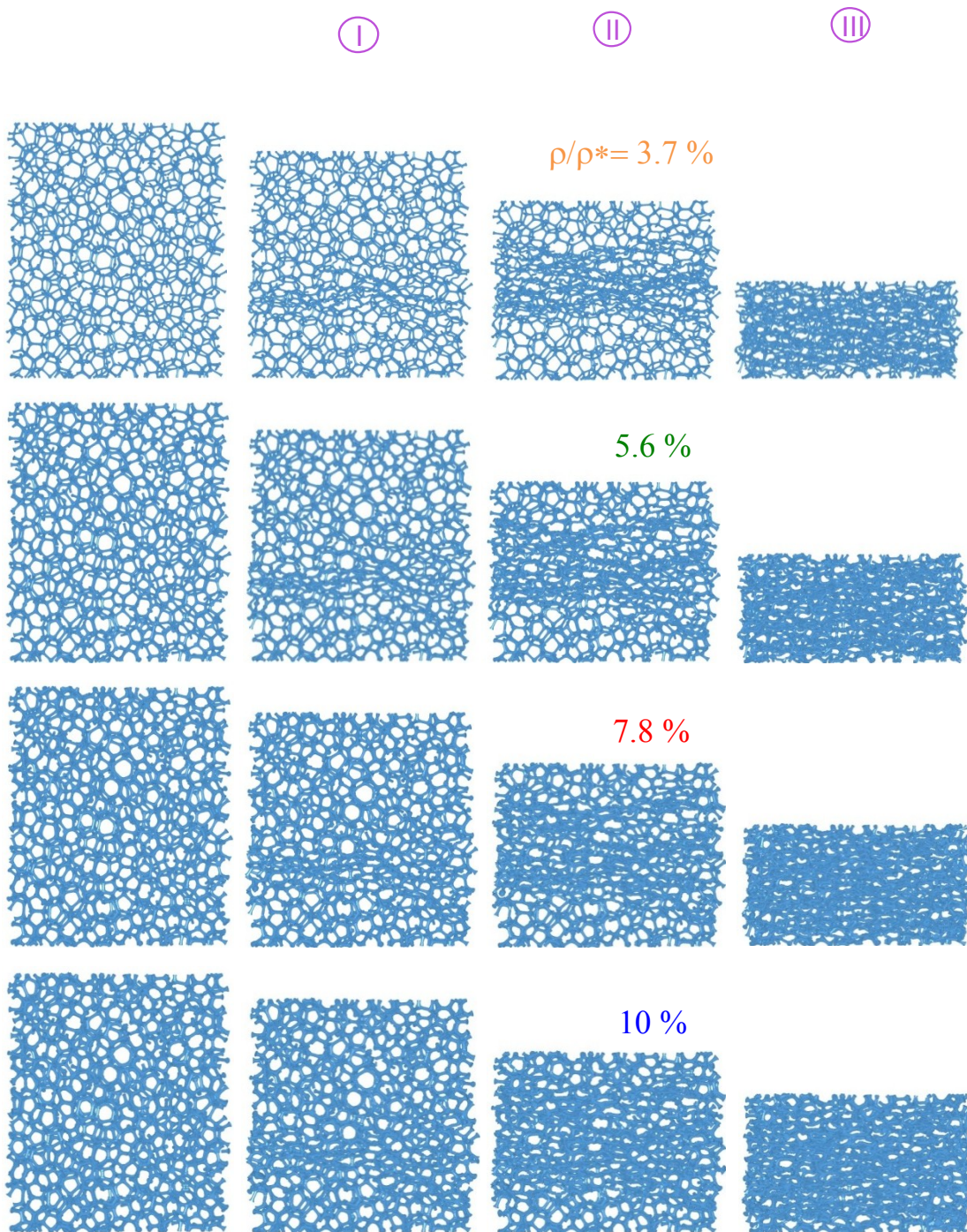
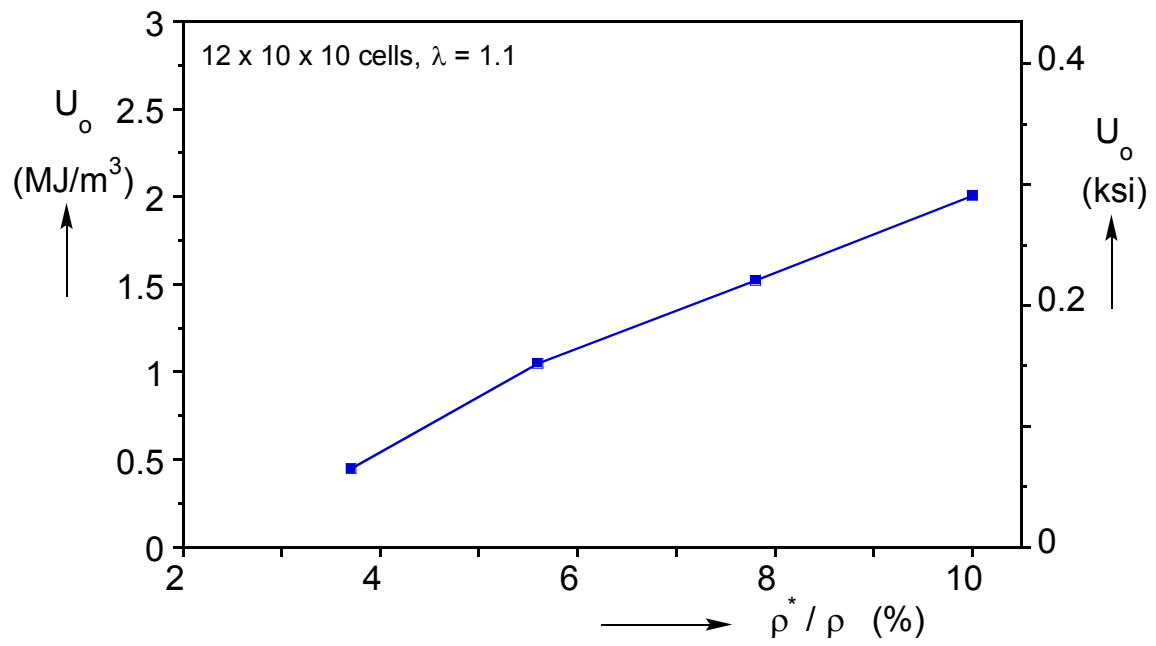
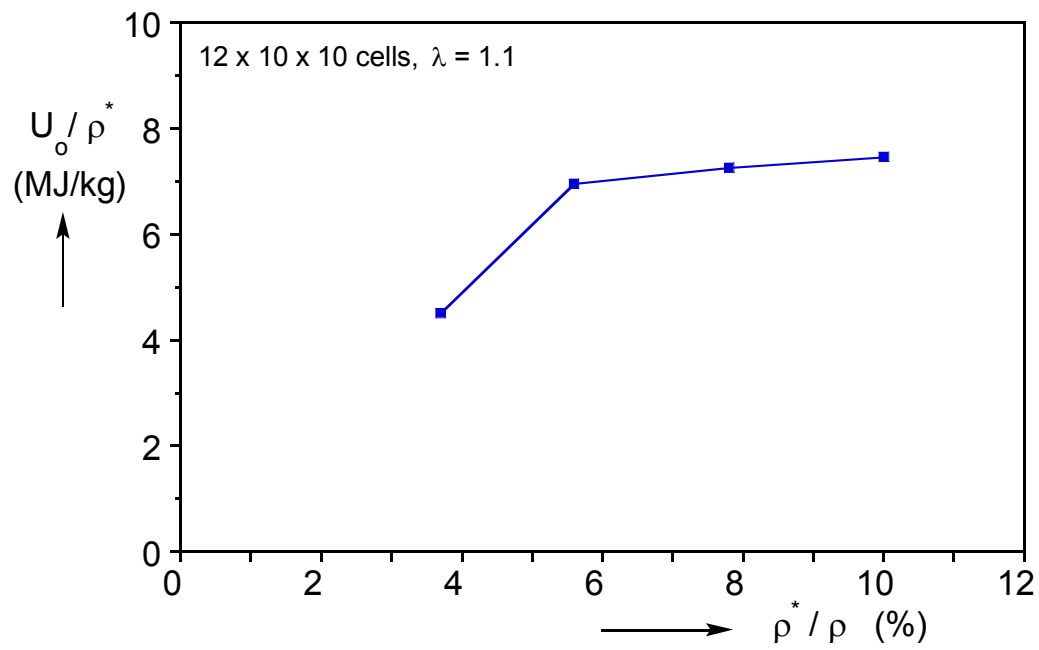


Fig. 6.2 Deformed configurations corresponding to the marked points in Fig. 6.1.

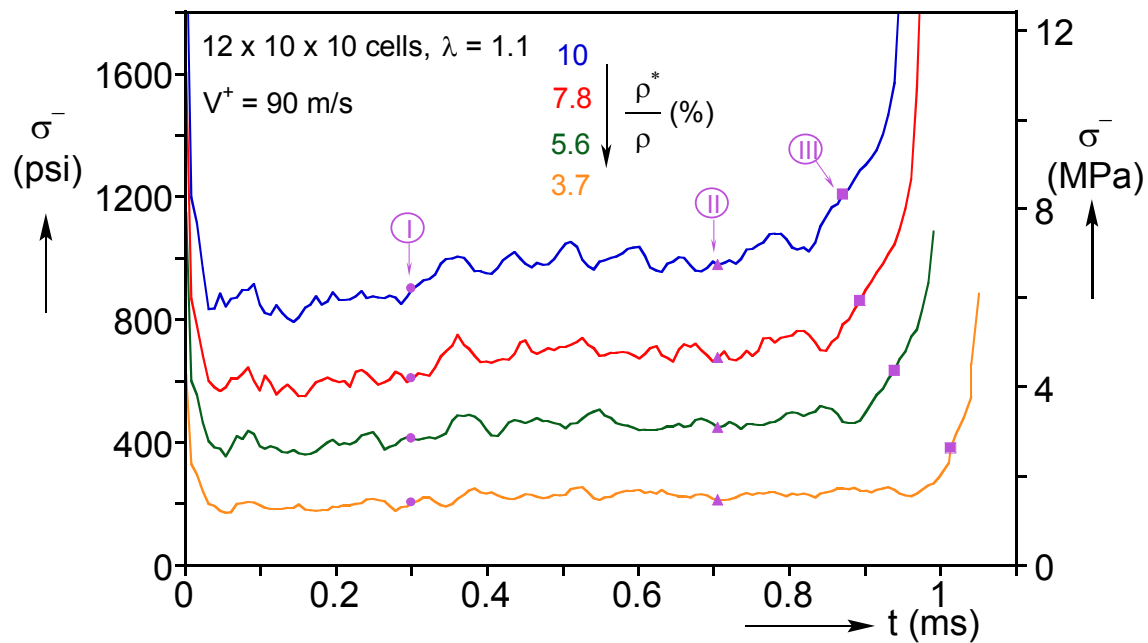


(a)

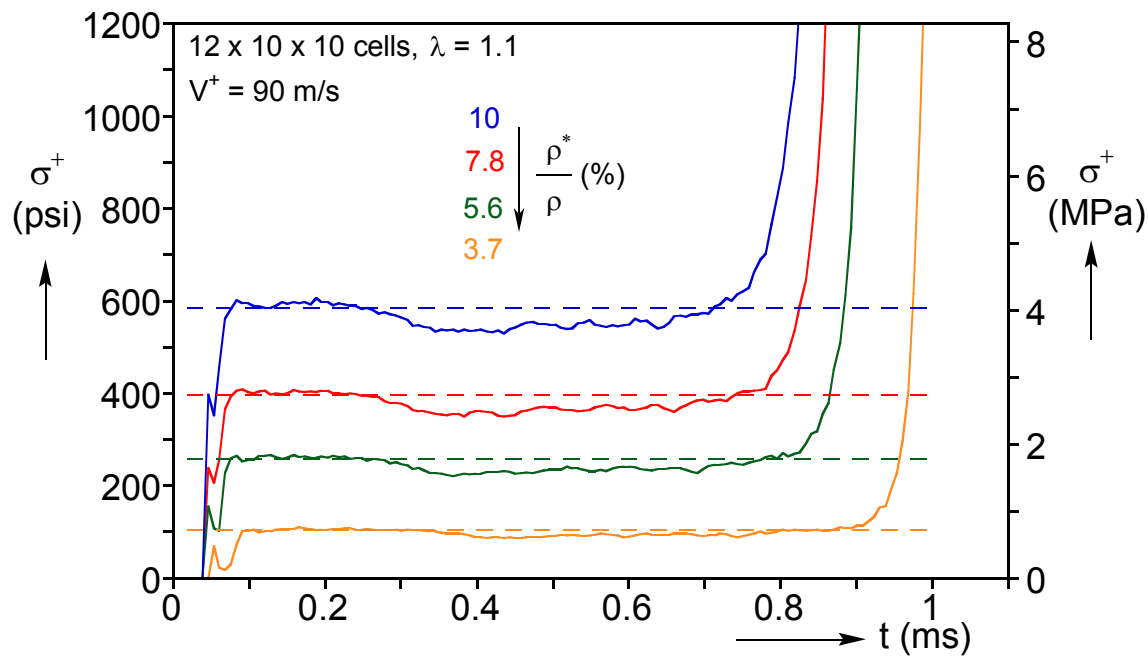


(b)

Fig. 6.3 (a) Strain energy density and (b) specific energy as a function of relative density.



(a)



(b)

Fig. 6.4 (a) Proximal and (b) distal stress-time histories for different densities under constant velocity crushing with 90 m/s.

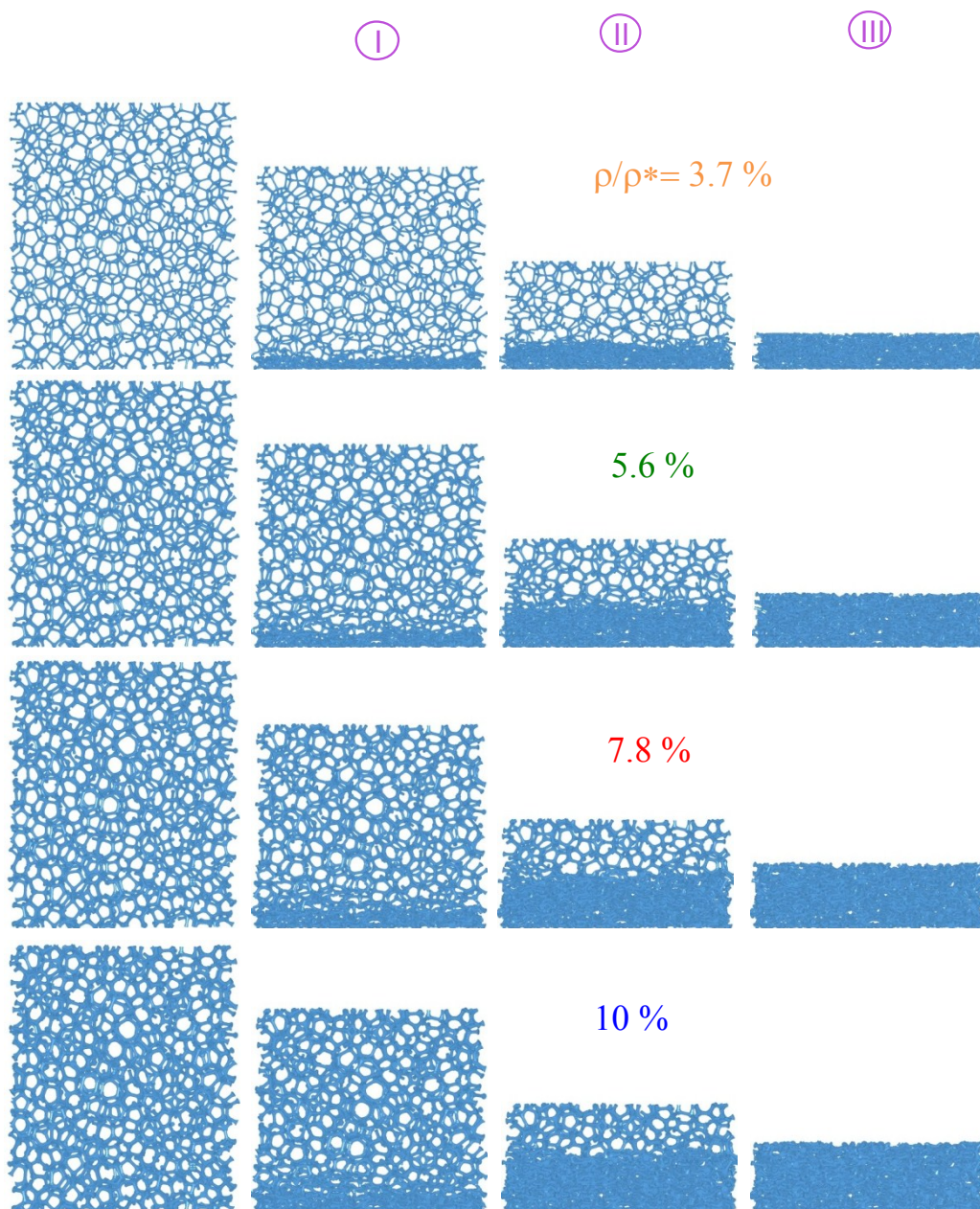


Fig. 6.5 Sequence of deformed configurations corresponding to times marked on the stress histories in Fig. 6.4a.

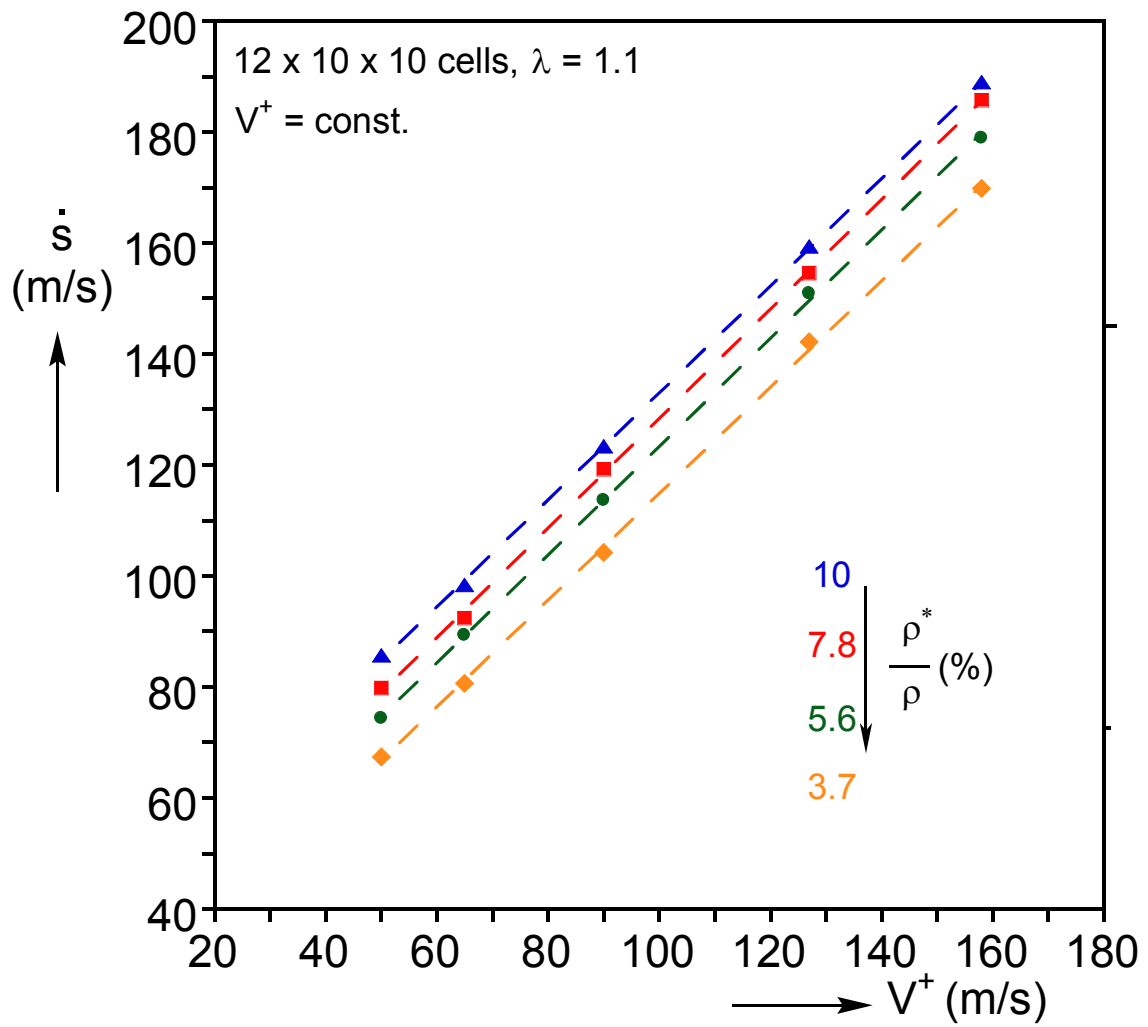


Fig. 6.6 Calculated shock speed-backing mass velocity Hugoniot for all densities considered.

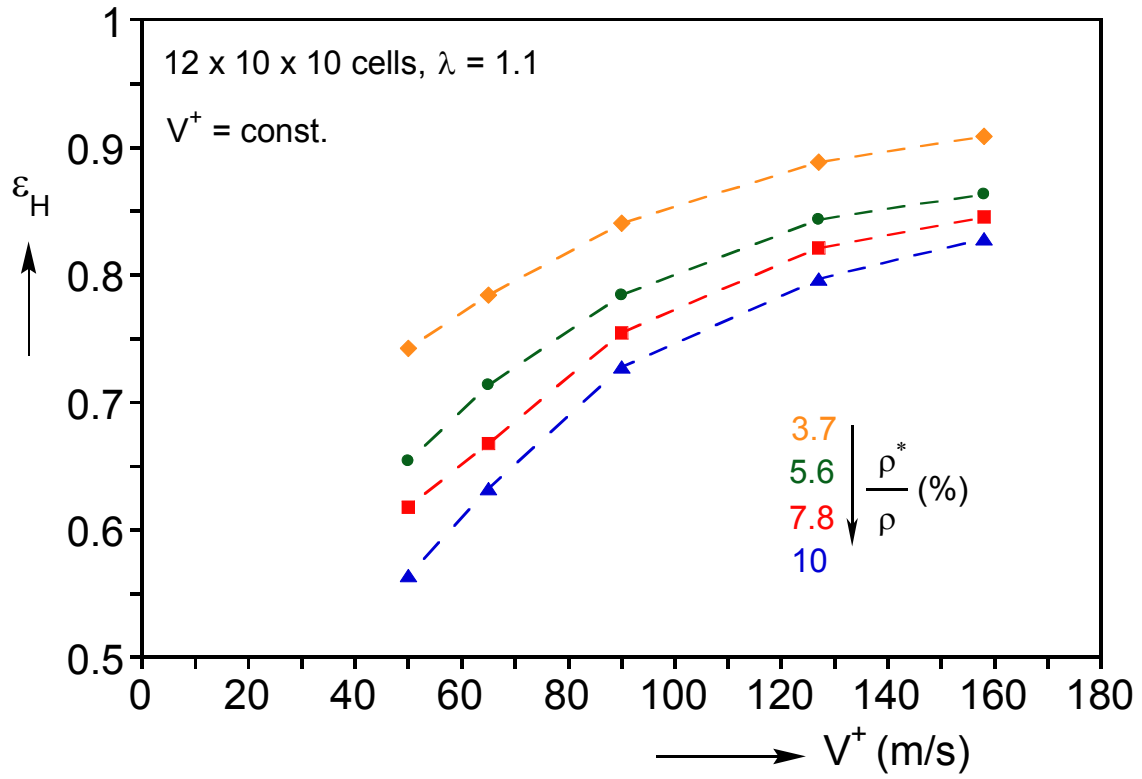


Fig. 6.7 Calculated Hugoniot strain-backing mass velocity for all densities considered.

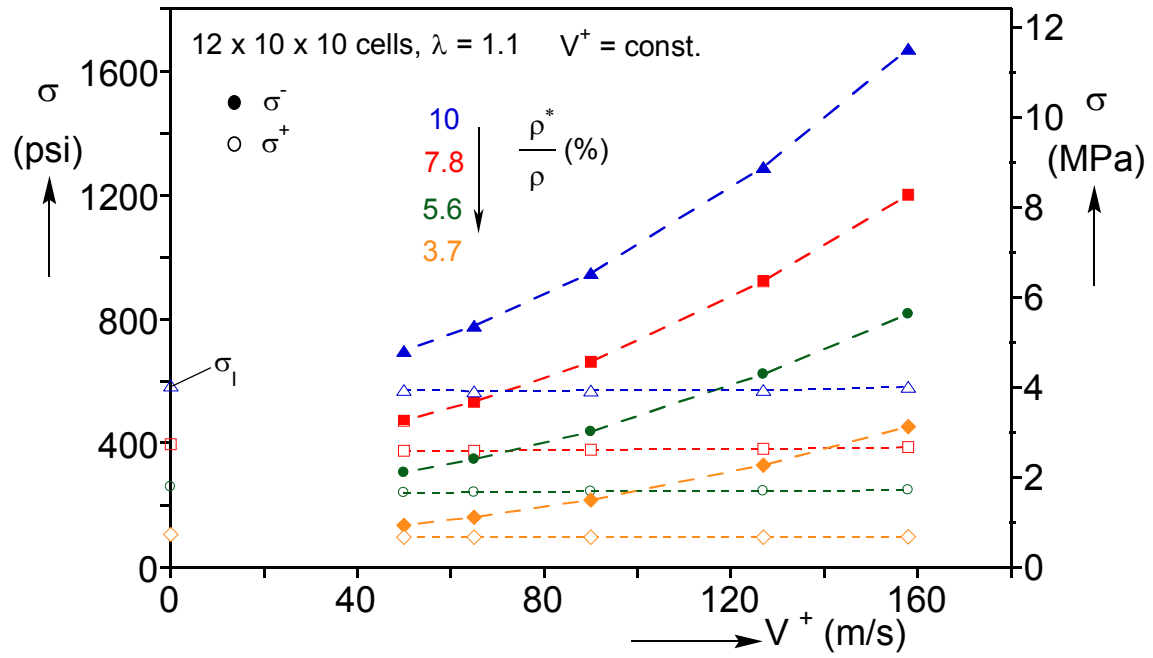
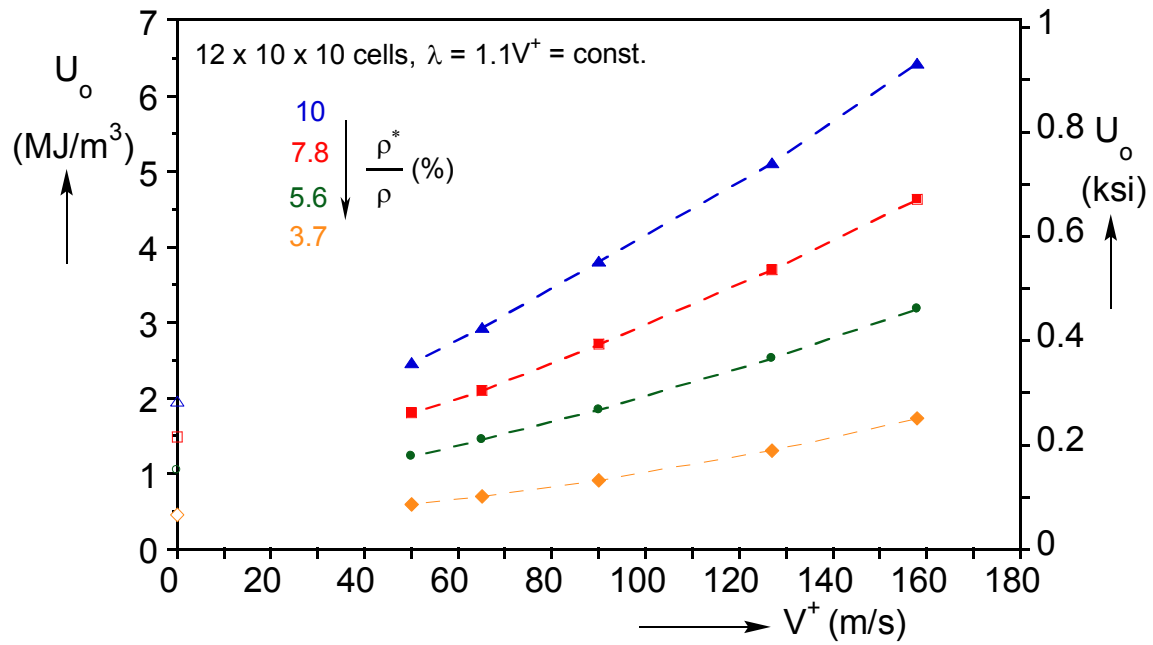
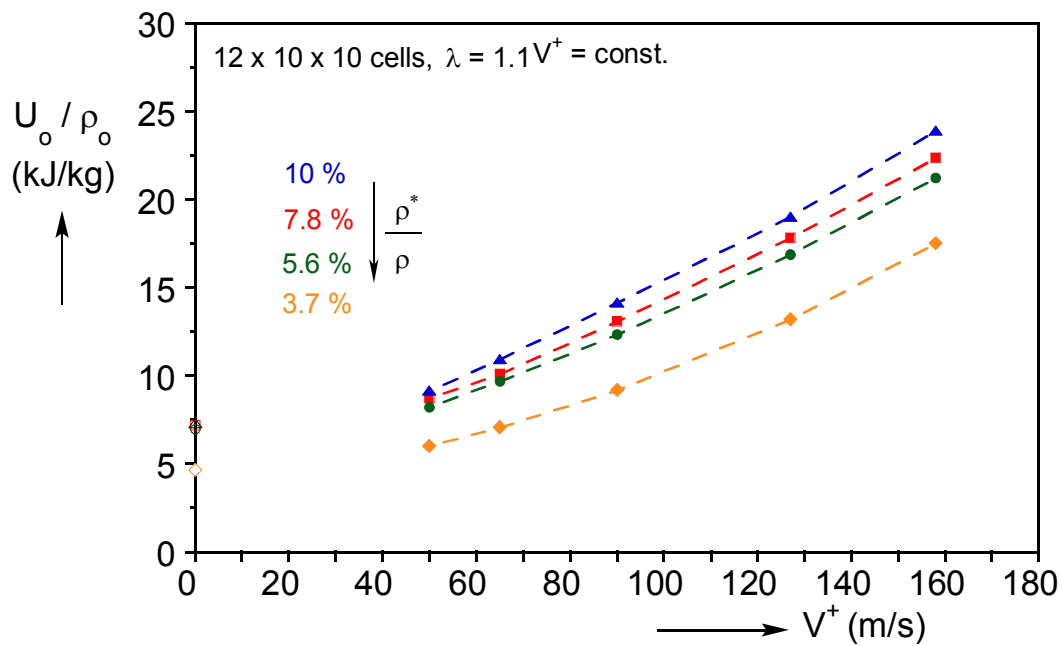


Fig. 6.8 Calculated Hugoniot of the stress ahead (σ^+) and behind (σ^-) the shock vs. backing mass velocity for all densities considered.

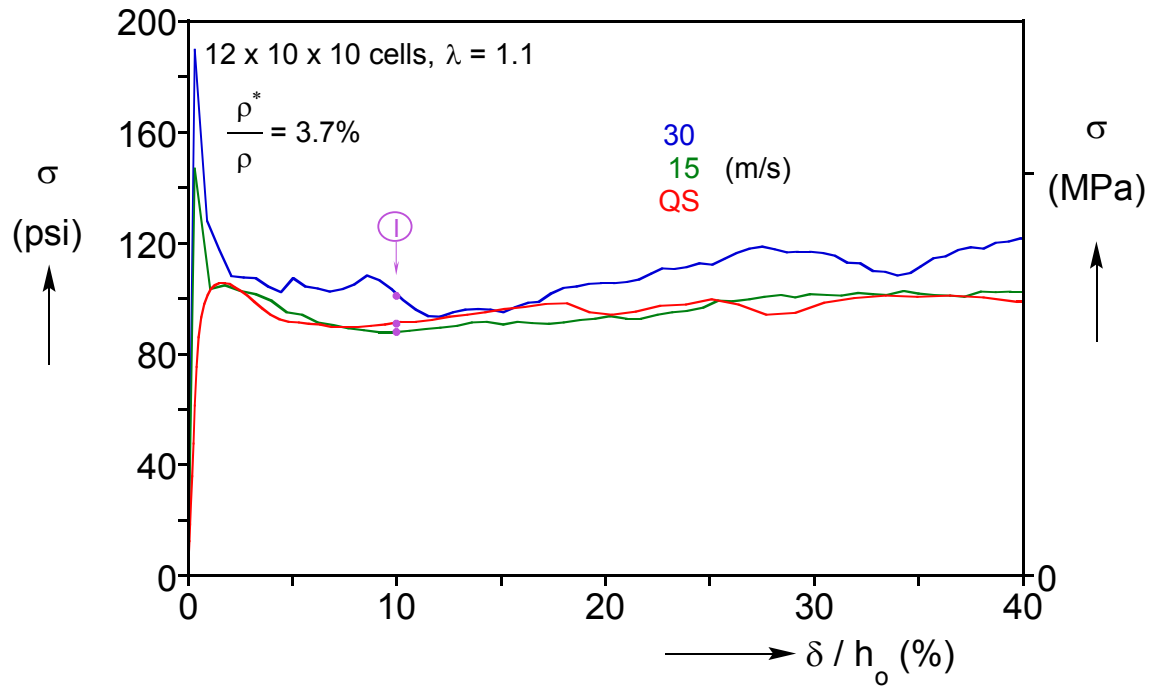


(a)

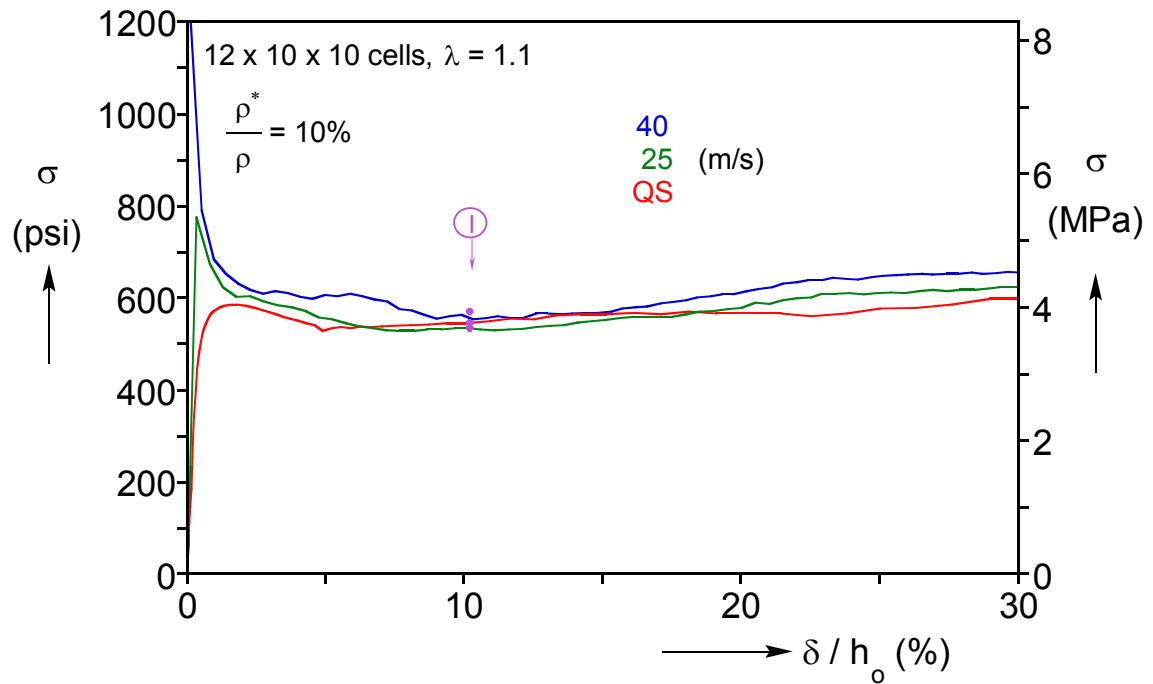


(b)

Fig. 6.9 (a) Strain energy density and (b) specific energy vs. backing mass velocity for all densities considered.



(a)



(b)

Fig. 6.10 Stress-displacement responses from several subcritical constant impact speed calculations for a foam with (a) 3.7% and (b) 10% relative density.

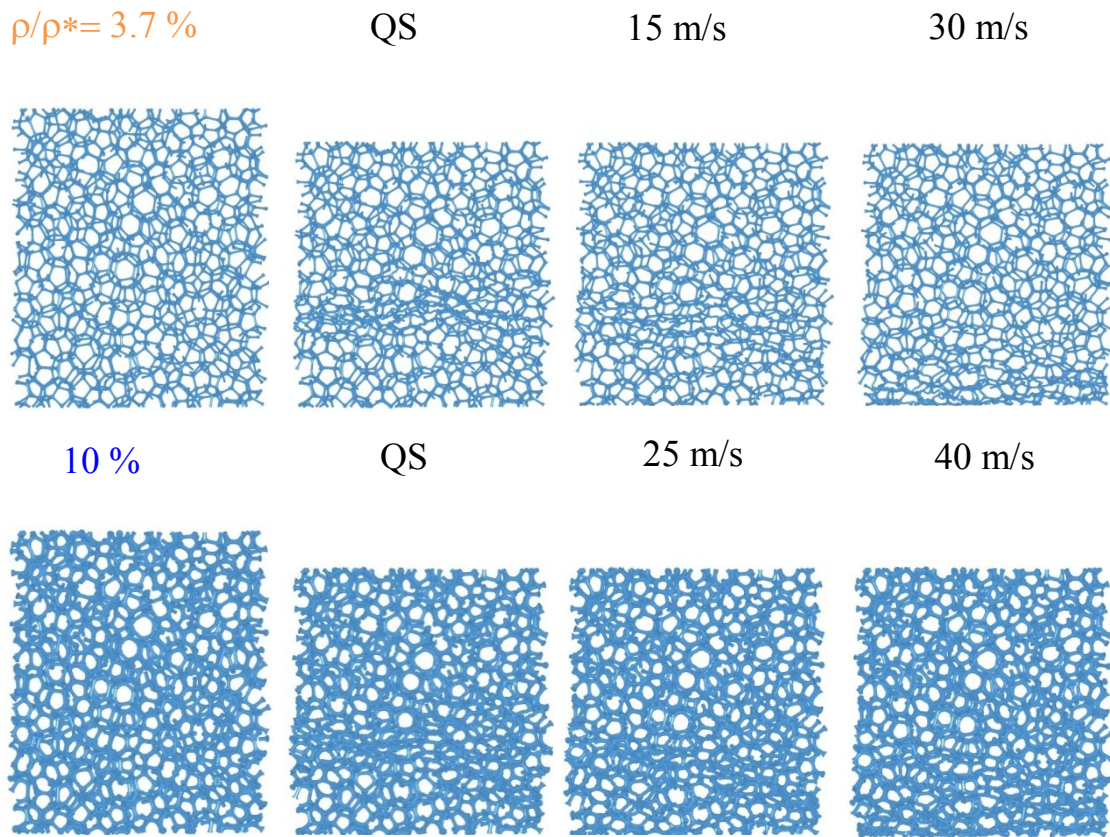


Fig. 6.11 Initiation of crushing ($\bar{\delta} = 10\%$) by sub-critical velocity impact on the foams with 3.7% and 10% relative density.

Chapter 7: Summary and Conclusions

This study focuses on a modeling framework for simulating the compressive response of open-cell metal foams under quasi-static and dynamic loadings. The approach involves the development of micromechanically accurate models with random microstructure. The models start as random soap froth generated through the Surface Evolver software. The skeletal microstructure is then dressed with beam elements with geometric characteristics that mimic measurements on ERG Duocel® aluminum foams. Such models are used to simulate the complete quasi-static crushing response of foams tested in Jang and Kyriakides (2009a) from the initial elastic regime to localization, collapse propagation and densification. The second part of the work involves the use of the same modeling framework to simulate the dynamic response and predict the energy absorption capacity of the same foams under impact at various velocities. Following are the major conclusions drawn from each part of the study along with recommendations for future work.

7.1 Quasi-static Crushing

Exploiting the nearly monodisperse nature of the class of foams analyzed, Jang and Kyriakides (2009b) showed that all mechanical properties starting from the elastic moduli, the strength, the level of the stress plateau and its extent could be reproduced with accuracy using a suitably modified Kelvin cell microstructure. A weakness of such models is that they cannot be applied to foams that exhibit polydispersity. Furthermore, the localized crushing patterns that develop in such regularized microstructures differ from those seen in actual foams.

The present work overcame the limitations of the Kelvin cell models by considering truly random foam microstructures generated using the Surface Evolver

software. Both the experiments and the modeling involved crushing of finite size rectangular blocks with free lateral sides. For the response of such blocks to be representative of bulk material they have to be large and consequently computationally intensive. This in turn dictates that the ligaments should be modeled as beams. Thus, the models started as random soap froth with N^3 cells. The ligaments were dressed with straight beams with non-uniform cross sections that follow measurements made on actual foam ligaments. The models were assigned the density and anisotropy of the actual foams and the elasto-plastic properties of the Al-alloy base material. The microstructure was discretized with finite elements using LS-DYNA, which allows for beam-to-beam contact on the outer surface of the ligaments. The latter element is an essential feature for locally limiting the extent to which collapsing cells can deform and thus enabling the spreading of crushing to neighboring cells.

Cubical models of several sizes were crushed between rigid surfaces. Because the lateral sides of the models were free, the solution could be influenced by the size of the domain. Parametric studies showed that the calculated response converged at a model size of 10^3 cells. The resultant rise direction stress-displacement response reproduced experimental ones in all respects. Following a load maximum, localized cell crushing nucleated at the weakest sites. The crushing developed into a band with a 3-D relief across the model that replicates experimental observations made using X-ray tomography. Contact between ligaments of crushed cells arrested local deformation causing crushing to spread to neighboring cells. In this way crushing progressively spread throughout the model while the stress remained relatively unchanged. As the crushing fronts approached the top and bottom planes, the stress gradually increased because of the stiffening effect provided by the rigid surfaces. Thus, the end cells crushed last. Continued loading beyond this point required an increase in stress that further compacted

the already significantly densified microstructure. These events and the associated crushing patterns reproduced with accuracy corresponding experimental ones. Coulomb friction between contacting ligaments was found to have a stabilizing effect on the numerical solution. Crushing the model in the transverse direction resulted in a similar behavior but at an overall lower stress level. The simulations were once again in good agreement with experimental results.

7.2 Dynamic Crushing

Barnes (2012) and Barnes *et al.* (2014) used a custom built gas-gun to perform dynamic crushing experiments with initial impact speeds in the range of 20-160 m/s. Similar to previous studies, the foam specimens were crushed by firing a projectile mass at a stationary foam specimen attached to a pressure bar (*stationary* impact) or by accelerating a backing mass-foam system and impacting the bar (*direct* impact). The stress at one end was determined from the pressure bar while the deformation of the entire foam specimen was monitored with high-speed photography. Specimens impacted at velocities of 60 m/s and above developed nearly planar shocks that propagated at well-defined speeds crushing the specimen. The highly densified material behind the shock was found to be under a higher stress than the quasi-static initiation stress and compacted to a higher (Hugoniot) strain than the quasi-static densification strain. Conservation of momentum was used along with the measured stress and velocities to evaluate the stress on the opposite side of the specimen. The stress behind the shocks was found to increase as V_b^2 . The material ahead of the shock was under a relatively low stress that left it essentially undeformed. This stress level was found to be bounded by the quasi-static initiation stress of the foam. Conservation of energy enabled the evaluation of the energy

consumed across the shock as a function of impact speed and was found to exhibit a significant increase with velocity.

Random foam models were used to simulate these experiments, reinforce their findings and further examine the dynamic behavior of foams. Most calculations were performed using a $12 \times 8 \times 8$ cell model which was scaled to have the 4 in (102 mm) length of the foam specimens used in the experiments. The models reproduced all aspect of shock formation and propagation. This includes the stresses recorded at the proximal and distal ends, the strain behind the shock and the velocities of the backing mass and shock. For direct impact tests the shock starts at the stationary target and propagates towards the moving mass. It is planar but with a somewhat ragged surface relief due to the discreteness and randomness of the cells. It has a width of about one-half of a cell. The proximal stress traced a stress plateau but discreteness of the microstructure introduced some stress undulations. The distal stress was confirmed to be bounded by the initiation stress of the quasi-static crushing response.

A series of constant impact speed numerical calculations were performed and used to develop the impact–shock velocity Hugoniot of the Al foam. This Hugoniot exhibits the linear trajectory of the one generated from the experiments. The trajectory is parallel to the experimental one but has a slightly lower intercept. In concert with the experimental results, the Hugoniot strain increased with impact speed asymptotically approaching 0.87 at $V^+ = 200$ m/s; in other words, the shocks compact the material significantly more than the 0.55 value induced when crushed quasi-statically. The stress behind the shock increased quadratically with impact speed again in concert with the corresponding measured Hugoniot. The stress in the undeformed material ahead of the shock remains essentially at the level of the initiation stress of the quasi-static case.

At relatively low impact speeds, in this case 20 m/s and lower, crushing initiated at the weakest site in the model, propagated until it encountered an obstacle when localization nucleates at another site, and so on. In other words, the crushing developed as in quasi-static loading. The proximal and distal end stresses follow essentially the quasi-static response including the onset of densification. That is to say, minimal inertial effects were observed. At impact speeds in the range of 20–40 m/s, a mixed shock/non-shock behavior was observed. A weak shock initiated at the proximal end but subsequently localization developed at other sites too. The corresponding stress started to increase and separate from that recorded at the distal end, and the induced strain gradually started to increase beyond the QS level. At impact of 50 m/s and higher clear shock behavior was observed. The transition to shock behavior is rather gradual and our best estimate of when shocks occur is between 40 and 50 m/s.

The experimental and numerical results demonstrated that a shock will develop when the impact induces a stress that is higher than the initiation stress of the QS case. The shock then follows the Rayleigh line to a higher stress, strain, and energy level. The numerical results confirm that the variables behind the shock are not related to the quasi-static response in any way. Consequently, predictions must be based on the Hugoniot as indeed is the tradition in shock physics. This conclusion is one of the major contributions of this study, since a significant body of work can be found in the literature where predictions of the dynamic behavior of foams use the quasi-static response, or an approximation of it (e.g., r-p-p-l) as a constitutive model.

7.3 Effect of Relative Density on Crushing and Energy Absorption

In view of the success of the numerical models in reproducing the quasi-static and dynamic behavior of the foams analyzed, similar models were generated and used in

Chapter 6 to examine how relative density affects the stresses, energy absorption, and other parameters of interest. Simulations were performed for loading rates ranging from quasi-static to shock type impact crushing. The same random microstructure was used to produce four foams with relative densities in the range 3.7-10%. These four models were subsequently crushed quasi-statically. It was found that the initiation stress increases nearly linearly with density while the densification strain decreases linearly. The energy density increases significantly while the specific energy has a more modest variation with density.

The same set of foam models was also used to examine how density affects all representations of the Hugoniot curve. It was found that similar to the densification strain, the Hugoniot strain is larger in less dense foams because of the increased local compaction of the cells. The shock front velocity was higher and the shock speed-impact velocity Hugoniot lines translated upwards (higher shock speed) while keeping the same slope. The stresses ahead of the shock followed the nearly linear increase of the quasi-static initiation stresses and induced the same increase to the stresses behind the shock. These stresses increased further because of the corresponding acceleration of the shock front in higher densities. The energy densities and specific energies expended across the shock also increased with relative density; the former much more than the latter. An increase of the critical velocity to shock formation of about 10 m/s between the relative densities of 3.7% and 10% was also found.

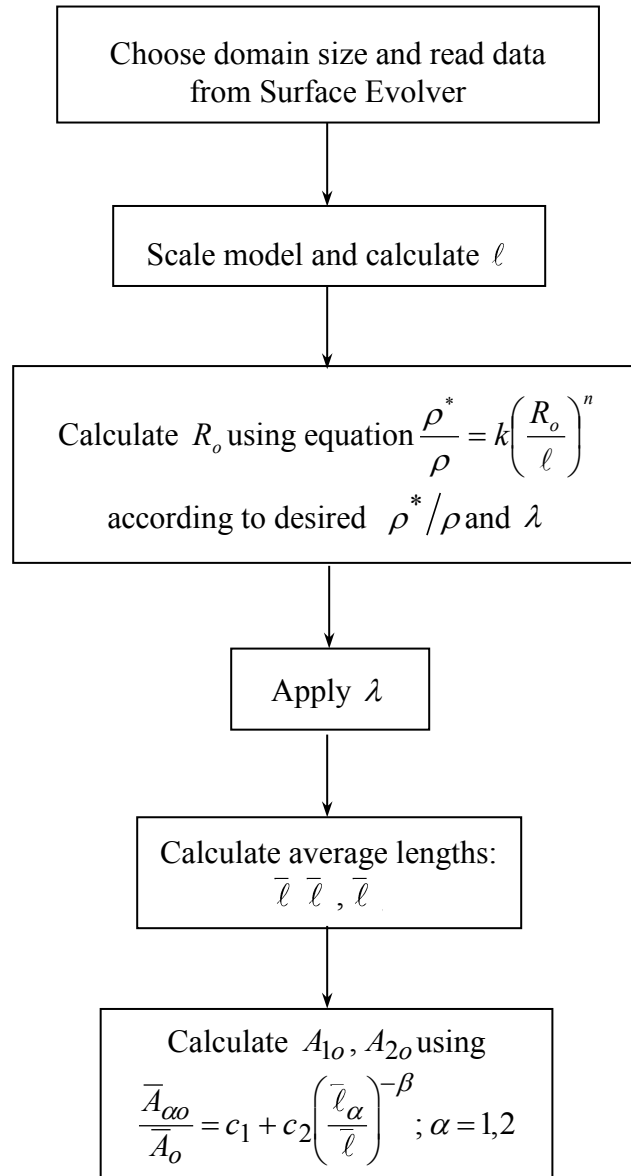
7.4 Future Work

The success in all aspects of the modeling framework developed bodes well for its future use in *polydisperse* foams. These are foams with significant variations in their cell sizes. A study on the effect of polydispersity on the mechanical properties, from the

elastic to the complete crushing response and the Hugoniot would complete the study of open-cell metal foams. The end goal is the ability to select the most appropriate foam microstructure (density, anisotropy, polydispersity) and base material behavior (elastic, plastic, etc.) for a given application.

Appendix A

Flowchart for Generating Random Foam Models



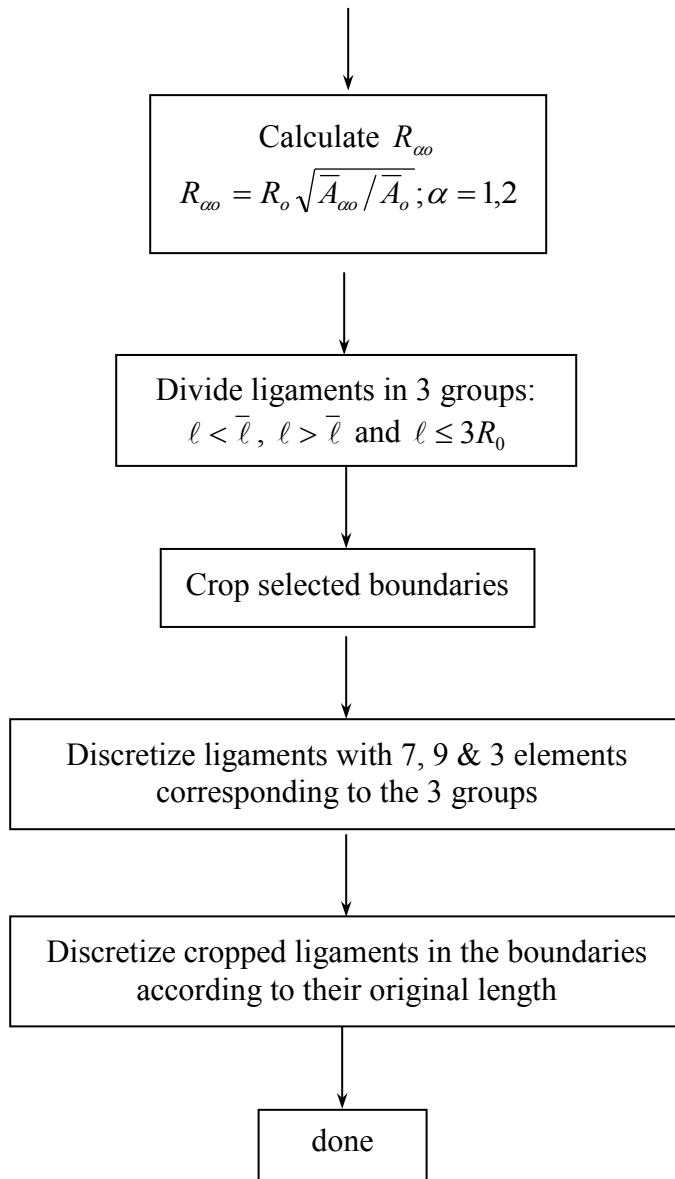


Fig. A.1 Flowchart for generating random foam models.

References

Ashby, M.F., Evans, A., Fleck, N.A., Gibson, L.J., Hutchinson, J.W., Wadley, H.N.G., 2000. *Metal Foams: A Design Guide*. Butterworth-Heinemann.

Barnes, A.T., 2012. *On the Dynamic Crushing of Open-Cell Aluminum Foams*. MS, Thesis, Engineering Mechanics, University of Texas at Austin, Dec. 2012.

Barnes, A.T., Ravi-Chandar, K., Kyriakides, S., Gaitanaros, S., 2014. Dynamic crushing of aluminum foams: Part I – Experiments. *Int'l J. Solids & Structures*, **51**:1631-1645.

Bart-Smith, H., Bastawros, A.-F., Mumm, D.R., Evans, A.G., Sypeck, D.J. and Wadley, H.N.G., 1998. Compressive deformation and yielding mechanisms in cellular Al alloys determined using X-ray tomography and surface strain mapping *Acta Materialia* **46**, 3583-3592.

Bethe, H., 1942. On the theory of shock waves for an arbitrary equation of state. Report No. 545 for the Office of Scientific Research and Development, Serial No. NDRC-B-237; reproduced in *Classic Papers in Shock Compression Science*, J.N. Johnson and R. Cheret (Eds), Springer, 1998, 421-492).

Brakke, K.A., 1992. The Surface Evolver. *Experimental Mathematics* **1**, 141-165. Available at <http://www.susqu.edu/facstaff/b/brakke/evolver/>

Davison, L. 2008. *Fundamentals of Shock Wave Propagation in Solids*. Springer.

Duchamp, M., Bartout, J. D., Forest, S., Bienvenu, Y., Walther, G., Saberi, S., Boehm, A., 2009. Mechanical Behavior of Nickel Base Foams for Diesel Particle Filter Applications. In: (Ed.) Han Zhao and N.A. Fleck, *Proc. IUTAM Symposium on Mechanical Properties of Cellular Materials*, September 2007, LMT-Cachan, Springer, Netherlands, pp. 51-67.

Elnasri, I., Pattofatto, S., Zhao, H., Tsitsiris, H., Hild, F. and Girard, Y., 2007. Shock enhancement of cellular structures under impact loading: Part I experiments. *J. Mechanics Phys. Solids* **55**, 2652-2671.

ERG Corp. website, available at <http://www.ergaerospace.com/Aluminum-properties.htm>

Gaitanaros, S., Kyriakides, S. and Kraynik, A.M. 2012. On the crushing response of random open-cell foams. *Int'l J. Solids Struct.* **49**, 2733-2743.

Gaitanaros, S., Kyriakides, S., 2014. Dynamic crushing of aluminum foams: Part II – Analysis. *Int'l J. Solids & Structures*, **51**: 1646-1661.

Gibson, L.J., Ashby, M.F., Zhang, J. and Triantafillou, T.C., 1989. Failure surfaces for cellular materials under multiaxial loads - I Modeling *Int'l J. Mechanical Sciences* **31**, 665-678.

Gibson, L.J., Ashby, M.F., 1997. *Cellular Solids: Structure and Properties, 2nd Ed.* Cambridge University Press.

Gibson, Lorna J., Michael F. Ashby, and Brendan A. Harley. *Cellular materials in nature and medicine.* Cambridge University Press, 2010.

Gioux, G., McCormack, T.M. and Gibson, L.J., 2000. Failure of aluminum foams under multiaxial loads. *Int'l J. Mechanical Sciences* **42**, 1097-1117.

Gong, L., Jang, W.-Y and Kyriakides S. 2005. Compressive response of open-cell foams. Part I: Morphology and elastic properties. *Int'l J. Solids Struct.* **42**, 1355-1379.

Gong, L., Kyriakides S., 2005. Compressive response of open-cell foams. Part II: Initiation and evolution of crushing. *Int'l J. Solids & Structures* **42**, 1381-1399.

Gong, L., Kyriakides, S., Triantafyllidis, N., 2005. On the stability of Kelvin cell foams under compressive Loads. *J. Mechanics and Physics of Solids* **53**:4, 771-794

Graff, K. 1975. *Wave Motion in Elastic Solids.* Ohio State University Press.

Herrmann, W., 1969. Constitutive equations for the dynamic compaction of ductile porous materials. *J. Appl. Physics* **40**, 2490-2499.

Hilyard, N.C., Cunningham, A. eds., 1994. *Low Density Cellular Plastics: Physical Basis of Behavior.* Chapman & Hall, London.

Hönig, A., Stronge, W.J. 2002a. In-plane dynamic crushing of honeycomb Part I: crush band initiation and wave trapping. *Int'l J. Mech. Sciences* **44**, 1665-1696.

Hönig, A., Stronge, W.J. 2002b. In-plane dynamic crushing of honeycomb Part II: application to impact. *Int'l J. Mech. Sciences* **44**, 1697-1714.

Hughes, T.J.R. and Liu, W.K., 1981. Nonlinear finite element analysis of shells-Part II. Two-dimensional shells. *Computer Meth. Applied Mech. Eng.* **27**, 167-181.

Jang, W.-Y., Kraynik, A.M., Kyriakides, S., 2008. On the microstructure of open-cell foams and its effect on elastic properties. *Int'l J. Solids & Structures* **45**, 1845-1875.

Jang, W.-Y., Kyriakides, S., 2009a. On the crushing of aluminum open-cell foams: Part I experiments. *Int'l J. Solids & Structures* **46**, 617-634.

Jang, W.-Y., Kyriakides, S., 2009b. On the crushing of aluminum open-cell foams: Part II analysis. *Int'l J. Solids & Structures* **46**, 635-650.

Jang, W.-Y., Kyriakides, S. and Kraynik, A.M. 2010. On the compressive strength of open-cell foams with Kelvin and random cell structures. *Int'l J. Solids & Structures* **47**, 2872-2883.

Klintworth, J.W. and Stronge, W.J., 1998. Elasto-plastic yield limits and deformation laws for transversely crushed honeycombs. *Int'l J. Mech. Sciences* **30**, 273-292.

Kraynik, A.M., 2003. Foam structure: From soap froth to solid foams. *MRS Bulletin* **28/4**, 275-278.

Kraynik, A.M., Reinelt, D.A., van Swol, F., 2003. Structure of random monodisperse foam. *Physical Review E* **67**, 031403/1-11.

Kraynik, A.M., Reinelt, D.A., van Swol, F., 2004. Structure of random foam. *Phys. Rev. Lett.* **93/20**, 208301/1-4.

Kraynik, A.M., Reinelt, D.A., van Swol, F., 2005. Structure of random bidisperse foam. *Colloids and Surfaces A* **263**, 11-17.

Kraynik, A.M., 2006. The structure of random foam. *Advanced Engineering Materials* **8/9**, 900-906.

Laroussi, M., Sab, K., Alaoui, A., 2002. Foam mechanics: Nonlinear response of an elastic 3D-periodic microstructure. *Int'l J. Solids & Structures* **39**, 3599-3623.

Lee, S., Barthelat, F., Moldovan, N., Espinosa, H.D. and Wadley, H.N.G., 2006. Deformation rate effects on failure modes of open-cell Al foams and textile cellular materials. *Int'l J. Solids & Structures* **43**, 53-73.

LS-DYNA Theory Manual, Livermore Software Technology Corporation, 2006.

Luxner, M.H., Stampfl, J., Pettermann, H.E., 2007. Numerical simulations of 3D open cell structures-influence of structural irregularities on elasto-plasticity and deformation localization. *Int'l J. Solids & Structures* **44**, 2990-3003.

Maines, W.R., Chhabildas, L.C., Reinhart, W.D., Thornhill III, T.F., 2010. High velocity uniaxial strain response of ERG aerospace aluminum foam. Proc. ASME 2010 Pressure Vessels & Piping Div/K-PVP Conf., July 18-22, 2010, Bellevue, Washington.

March, S.P., Ed. *LASL Shock Hugoniot data*, 1980. University of California Press, Berkeley-Los Angeles-London. ISBN 0-520-04007-4.
www.fas.org/sgp/othergov/doe/lanl/docs1/shd.pdf

Matzke, E.B., 1946. The three-dimensional shape of bubbles in foam-An analysis of the role of surface forces in three-dimensional shape determination. *American Journal of Botany* **33**, 58-80.

Mills, N.J., 2007. The high strain mechanical response of the wet Kelvin model for open-cell foams. *Int'l J. Solids & Structures* **44**, 51-65.

Montanini, R., 2005. Measurement of strain sensitivity of aluminum foams of energy dissipation. *Int'l J. Mechanical Science* **47**, 26-42.

Morris, C.E., 1991. Shock-wave equation-of-state studies at Los Alamos. *Shock Waves* **1**, 213-222.

Nemat-Nasser, S., Kang, W.J., McGee, J.D., Guo, W.-G., Isaacs, J.B., 2007. Experimental investigation of energy-absorption characteristics of components of sandwich structures. *Int'l J. Imp. Engin.* **34**, 1119-1146.

Nieh, T.G., Higashi, K. and Wadsworth, J., 2000. Effect of cell morphology on the compressive properties of open-cell aluminum foams. *Material Science and Engineering A*, **283**, 105-110.

Papka, S.D. and Kyriakides, S., 1994. In-plane compressive response and crushing of honeycomb. *J. Mechanics & Physics Solids*, **42**, 1499-1532.

Papka, S.D., Kyriakides, S., 1998a. In-plane crushing of a polycarbonate honeycomb. *Int'l J. Solids & Structures* **35**, 239-267.

Papka, S.D. and Kyriakides, S., 1998b. Experiments and full-scale numerical simulations of in-plane crushing of a honeycomb. *Acta Materialia* **46**, 2765-2776.

Pattofatto, Elnasri, I., S., Zhao, H., Tsitsiris, H., Hild, F. and Girard, Y., 2007. Shock enhancement of cellular structures under impact loading: Part II analysis. *J. Mech. Physics Solids* **55**, 2672-2686.

Priester, R.D. and Turner, R.B. 1994. The morphology of flexible polyurethane matrix polymers. In, *Low Density Cellular Plastics: Physical Basis of Behavior*. Ed. Hilyard, N.C. and Cunningham, A. pp. 78-103. Chapman & Hall, London.

Radford, D.D., Deshpande, V.S., Fleck, N.A., 2005. The use of metal foam projectiles to simulate shock loading on a structure. *Int'l J. Imp. Eng.* **31**, 1152-1171.

Reid, S.R. and Peng, C., 1997. Dynamic uniaxial crushing of wood. *Int'l J. Imp. Eng.* **19**, 531-570.

Ruan, D., Lu, G., Wang, B. and Yu, T.X. 2003. In-plane dynamic crushing of honeycombs – a finite element study. *Int'l J. Impact Engin.* **28**, 161-182.

Simone, A.E. and Gibson, L.J., 1998. Aluminum foams produced by liquid-state processes. *Acta Materialia* **46/9**, 3109-3123.

Skews, B.W., Atkinks, M.D., and Seitz, M.W., 1991. Gas dynamic and physical behaviour of compressible porous foams struck by a weak shock. Shock Waves, Proc. 18th *Int'l Symp. on Shock Waves*, Sendai, Japan, Ed. K. Takayama, Vol. 1, pp. 511-516.

Tan, P.J., Reid, S.R., Harrigan, J.J., Zou, Z. and Li, S., 2005a. Dynamic compressive strength properties of aluminium foams. Part I - experimental data and observations. *J. Mech. Phys. Solids* **53**, 2174-2205.

Tan, P.J., Reid, S.R., Harrigan, J.J., Zou, Z. and Li, S., 2005b. Dynamic compressive strength properties of aluminium foams. Part II - 'shock' theory and comparison with experimental data and numerical observations. *J. Mech. Phys. Solids* **53**, 2206-2230.

Tan, P.J., Reid, S.R., and Harrigan, J.J., 2012. On the dynamic mechanical properties of open-cell metal foams – a reassessment of the 'simple-shock theory'. *Int'l J. Solids & Struct.* **49**, 2744-2753.

Thompson, W. (Lord Kelvin), 1887. On the division of space with minimal partitional area. *Philos. Magazine* **24**, 5th Series 503-514.

Thornton, P.H. and Magee, C.L., 1975. The deformation of aluminum foams. *Metallurgical Transaction A* **6A**, 1253-1263.

Triantafillou, T.C. Zhang, J., Shercliff, T.L., Gibson, L.J. and Ashby, M.F., 1989. Failure surfaces for cellular materials under multiaxial loads: I Modeling. *Int'l J. Mechanical Science* **31**, 635-663.

Warren, W.E., Kraynik, A.M., 1997. Linear elastic behavior of a low-density Kelvin foam with open cells. *ASME J. Applied Mechanics* **64**, 787-793.

Weaire, D., Hutzler, S., 1999. *The Physics of Foams*. Oxford University Press, Oxford.

Zaretsky, E., Ben-Dor, G., 1995. Compressive stress-strain relations and shock Hugoniot curves for flexible foams. *AMSE J. Eng. Mater. Technol.* **117**, 278-284.

Zaretsky, E., Asaf, Z., Ran, E., Aizik, F. 2012. Impact response of high density flexible polyurethane foam. *Int'l J. Impact Eng.* **39**, 1-7.

Zhang, J., Ashby, M.F., 1992. The out-of-plane properties of honeycombs. *International Journal of Mechanical Sciences*, **34**(6), 475-489.

Zhou, J., Mercer, C. and Soboyejo, W.O., 2002. An investigation of the microstructure and strength of open-cell 6101 aluminum foams. *Metallurgical and Materials Transactions* **33A**, 1413-1427.

Zhou, J., Shrotriya, P. and Soboyejo, W.O., 2004. Mechanisms and mechanics of compressive deformation in open-cell Al foams. *Mechanics of Materials* **36**, 781-797.

Zhou, J. and Soboyejo, W.O., 2004. Compression-compression fatigue of open cell aluminum foams: macro-/micro- mechanisms and the effect of heat treatment. *Materials Science and Engineering* **A369**, 23-35.

Zhu, H.X., Knott, J.F., Mills, N.J., 1997. Analysis of the elastic properties of open-cell foams with tetrakaidecahedral cells. *J. Mechanics & Physics of Solids* **45**, 319-343.

Zou, Z., Reid, S.R., Tan, P.J., Li, S. and Harrigan, J.J. 2009. Dynamic crushing of honeycombs and features of shock fronts. *Int'l J. Impact Engin.* **36**, 165-176.

Vita

Stavros Gaitanaros entered the University of Thessaly in 2000 and graduate with a Diploma (2005) and M.Sc. (2007) in Mechanical & Industrial Engineering. He then entered the Graduate School of The University of Texas at Austin to pursue a Ph. D. in Engineering Mechanics. During his final year he taught the EM 319 Mechanics of Solids class, serving as an Assistant Instructor in the Department of Aerospace Engineering and Engineering Mechanics. He made several presentations at national and international conferences and co-authored the following journal publications:

- [1] Gaitanaros, S., Kyriakides, S., Kraynik, A.M., 2012. On the crushing response of random open-cell foams. *Int'l J. Solids & Structures*, **49**:2733-2743.
- [2] Barnes, A.T., Ravi-Chandar, K., Kyriakides, S., Gaitanaros, S., 2014. Dynamic crushing of aluminum foams: Part I – Experiments. *Int'l J. Solids & Structures*, **51**:1631-1645.
- [3] Gaitanaros, S., Kyriakides, S., 2014. Dynamic crushing of aluminum foams: Part II – Analysis. *Int'l J. Solids & Structures*, **51**: 1646-1661.
- [4] Gaitanaros, S., Kyriakides, S., 2014 Energy absorption in open-cell foams under impact (*in preparation*).

Permanent email: stgaitan@utexas.edu

This dissertation was typed by the author.